UNIVERSIDADE
BEIRA INTERIOR

Design of a Flying Wing to Convert an Existing Multirotor UAV into a VTOL Aircraft
(Versão final após defesa)

Ricardo Jorge Rodrigues Marques

Dissertação para obtenção do Grau de Mestre em
Engenharia Aeronáutica
(Ciclo de estudos integrado)

Orientador: Prof. Doutor Pedro Vieira Gamboa
Co-orientador: Mestre Filipe Miguel Jesus Silva

Covilhã, dezembro de 2023

Declaração de Integridade

Eu, Ricardo Jorge Rodrigues Marques, que abaixo assino, estudante com número de inscrição 41123 de/o Mestrado Integrado em Engenharia Aeronáutica da Faculdade de Engenharia, declaro ter desenvolvido o presente trabalho e elaborado o presente texto em total consonância com o **Código de Integridade da Universidade da Beira Interior**.

Mais concretamente afirmo não ter incorrido em qualquer das variedades de Fraude Académica, e que aqui declaro conhecer, que em particular atendi à exigida referenciação de frases, extratos, imagens e outras formas de trabalho intelectual, e assumindo assim na íntegra as responsabilidades da autoria.

Universidade da Beira Interior, Covilhã 29/11/2023

Assinado por: **Ricardo Jorge Rodrigues Marques**
Num. de Identificação: 14752619
Data: 2023.11.30 20:58:19+00'00'

CHAVE MÓVEL

Acknowledgements

First of all, I would like to thank my thesis supervisor, Professor Pedro Gamboa, and my co-supervisor, Filipe Silva, for their patience, assistance and guidance throughout all phases of this dissertation.

I would also like to thank CEiiA for the opportunity to work on this project and complete this academic journey. To the AAM team, thank for being so supportive and outgoing.

A especial thanks to my friends that managed to put up with me all these years, I know it wasn't easy. Thank you for the late night "study" sessions, for the summer vacations, for travelling the world with me, for the walks and conversations every week at the same place. Thank you for all those memories.

To my family, especially to my parents, thank you for ensuring that I had everything I needed, for providing me with unwavering support, and most importantly, for believing in me all these years. I literally could not have done it without you.

Resumo

Esta dissertação contribui para um dos projetos que se encontra em desenvolvimento pelo departamento de Mobilidade Aérea Avançada (AAM) do Centro Português de Engenharia e Desenvolvimento de Produtos (CEiiA). O objetivo do projeto é desenvolver um veículo aéreo não tripulado (UAV) de descolagem e aterragem vertical (VTOL) capaz de realizar missões de longo alcance e operar em ambientes urbanos através de um sistema de asas removíveis.

No presente trabalho são detalhados o desenvolvimento preliminar aerodinâmico e estrutural de uma asa que tem como propósito ser integrada com o multirotor desenvolvido pela AAM.

Foi realizada uma revisão bibliográfica sobre temas como design de aeronaves, estruturas de aeronaves, estruturas em compósitos e tecnologias UAV VTOL. Isto foi seguido pelo design conceptual de uma asa, onde são considerados os requisitos do departamento e as restrições impostas pela geometria do multirotor para determinar possíveis configurações. As configurações mais viáveis foram avaliadas e, através de um processo de seleção, um design base foi estabelecido.

Utilizando o software Flow5, foi realizada uma seleção de perfis, uma determinação da disposição dos componentes, o design de um modelo aerodinâmico da asa e uma análise de estabilidade da mesma. Todos estes parâmetros foram determinados e avaliados com base em exemplos ou restrições típicas encontradas na literatura, com a exceção do design da asa, que exigiu um método iterativo que foi definido especificamente para este caso.

Foi realizada uma análise da relação entre a tração e peso para selecionar o motor e a hélice mais adequados para o sistema propulsivo responsável pelo voo horizontal (FFPS). Além disso, foi também realizada uma análise de desempenho considerando as características aerodinâmicas da asa, o perfil da missão, a bateria selecionada e as características do FFPS para determinar o alcance e o tempo de voo do UAV.

Modelos CAD da asa e da estrutura interna foram desenvolvidos através do software SolidWorks, com base nas dimensões do modelo aerodinâmico da asa e nos requisitos estruturais.

Seleção de materiais, avaliações do empilhamento aplicado aos componentes e análises estruturais à estrutura da asa foram realizadas usando o software Ansys. As análises estruturais foram realizadas por análise de elementos finitos e usando a ferramenta *Composite Failure* para obter resultados.

O trabalho realizado nesta dissertação levou ao desenvolvimento de uma asa voadora com uma envergadura de seis metros, feita principalmente de fibra de carbono e sanduíches de espuma revestidos com fibra de carbono, projetada para ser integrada com um multirotor específico. A estrutura da asa tem uma massa total de aproximadamente 8.5 kg e é capaz de suportar um fator de carga máximo 6.75 vezes superior à força vertical aerodinâmica exercida na asa durante condições normais de voo cruzeiro. Com a asa montada e desprezando o

arrasto da estrutura do multirotor que se encontra exposta, o UAV é teoricamente capaz de realizar missões de 82.97 km num período de tempo de 0.92 h quando totalmente carregado, e missões de 105.13 km num período de tempo de 1.32 h quando vazio.

Palavras-chave

Seleção de Perfís Alares, Design Aerodinâmico de Asas, Análise de Estabilidade, CAD design, Estruturas em Compósito, Sequência de Empilhamento, Análise por Elementos Finitos, Falha em Compósitos.

Abstract

This dissertation contributes to one of the projects being developed by the Advanced Air Mobility (AAM) business unit of the Portuguese Centre of Engineering and Product Development (CEiiA). The project's objective is to develop a modular vertical takeoff and landing (VTOL) unmanned aerial vehicle (UAV) capable of performing long-range missions and operating in urban environments through a removable wing system.

The present work details the preliminary aerodynamic and structural development of a wing that can be integrated with the multirotor developed by the AAM business unit.

A literature review was conducted on topics such as aircraft design, aircraft structures, composite structures, and VTOL UAV technologies. This was followed by the conceptual design of the wing, which takes into account the requirements of the business unit and the constraints imposed by the multirotor's geometry to create several different configurations. The feasible configurations were evaluated and subsequently narrowed down until a baseline design was established.

An airfoil selection, an assessment of the component's arrangement, the design of an aerodynamic wing model, and a stability analysis were performed using the Flow5 software. All of these parameters were determined and evaluated based on examples or typical restrictions found in the literature, with the exception of the wing design, which required an iterative method that was defined specifically for this case.

A thrust-to-weight ratio constraint analysis was employed to select an appropriate motor and propeller for the forward flight propulsive system (FFPS). Additionally, a performance analysis was conducted considering the aerodynamic characteristics of the wing, the mission profile, the selected battery, and the characteristics of the FFPS to determine the range and endurance of the UAV.

A computer-aided design model of the wing and its internal structure was developed using SolidWorks, based on the dimensions of the aerodynamic wing model and the structural requirements of the wing.

A material selection, an assessment of the stacking sequence of the component's laminates, and a structural analysis of the wing's structure were performed using Ansys. The structural analyses were conducted using Finite Element Analysis and using the *Composite Failure* tool to obtain solutions.

The research conducted in this dissertation led to the development of a six-meter wingspan flying wing, primarily made of carbon fiber and foam-cored carbon fiber sandwiches, specifically designed to be integrated with a multirotor. The structure of the wing has a total mass of approximately 8.5 kg and is capable of withstanding an ultimate load factor 6.75 times greater than the vertical aerodynamic force exerted on the wing during normal cruise conditions. With the wing attached and disregarding the drag of the exposed frame, the UAV is

theoretically capable of performing 82.97 km missions over a duration of 0.92 h when fully loaded, and 105.13 km missions over a duration of 1.32 h when empty.

Keywords

Airfoil Selection, Wing Design, Stability Analysis, CAD Design, Composite Structures, Stacking Sequence, Finite Element Analysis, Composite Failure

Contents

Acknowledgements v

Resumo vii

Abstract ix

Contents xiii

List of Figures xviii

List of Tables xx

Nomenclature xxi

Symbols xxiii

Acronyms xxv

1 Introduction 1

1.1 Motivation . . . 1
1.2 CEiiA and AAM business unit . . . 2
1.3 Objectives . . . 2
1.4 Dissertation Outline . . . 3

2 Background and Tools 5

2.1 Theoretical Foundations . . . 5
2.1.1 Airfoils and Aerodynamics . . . 5
2.1.2 Wing Configuration . . . 12
2.1.3 Performance . . . 17
2.1.4 Stability . . . 20
2.1.5 Control Surfaces . . . 25
2.1.6 Wing Structure and Loads . . . 26
2.1.7 Composite Materials . . . 30
2.2 State of the art / VTOL UAVs . . . 33
2.2.1 VTOL History . . . 34
2.2.2 VTOL UAV Technologies . . . 35
2.2.3 VTOL UAV's Market and Applications . . . 36
2.3 Tools . . . 37
2.3.1 Flow5 . . . 37
2.3.2 Prop Selector . . . 38
2.3.3 SolidWorks . . . 38
2.3.4 Ansys . . . 38

3 Conceptual Design **39**
3.1 Design Process . . . 39
3.2 Requirements and Constraints . . . 39
3.3 Configuration Alternatives . . . 40
3.4 Wing Vertical Location . . . 43
3.5 Initial Concept . . . 43

4 Design Methodology **45**
4.1 Weight Build-up . . . 46
4.2 Center of Gravity Estimation . . . 47
4.3 Airfoil Selection . . . 47
4.3.1 Simulation Parameters . . . 48
4.3.2 Reynolds Number . . . 49
4.3.3 Proposed Methodology for Airfoil Selection . . . 49
4.4 Wing Design . . . 50
4.4.1 Simulation Parameters . . . 51
4.4.2 Proposed Methodology for Wing Design . . . 51
4.5 Winglet . . . 53
4.6 Control Surfaces . . . 54
4.7 Stability Analysis . . . 55
4.8 Performance Analysis . . . 55
4.9 Flight Envelope . . . 56
4.10 Aerodynamic Loads . . . 56
4.11 Structural Layout and CAD Model Design . . . 56
4.12 Composite Structure and Structural Analysis . . . 58

5 Preliminary Design **61**
5.1 Mass, Weight and Center of Gravity . . . 61
5.2 Airfoil Selection . . . 62
5.2.1 Reynolds Number . . . 62
5.2.2 Selection Results . . . 63
5.3 Wing Dimensions . . . 65
5.4 Winglet . . . 66
5.5 Control Surfaces . . . 67
5.6 Aerodynamic Characteristics . . . 68
5.7 Handling Qualities . . . 69
5.8 Performance . . . 70
5.8.1 Endurance and Range . . . 70
5.8.2 Constraint Analysis . . . 71
5.8.3 Power Curves . . . 72

5.9 Flight Envelope . . . 73
5.9.1 Maneuvering Loads . . . 73
5.9.2 Gust Loads . . . 73
5.9.3 Envelope Results . . . 74
5.10 Aerodynamic Loads . . . 75
5.11 Structural Layout and CAD Model Design . . . 76
5.12 Composite Structure . . . 78
5.12.1 Material Selection . . . 78
5.12.2 Stacking Sequence . . . 78
5.12.3 Manufacturing Process . . . 79
5.12.4 Wing Structural Mass . . . 81
5.13 Structural Analysis . . . 81
5.13.1 Mesh Details . . . 81
5.13.2 Boundary Conditions . . . 82
5.13.3 FEA Results . . . 84
5.14 3D Models . . . 86
5.14.1 Aerodynamic Design . . . 86
5.14.2 Structural Design . . . 86
5.14.3 Final Design . . . 87

6 Conclusions and Future Work **89**
6.1 Main Conclusions . . . 89
6.2 Future Work . . . 90

Bibliografia **93**

A Airfoil Selection **99**
A.1 Airfoil Measurements - Trip Location set to 1 . . . 99
A.2 Airfoil Measurements - Trip Location set to 0.3 . . . 101

B Aerodynamic Model **103**
B.1 Analysis Model . . . 103
B.2 Model Integration . . . 104

List of Figures

2.1 Airfoil nomenclature [1]. 6

2.2 Effect of leading edge radius on NACA 4412 airfoil (adapted) [2]. 6

2.3 Airfoils with different camber [3]. 7

2.4 Lift coefficient and lift-to-drag ratio of each airfoil for different angles of attack [3]. 7

2.5 Aerodynamic characteristics of airfoils with different relative thickness values (adapted) [4]. 8

2.6 Symmetrical airfoil lift and drag coefficient curves as functions of angle of attack [5]. 9

2.7 Wide and narrow buckets for two different airfoils and Reynolds number (adapted) [6]. 9

2.8 Method to evaluate the stall quality (adapted) [6]. 10

2.9 Airfoil lift and drag coefficient curves for two different Reynolds numbers (adapted) [5]. 11

2.10 Options for vertical wing positions (adapted) [7]. 12

2.11 Wing with negative twist (wash-out) [5]. 13

2.12 C_L/C_D versus angle of attack (a) and C_L versus C_D (b) for different aspect ratios [8]. 13

2.13 Wings with various taper ratios [7]. 14

2.14 Typical effect of taper ratio on the lift coefficient distribution [7]. 15

2.15 Five wings with different sweep angles (adapted) [7]. 15

2.16 (a) Dihedral and (b) anhedral (aircraft front view) [7]. 16

2.17 Lift load distribution over the semi-span of the wing: (a) non-elliptical; (b) elliptical [7]. 17

2.18 Pusher and tractor propeller arrangements on flying wing (adapted) [9]. . . . 20

2.19 Simple systems with positive, negative, and neutral static stability [5]. 20

2.20 Dynamic stability (adapted) [10]. 21

2.21 Stable, unstable and neutral longitudinal static stability (adapted) [10]. 22

2.22 Short-period dynamic mode [11]. 22

2.23 Phugoid dynamic mode [11]. 23
2.24 Static directional stability [12]. 24
2.25 Static lateral stability [12]. 24
2.26 Control system for tailless and conventional aircraft [13]. 25
2.27 Conventional winglet geometrical parameters [14]. 26
2.28 Typical structural layout of a wing for general aviation aircraft [1]. 26
2.29 Typical maneuvering envelope [15]. 29
2.30 Typical gust envelope [15]. 30
2.31 Composition of composite material. 31
2.32 Classification of composite material systems (adapted) [16]. 31
2.33 Isotropic, anisotropic, and orthotropic materials subjected to axial tension [17]. 32
2.34 A laminate made up of several lamina with different fiber orientations (adapted) [18]. 32
2.35 Sandwich structure. 33
2.36 Tail-sitter [19], Tilt-rotor [20], Tilt-wing [21], Rotor-wing [22] and Dual system [23] technologies. 36

3.1 Design process of a wing for integration with a multirotor UAV. 39
3.2 Dimensions of the frame and components of the UAV. 40
3.3 Configurations "+" and "×" representative of the frame orientation relative to the flight direction. 41
3.4 Wing shape possibilities of each configuration. 41
3.5 Conceptual design of a flying/blended wing for a VTOL UAV. 43

4.1 Wing aerodynamic and structural design process. 45
4.2 Planform sections and mesh characteristics. 51
4.3 Flow5 interface and simulation parameters. 52
4.4 Ansys project schematic and systems. 58
4.5 Details of the *Composite Failure Tool*. 59

5.1 Mass center position distribution of the UAV's components. 62
5.2 Wing planform. 66

5.3 Winglet planform. 67
5.4 Elevon size and parameters. 68
5.5 Aerodynamic characteristics of the wing with and without payload. 69
5.6 Available power and required power. 72
5.7 Maneuvering and gust loads (1) and combined envelope (2). 74
5.8 Lift distribution. 75
5.9 Bending moment. 75
5.10 Shear stress. 76
5.11 Wing-shaped solid body. 76
5.12 Spar solid bodies after *Combine* and *Extrude*. 76
5.13 Wing skin solid body. 77
5.14 Rib parts. 77
5.15 Wing structural components. 77
5.16 Manufacturing process of the main spar and orientations considered. 80
5.17 Mesh details of the structural components. 82
5.18 Boundary conditions applied to the structure. 83
5.19 Total deformation [mm]. 84
5.20 Inverse reserve factor. 85
5.21 Ribs equivalent stress. 85
5.22 Aerodynamic wing model - dimetric view. 86
5.23 Aerodynamic wing model - top view. 86
5.24 Final structural design with transparent wing skin and caps - dimetric view. . 86
5.25 Final wing model - dimetric view. 87
5.26 Final wing model - top view. 87
5.27 Final design - dimetric view. 87
5.28 Final design - top view. 87

A.1 Airfoil characteristics at 500,000 Re and with trip location set to 1. 99
A.2 Airfoil characteristics at 900,000 Re and with trip location set to 1. 100
A.3 Airfoil characteristics at 1,300,000 Re and with trip location set to 1. 100

A.4 Airfoil characteristics at 500,000 Re and with trip location set to 0.3. 101
A.5 Airfoil characteristics at 900,000 Re and with trip location set to 0.3. 102
A.6 Airfoil characteristics at 1,300,000 Re and with trip location set to 0.3. 102

B.1 Wing analysis model - dimetric view. 103
B.2 Wing analysis model - top view. 103
B.3 Wing analysis model - side view. 104
B.4 Aerodynamic wing model integrated with the multirotor's frame - dimetric view.104
B.5 Aerodynamic wing model integrated with the multirotor's frame - top view. . . 104

List of Tables

2.1 Criteria importance and performance of each UAV configuration. 37

3.1 Criteria importance and performance of each UAV configuration. 42

4.1 Considered airfoil selection. 47

4.2 Commonly used parameters for aileron and elevator sizing [7]. 54

5.1 Mass center positions, masses and weights of the UAV's components. 61

5.2 Center of gravity position, mass and weight of the UAV with payload. 62

5.3 Reynolds number for stall, cruise and max speed. 63

5.4 Results at Re $1,300,000$. 63

5.5 Results at Re $900,000$. 64

5.6 Results at Re $500,000$. 64

5.7 Overall airfoil performance. 64

5.8 Characteristics and performance of wing planforms with different wingspans. 65

5.9 Wing characteristics. 65

5.10 Winglet characteristics. 66

5.11 Elevon specifications. 68

5.12 Aerodynamic characteristics. 68

5.13 Static stability analysis. 69

5.14 Longitudinal dynamic stability flight quality results (without payload). 69

5.15 Lateral-directional dynamic stability flight quality results (without payload). . 69

5.16 Longitudinal dynamic stability flight quality results. 70

5.17 Lateral-directional dynamic stability flight quality results. 70

5.18 Range and endurance results of the UAV. 71

5.19 T-Motor AT5220 specifications [24]. 72

5.20 Combined envelope specifications. 74

5.21 Material characteristics and properties. 78

5.22 Composite details of each component. 79

5.23 Mass of each structural component. 81
5.24 Mesh details of each component. 82
5.25 Center of pressure distribution along the semi-span. 83
5.26 Element types, classification and application [25]. 84

Nomenclature

A	Aspect ratio	—
A_{dist}	Percentage of wing area subjected to non-disturbed flow	%
b	Wing span	m
b_a	Aileron span	m
b_e	Elevator span	m
b_h	Horizontal tail span	m
b_n	Elevon span	m
c	Chord length	m
c_a	Aileron chord	m
C_d	Drag coefficient	—
$C_{D_{\alpha_0}}$	Drag coefficient at 0 angle of attack	—
$C_{d_{min}}$	Minimum drag coefficient	—
c_e	Elevator chord	m
c_h	Horizontal tail chord	m
C_l	Lift coefficient	—
C_l/C_d	Lift-to-drag ratio	—
$C_{L_{\alpha_0}}$	Lift coefficient at 0 angle of attack	—
$C_{L_{\alpha_0}}/C_{D_{\alpha_0}}$	Lift-to-drag ratio at 0 angle of attack	—
$C_{l_{max}}$	Maximum lift coefficient	—
C_{l_α}	Subsonic lift coefficient curve slope relative to the angle of attack	—
C_{l_β}	Lift coefficient curve slope relative to the sideslip angle	—
C_m	Pitching moment coefficient	—
c_m	Mid chord	—
$C_{m_{mean}}$	Average pitching moment coefficient	—
C_{m_α}	Moment coefficient curve slope relative to the angle of attack	—
C_n	Yawing moment coefficient	—
c_{n_r}	Elevon root chord	m
c_{n_t}	Elevon tip chord	m
C_{n_β}	Yawing moment curve slope relative to the sideslip angle	—
c_r	Wing root chord	m
c_t	Wing tip chord	m
$\bar{c}$	Mean geometrical chord	[m]
E	Young's modulus	N/mm^2
E_{sb}	Battery specific energy	Wh/kg
G	Shear modulus	N/mm^2
g	Acceleration due to gravity	m/s^2
I	Importance	—
K	Gust alleviation factor	—
k	Ratio of two-dimensional lift curve slope to 2π	—
l_h	Distance from the tail quarter-chord to the wing quarter-chord	m

$\boldsymbol{M}$	Airfoil parameters maximum value vector	—
$\boldsymbol{m}$	Airfoil parameters minimum value vector	—
m_b	Battery mass	kg
m_{TO}	Aircraft takeoff mass	kg
$\boldsymbol{N}$	Wing parameters maximum value vector	—
$\boldsymbol{n}$	Wing parameters minimum value vector	—
n	Load factor	—
P	Performance function	—
P_{req}	Power required	W
R	Range	km
Re	Reynolds Number	—
S	Wing area	m^2
S_a	Aileron area	m^2
S_e	Elevator area	m^2
S_h	Horizontal tail area	m^2
S_n	Elevon area	m^2
T	Torque	Nm
t/c	Thickness ratio	—
U	Gust speed	m/s
u	Vertical gust velocity	m/s
V	Velocity	m/s
V_A	Positive maneuvering speed	m/s
V_C	Cruise speed	m/s
V_D	Dive speed	m/s
V_F	Negative maneuvering speed	m/s
v_h	Horizontal tail volume coefficient	—
V_{max}	Maximum speed	m/s
$V_{n_{max}}$	Speed at which the load is maximum	m/s
$V_{n_{min}}$	Speed at which the load is minimum	m/s
V_s	Stall speed	m/s
V_V	Vertical speed	m/s
W/S	Wing loading	kg/m^2
W_{TO}	Aircraft takeoff weight	kg

Symbols

α	Angle of attack	$^\circ$
α_{i_r}	Root angle of incidence	$^\circ$
α_{i_t}	Tip angle of incidence	$^\circ$
α_s	Stall angle of attack	$^\circ$
α_{toe}	Toe angle	$^\circ$
α_{twist}	Angle of twist	$^\circ$
β	Sideslip angle	$^\circ$
β_M	Mach number parameter (Prandtl-Glauert)	—
Γ	Dihedral angle	$^\circ$
$\delta_{a_{max}}$	Aileron maximum deflection	$^\circ$
$\delta_{e_{max}}$	Elevator maximum deflection	$^\circ$
Δx	2D Horizontal distance	—
Δy	2D Vertical Distance	—
η_{b2s}	Total system efficiency	—
η_p	Propeller efficiency	—
θ	Ply orientation	$^\circ$
λ	Taper ratio	—
Λ	Sweep angle	$^\circ$
$\Lambda_{c/2}$	Sweep angle at the mid chord	$^\circ$
μ	Dynamic air viscosity	kg/ms
μ_{mr}	Mass ratio	—
ν	Poisson's ratio	—
ρ	Air density	kg/m^3
φ	Cant angle	$^\circ$

Acronyms

AAM	Advanced air mobility
AC	Aerodynamic center
BW	Bucket width
CAD	Computer-aided design
CEiiA	Centre of Engineering and Product Development
CG	Center of gravity
FEA	Finite element analysis
FFPS	Forward flight propulsive system
IRF	Inverse reserve factor
LE	Leading edge
MAC	Mean aerodynamic chord
MTOM	Maximum takeoff mass
SM	Static margin
SQ	Stall quality
TE	Trailing edge
UAV	Unmanned aerial vehicles
VTOL	Vertical takeoff and landing

Chapter 1

Introduction

This chapter contains the motivation behind this dissertation in Section 1.1, an introduction to the company and business unit that are involved with this project in Section 1.2, the main objectives in Section 1.3 and an outline of the dissertation in Section 1.4.

1.1 Motivation

This project initiated following an interaction with the team responsible for the Advanced Air Mobility (AAM) business unit at CEiiA. In a conversation about the advancement of technology in the field of air mobility and the development of new and innovative solutions for air transportation, the business unit presented their most recent project, designated as CASTA.

CASTA was presented as a cutting-edge, multirotor modular platform designed specifically for testing and validating enabling technologies for advanced air mobility. It is intended to operate in semi-urban and urban environments, with safety being a top priority. The platform can carry up to 20kg of payload in a four-rotor configuration and up to 40kg in an eight-rotor configuration, providing the versatility needed for a wide range of tasks, such as in the agricultural and transportation industries. Some of its key specifications and features include a three-meter diameter footprint, electric brushless motor propulsion, lithium batteries, a flight termination system, and a quick-folding system.

One limitation of normal multirotors is their inability to perform long-range flights, which restricts their usage in missions that require covering long distances. To address this limitation, a project was proposed to design a wing that can be attached to the multirotor for long-range missions but can be removed for missions where a smaller footprint is required, such as in urban environments.

This project allows for the involvement in every major subject related to aircraft development, such as aerodynamics, structures, performance and computer-aided design (CAD) modeling. It also enables a better understanding of the steps and iterative nature of developing components or systems for an aircraft, from the planning process to the final design and manufacture of the component.

Another interesting aspect of this project is the business unit's intention to use the results from the wing design to manufacture and integrate into the CASTA project. This opens up the possibility of seeing the physical results of this project in the future. Additionally, there is the benefit of being able to work on-site at the CEiiA headquarters, providing the opportunity to collaborate with a team focused on developing new and innovative projects.

1.2 CEiiA and AAM business unit

CEiiA is a Portuguese Centre of Engineering and Product Development that designs, implements and operates technological solutions to push innovation in the aeronautic, urban mobility, automotive, ocean, and space sectors. It was founded in 1999 and, since then, it has been involved in many relevant projects in collaboration with many different companies, such as Embraer, Leonardo, Daher, and others. CEiiA also develops their own projects within their business units.

The AAM is a business unit at CEiiA with a special focus on the aeronautical industry and the aim of developing enabling technologies to accelerate the safe implementation of drone delivery for logistics and emergency medical responses. Their multidisciplinary team is working in collaboration with strategic partners and authorities to create value, expand knowledge, and develop mechanisms and products from scratch.

1.3 Objectives

The main objective of this project is to design a wing that can be integrated into the multirotor developed by the AAM business unit. Essentially, the multirotor will be adapted into a fixed-wing vertical takeoff and landing (VTOL) unmanned aerial vehicle (UAV), retaining its vertical takeoff and landing capabilities while also acquiring the capability to perform long-range missions.

The design of the wing can be broken down into the following main tasks:

1. Determine feasible configurations for the integration of a wing with the multirotor and create an initial concept;
2. Create an aerodynamic design of the wing, considering the requirements of the business unit and the constraints imposed by the geometry of the multirotor;
3. Conduct stability and performance analysis;
4. Determine the flight envelope and the aerodynamic loads generated during flight;
5. Establish the structural configuration of the wing and produce a CAD model of that structure;
6. Determine the stacking sequence of lamina that compose the structural components of the wing;
7. Establish a feasible manufacturing process for the defined components;
8. Perform a finite element analysis (FEA) on the final structure design.

1.4 Dissertation Outline

This dissertation is organised into six chapters:

Chapter 1 - Introduction. This chapter presents the motivation behind this dissertation, the company and business unit involved in project, the main objectives, and the dissertation outline;

Chapter 2 - Background and Tools. This chapter presents the theoretical foundations of aircraft design, the state of the art related to VTOL UAVs, and the tools employed to design the wing and perform the desired analyses;

Chapter 3 - Conceptual design. This chapter covers the requirements and constraints of the project, the configuration alternatives to integrate the wing in the multirotor, and the initial concept of the wing;

Chapter 4 - Design Methodology. This chapter outlines the steps implemented and the decisions made in the preliminary design process of the wing.

Chapter 5 - Preliminary design. This chapter presents the results obtained through the methodology presented and clarifies the chosen parameters for the design;

Chapter 6 - Conclusions and future work. This chapter presents the main conclusions, and provides insights of possible future work related to the project.

Chapter 2

Background and Tools

This chapter introduces the main concepts that were explored throughout the development of this dissertation in Section 2.1. It also includes a review on VTOL UAVs in Section 2.2, and a description of the tools that were employed to complete this work in Section 2.3.

2.1 Theoretical Foundations

2.1.1 Airfoils and Aerodynamics

An airfoil is a shape designed to produce a useful reaction from the air when it moves through it and is a fundamental component of aerodynamics used extensively in various industries, including aviation, aerospace, wind energy, and hydrodynamics, and applications such as airplane wings, helicopter blades, wind turbine blades, and other applications where lift is required to generate movement or support weight. A wing's airfoil shape is the cross-section perpendicular to both the leading and trailing edges and is chosen by aircraft designers in such a way as to obtain optimum pressure distribution on the upper and lower wing surfaces so that the required lift is created at the lowest drag cost [7].

When moving through the air, the shape and orientation of an airfoil will result in changes of velocity and static pressure on the upper and lower surfaces of the airfoil which generates aerodynamic forces, as well as boundary-layer profiles, transition characteristics and separation characteristics [5]. Cruise speed, takeoff and landing distances, stall behaviour, roll stability, manoeuvrability and the overall effectiveness of the aerodynamic system throughout flight are all impacted by the airfoil design [26].

2.1.1.1 Airfoil Design and General Features

When designing an airfoil, the first step is to create a list of the desired characteristics, such as operational lift coefficients, maximum lift values, desirable entry into the post-stall region, minimum drag values, extent of laminar flow, pitching moment coefficient, and geometric characteristics like thickness and its location along the chord. These characteristics can vary based on conditions such as Mach number and Reynolds number. To that end, airfoils are usually designed using one of two methods: direct analysis or inverse design. Nowadays, this is done with computer applications such XFLR5 (which runs Xfoil in the background), and other two-dimensional computer softwares [1]. Figure 2.1 depicts a typical airfoil section along with several geometric parameters.

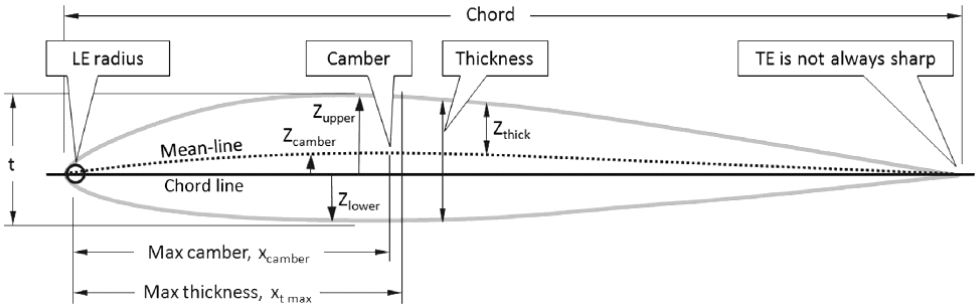

Figure 2.1: Airfoil nomenclature [1].

Chord Line, Leading Edge and Trailing Edge

The leading edge (LE) and trailing edge (TE) are the chord line's most forward and backward locations, respectively. A straight line traced from the leading edge to the trailing edge of the airfoil is referred to as the chord line and the exact distance measured between those two points is simply referred to as the chord of the airfoil.

Leading Edge Radius

The leading edge of the airfoil is defined by a radius, tangent to the upper and lower surfaces. The radius of the leading edge has a significant impact on aerodynamics, including lift, drag, and stall characteristics. A wider LE radius has the advantage of maintaining air attachment at increased angles of attack, leading to a higher stall angle and more generated lift for takeoff and landing. However, an excessively wide leading edge can result in excessive drag [26].

To better understand the effect of the LE radius on the lift-to-drag ratio (C_l/C_d) across different angles of attack (α), Figure 2.2 provides a visual representation of this effect for the same airfoil modified with eight different LE radius.

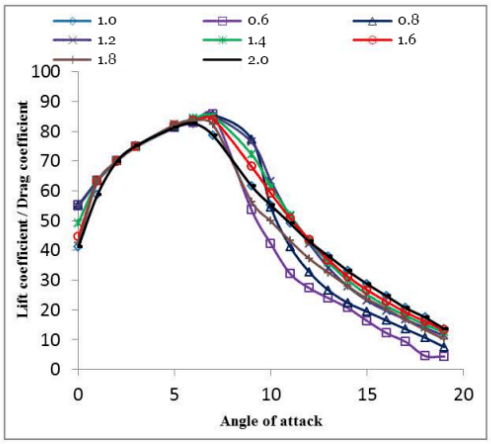

Figure 2.2: Effect of leading edge radius on NACA 4412 airfoil (adapted) [2].

Camber

The mean camber line is a curved line that is traced from the leading edge to the trailing edge, positioned equidistantly between the upper and lower surfaces of the airfoil. It significantly impacts the downwash behind the airfoil and consequently, the amount of lift generated. The maximum camber of the airfoil is the largest distance between the chord line and mean camber lines. Generally, a larger camber results in greater maximum lift from the airfoil, and a thicker airfoil leads to a higher stall angle-of-attack and increased drag. However, there are exceptions to these rules [1].

Positive camber means that the upper surface of the wing is more curved than the lower surface, while negative camber means the opposite. The shape and position of the camber can be adjusted to optimise the performance of the wing for different flight conditions. In the case of the symmetrical airfoil, the lower surface is a mirror copy of its upper surface, meaning that its mean camber line coincides with its chord line and can be classified as uncambered [5].

One method for achieving natural stability in a tailless or flying-wing aircraft is to use a ”S” shaped camber line with an upwards reflex at the trailing edge [26]. As an example, Figures 2.3 and 2.4 illustrate the outline of four different camber airfoils, all of which have the same chord length.

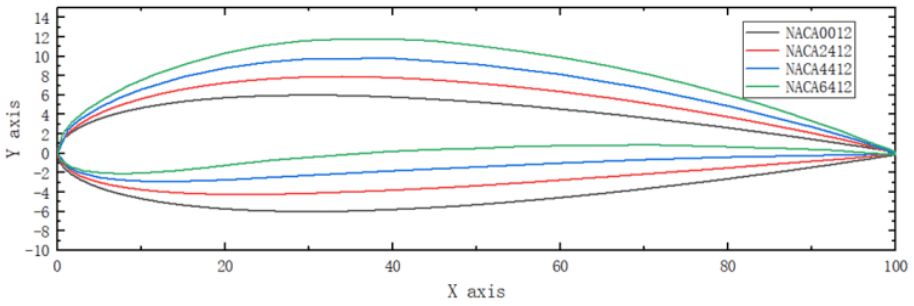

Figure 2.3: Airfoils with different camber [3].

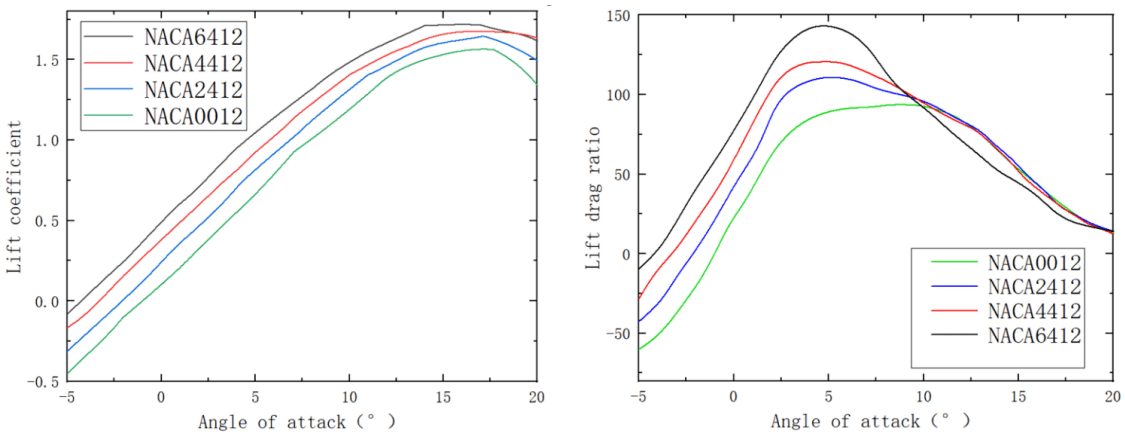

Figure 2.4: Lift coefficient and lift-to-drag ratio of each airfoil for different angles of attack [3].

Thickness

The thickness of an airfoil is the distance measured perpendicular to the chord line from its upper surface to the lower surface and it is typically expressed as a percentage of the chord length (c). The maximum thickness of the airfoil divided by its chord is referred to as the airfoil thickness ratio (t/c) and it affects the aerodynamic characteristics of the airfoil [26]. Figure 2.5 depicts the aerodynamic characteristics of four airfoils with different thickness ratios.

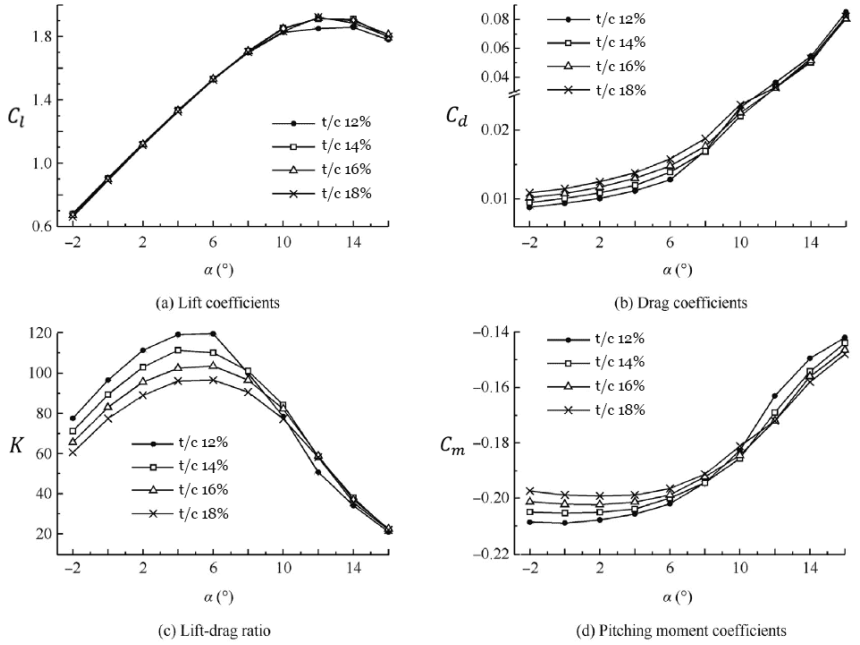

Figure 2.5: Aerodynamic characteristics of airfoils with different relative thickness values (adapted) [4].

2.1.1.2 Lift and Drag Coefficient Curves

By definition, the lift force acts perpendicular to the relative wind, while the drag force acts parallel to the relative wind. The lift coefficient (C_l) and drag coefficient (C_d) can be obtained using Equations 2.1 and 2.2, where ρ is the air density, V is the reference air velocity [7].

$$C_l = \frac{Section\ lift}{\frac{1}{2}\rho V^2 c} \tag{2.1}$$

$$C_d = \frac{Section\ drag}{\frac{1}{2}\rho V^2 c} \tag{2.2}$$

It is worth noting that the characteristics of two-dimensional airfoils are indicated using lowercase subscripts, while the characteristics of a three-dimensional wing are indicated using uppercase subscripts.

Typically, the lift and drag coefficient curves are plotted relative to the angle of attack, as illustrated in Figure 2.6.

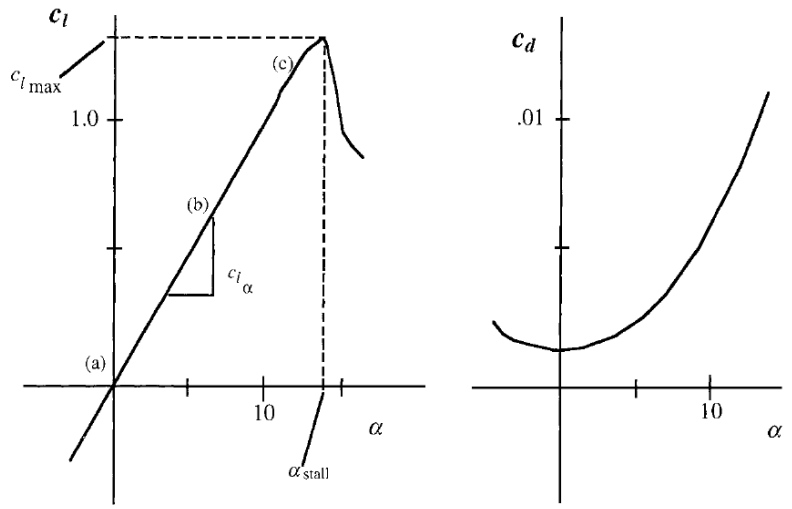

Figure 2.6: Symmetrical airfoil lift and drag coefficient curves as functions of angle of attack [5].

2.1.1.3 Lift Coefficient Bucket Width

The bucket width is a parameter that results from the difference between the maximum ($C_{l_{max}}$) and minimum ($C_{l_{min}}$) lift coefficients within the interval where the C_d is close to the minimum drag coefficient ($C_{d_{min}}$). These lift coefficients represent the operating range in which an airfoil has high efficiency.

A wider lift coefficient bucket presents a significant advantage for both the UAV designer and the operator, providing a larger margin of deviation within the flight envelope without imposing significant penalties on the range and endurance of the aircraft [6].

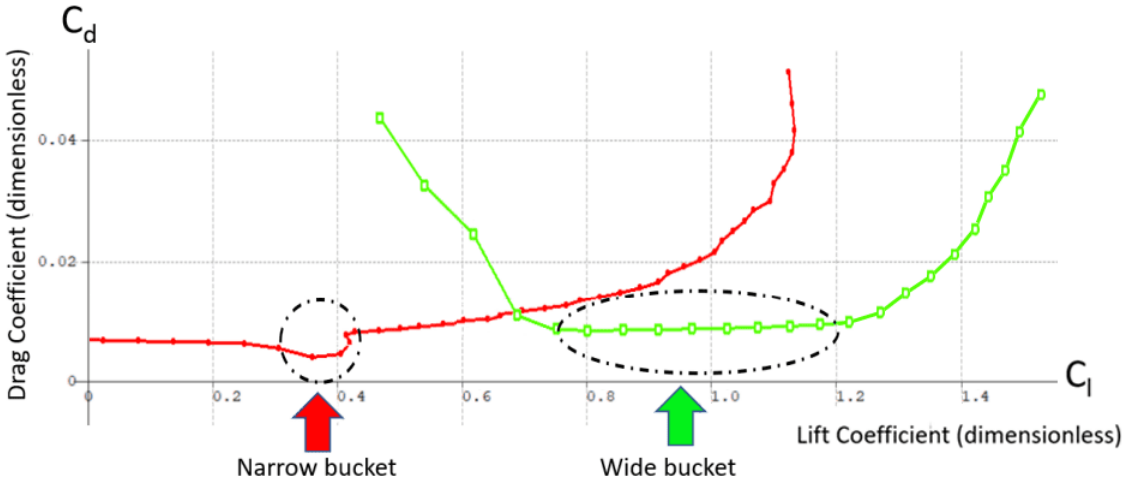

Figure 2.7: Wide and narrow buckets for two different airfoils and Reynolds number (adapted) [6].

2.1.1.4 Stall Quality

By definition, the quality of stall performance is a predictive measurement referring to the behaviour of the airfoil after the stall angle is reached. In Figure 2.8, there is a C_l-α diagram on the left, and a zoomed section of three hypothetical stall curves on the right. The preferred order in terms of stall quality is green > orange > red.

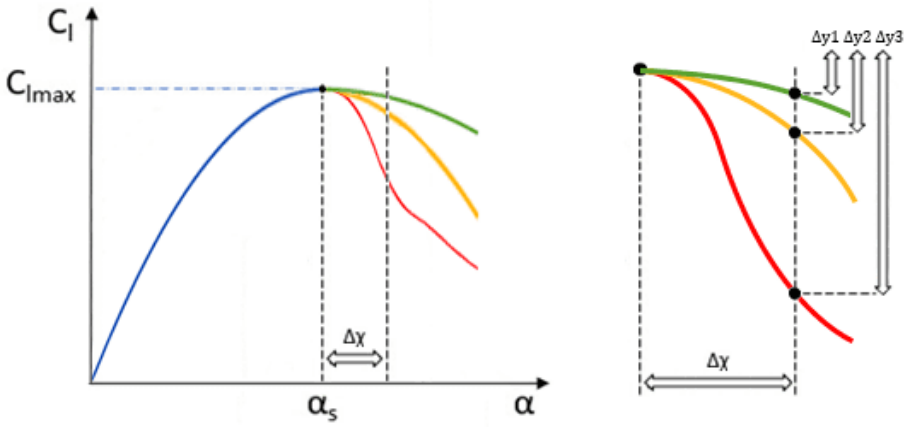

Figure 2.8: Method to evaluate the stall quality (adapted) [6].

To evaluate the stall quality, a vertical line is introduced at a distance Δx from the stall angle, intersecting the three stall curves. Subsequently, the distances between the $C_{l_{max}}$ and the intersection points ($\Delta y1$, $\Delta y2$, and $\Delta y3$) are measured. The curve that exhibits the smallest Δy value, indicating the least decrease in lift coefficient beyond the stall point, corresponds to the highest stall quality [6].

2.1.1.5 Moment Coefficient, Center of Pressure and Aerodynamic Center

The pressure and shear stress distribution around asymmetrical airfoils generates lift and drag forces, as well as a moment. This moment is known as the pitching moment (C_m) and tends to rotate the leading edge of the airfoil either upward or downward, depending on the shape of the airfoil [5]. The pitching moment coefficient is defined as follows:

$$C_m = \frac{Section\ moment}{\frac{1}{2}\rho V^2 c^2} \tag{2.3}$$

The aerodynamic center (AC) of an airfoil is the point where the pitching moment remains nearly constant with variations in the angle of attack. For flights at subsonic speeds, this point is typically located at approximately 25% of the chord length from the leading edge of the airfoil and is known as the quarter-chord point. This point is commonly used as the reference for lift, drag, and pitching moment data of the airfoils [26].

The center of pressure (CP) is the point where the vertical forces balance, and consequently,

the moment at this point equals to zero. This point typically oscillates between the leading edge and the AC as the angle of attack changes [5].

2.1.1.6 Reynolds Number

The Reynolds number (Re) significantly impacts the parasitic drag coefficient and the timing and location of flow separation, regardless of whether the flow is laminar or turbulent. Therefore, it is importing to account for this factor, as the behaviour of an airfoil can significantly differ between two distinct Reynolds numbers. The Re represents the ratio of inertial forces to viscous forces within a fluid flow and is a critical factor in boundary layer analysis [26]. The definition of Reynolds number is presented in Equation 2.4, where μ is the dynamic air viscosity.

$$Re = \frac{\rho V c}{\mu} \tag{2.4}$$

An increase in Reynolds number prompts a shift from a smooth, predictable flow (laminar flow) to a chaotic, unpredictable flow (turbulent flow) in the boundary layer nearer to the leading edge of an airfoil. This change incurs an increase in skin-friction drag, but also postpones separation and diminishes pressure drag. At lower angles of attack, this adjustment in the balance between skin friction and pressure drag may either increase or reduce the overall drag at elevated Reynolds numbers. However, at higher angles of attack, where separation and pressure drag are predominant, the postponed separation brings about a reduction in pressure drag, leading to a lower total drag at higher Reynolds numbers [5].

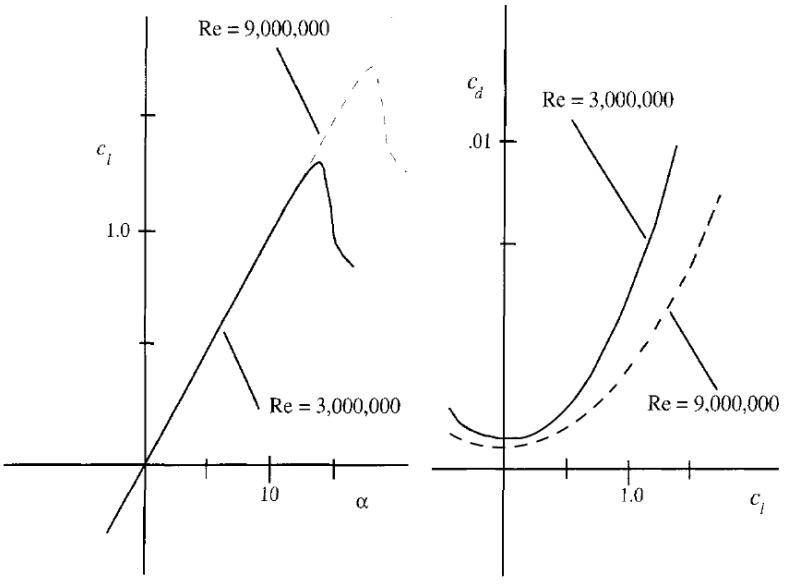

Figure 2.9: Airfoil lift and drag coefficient curves for two different Reynolds numbers (adapted) [5].

The lift coefficient and drag coefficient curves for an airfoil at two different Reynolds numbers

are displayed in Figure 2.9 where is possible to visualise that the airfoil experiences better lift-to-drag ratio at higher Reynolds numbers.

2.1.2 Wing Configuration

The wing is a lifting surface whose primary function is to generate lift. Its shape influences the airflow over and under it, creating a pressure difference between the top and bottom surfaces, which generates an upward force that lifts the aircraft. However, the wing also produces two other forces: drag, the force that resists the aircraft's forward motion caused by the air resistance to the wing's shape, and the pitching moment, the tendency of the aircraft to pitch downwards or upwards due to the wing's lift. Therefore, the wing design requires careful consideration and attention to detail considering a balance in trade-offs between lift, drag, and pitching moment to ensure a safe, efficient, and stable flight. This can be achieved by carefully selecting the wing's shape, size, and angle of attack, among other factors [7].

2.1.2.1 Vertical Wing Location

One of the key wing parameters that can be established during the early stages of wing design is the vertical location of the wing with respect to the center line of the fuselage and this decision has a direct impact on the design of many critical aircraft components. In essence, there are four options for the placement of the wing, shown in Figure 2.10 [7].

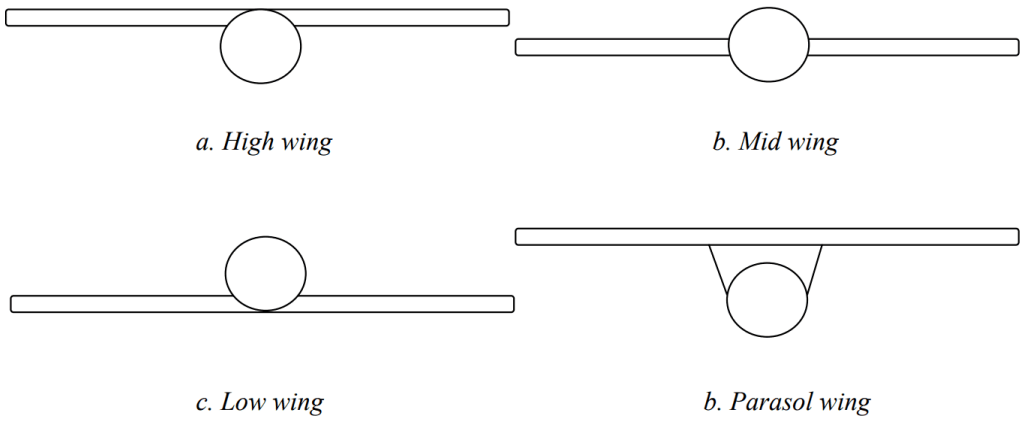

Figure 2.10: Options for vertical wing positions (adapted) [7].

Each of these configurations has its own advantages and disadvantages, and they are used in various aircraft types for different purposes. The vertical location of the wing affects the aircraft's stability, manoeuvrability, and overall performance.

2.1.2.2 Incidence and Twist

During flight, the chord line of a wing section may not align parallel to the relative wind. The angular difference between the chord line of a specific section and the relative wind is known

as the geometric angle of incidence (α_i). The concept of incidence can be extended to the twist of a wing. This means that if the angle of incidence is not uniform across all sections, the wing is considered twisted. If the incidence angle increases towards the tip, the angle of twist (α_{twist}) is positive and it is referred to as wash-in. Conversely, if the incidence angle decreases towards the tip, the α_{twist} is negative and is known as wash-out [27]. Figure 2.11 displays an example of a wing with negative twist.

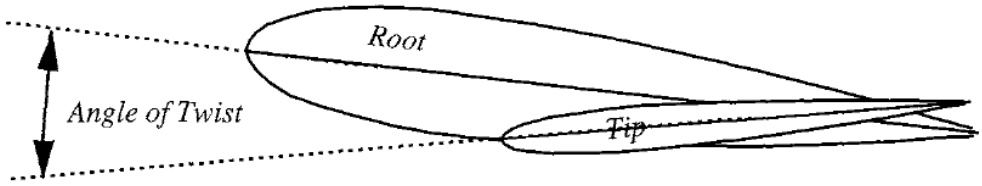

Figure 2.11: Wing with negative twist (wash-out) [5].

The incorporation of twist in wing design aims to prevent the wingtip from stalling before root. This allows the aileron to to maintain control of the aircraft even after the wing root has stalled, which increases the safety of the aircraft in the event of a wing stall. Additionally, it helps approximate the lift distribution into an elliptical shape. However, the downside of wing twist is that it reduces the overall lift produced, which is undesirable [27].

2.1.2.3 Aspect Ratio

The aspect ratio (A) is simply represented by the span (b) squared divided by the wing area (S), as presented in Equation 2.5.

$$A = \frac{b^2}{S} \tag{2.5}$$

Figure 2.12 displays the impact of the aspect ratio in the lift and drag coefficients of a wing.

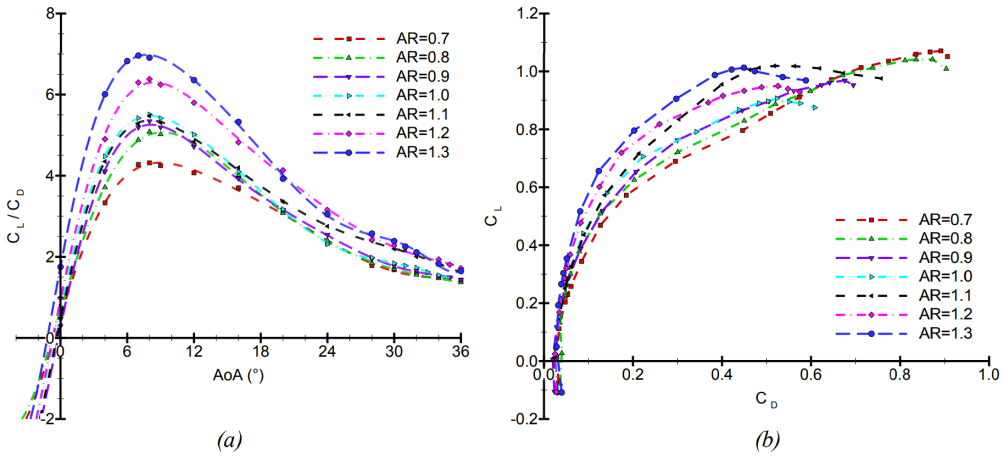

Figure 2.12: C_L/C_D versus angle of attack (a) and C_L versus C_D (b) for different aspect ratios [8].

Research indicates that a wing with a high aspect ratio is more efficient in generating lift and

experiences less induced drag at a given lift coefficient than a wing with a low aspect ratio. This can be attributed to the fact that the tip vortex affects a smaller portion of a high aspect ratio wing, resulting in less lift loss and less drag increase due to tip effects compared to a low aspect ratio wing of equal area [26].

2.1.2.4 Taper Ratio

The taper ratio (λ) is defined as the ratio between the tip chord (c_t) and the root chord (c_r), and it significantly influences the lift distribution across the wing's span.

$$\lambda = \frac{c_t}{c_r} \tag{2.6}$$

Usually ranging between zero and one, the taper ratio is typically applied to obtain a reduced tip chord length, resulting in rectangular (λ=1), trapezoidal (0<λ<1) and delta (λ=0) shaped wings [7].

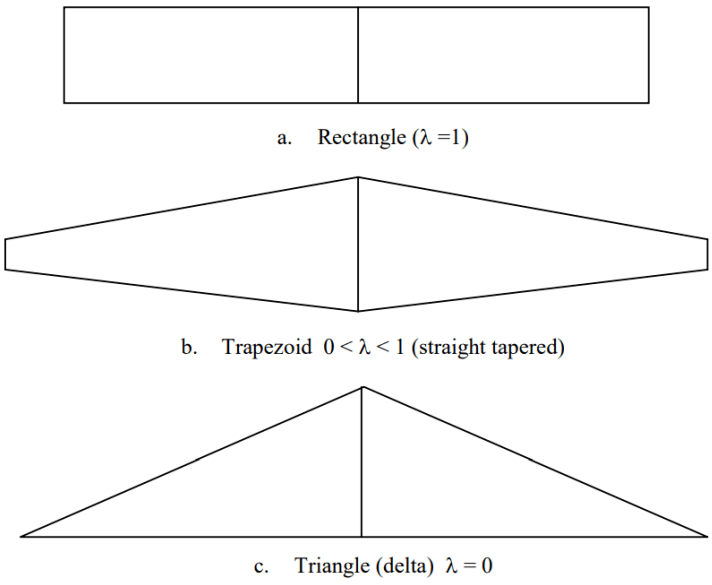

Figure 2.13: Wings with various taper ratios [7].

Wing taper is a strategy employed to reduce the inefficiencies of untapered wings. Despite increasing manufacturing costs, the taper improves the distribution of lift across the wing. In fact, when the taper ratio of an unswept wing is 0.45, the generated lift distribution closely approximates the ideal elliptical pattern, resulting in a drag due to lift only slightly higher than that of an elliptical wing [26].

Increasing the wing taper also reduces the weight of the wing by repositioning the center of gravity (CG) of each wing section closer to the fuselage center line, which results in a lower bending moment at the wing root, requiring a lighter wing spar and structure. Furthermore, this repositioning of the CG reduces the wing mass moment of inertia about the longitudinal

axis improving the aircraft lateral control, with the delta wing being the most effective configuration if this is a requirement. Additionally, the wing taper has influence on the aircraft static lateral stability due to the sweep angle generated by the taper [7].

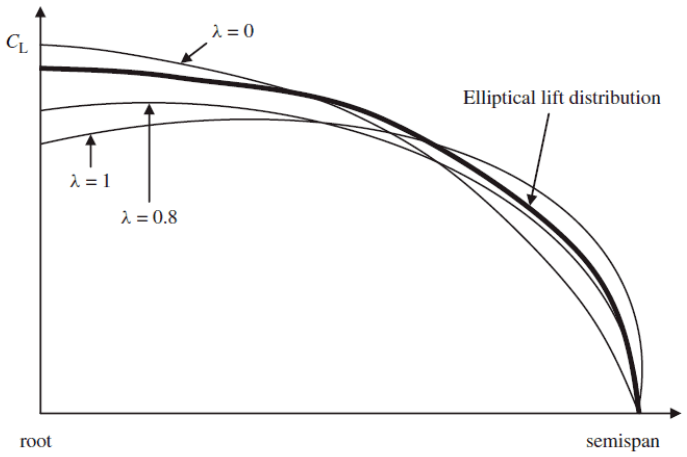

Figure 2.14: Typical effect of taper ratio on the lift coefficient distribution [7].

2.1.2.5 Sweep Angle

A swept wing is a type of wing configuration that deviates from a straight sideways direction by angling either backward or, in some cases, forward from its root. When examining an aircraft from a top-down perspective, the sweep angle (Λ) of a wing represents the angle formed between a line drawn along the wing's span at a consistent percentage of the chord length and a line perpendicular to the centerline of the aircraft [27].

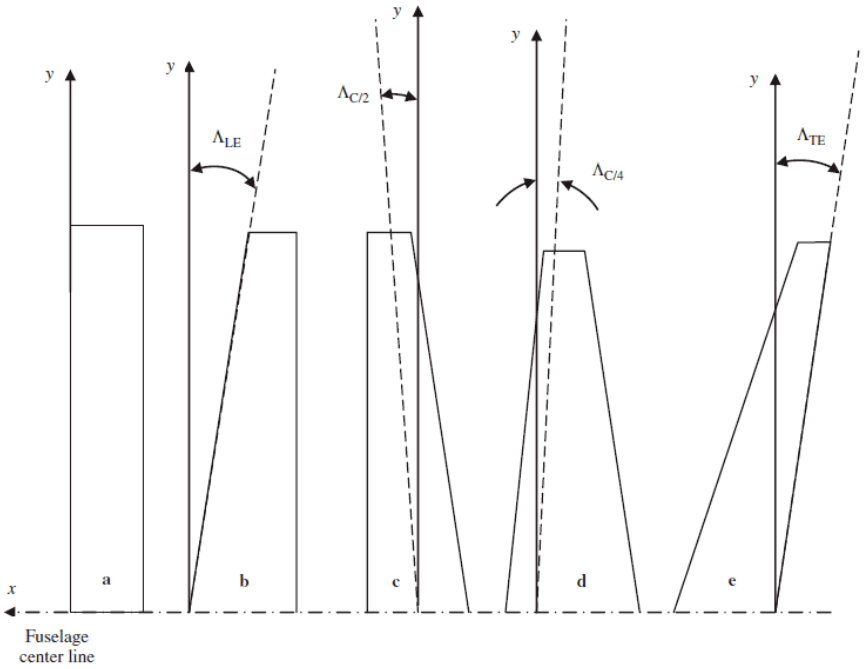

Figure 2.15: Five wings with different sweep angles (adapted) [7].

The sweep angle of an aircraft's wing is employed for various design goals, including the improvement of the aerodynamic performance at different flight speeds by delaying the onset of the compressibility effect, increasing lift, reducing drag, and managing pitching moments during flight. Other purposes of wing sweep are to adjust the aircraft's center of gravity, which can significantly impact its stability and handling [7].

2.1.2.6 Dihedral Angle

The wing dihedral (Γ) can be described as the angle at which the wing is positioned in relation to the horizontal plane when viewed from the front.

When the wing tip is positioned above the horizontal plane, the wing angle is referred as positive dihedral. Conversely, when the wing tip is positioned below the horizontal plane, the angle is known as negative dihedral or anhedral, as depicted in Figure 2.16 [7].

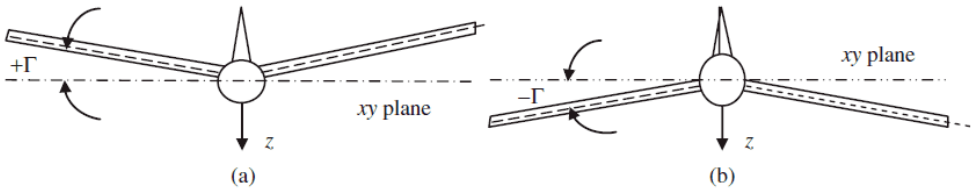

Figure 2.16: (a) Dihedral and (b) anhedral (aircraft front view) [7].

The main objective of implementing a wing dihedral is to enhance the aircraft's lateral stability, which refers to the aircraft's ability to regain its original trim level-wing flight position in the event of a disturbance like gusty winds. This type of stability is also known as dihedral stability because the wing's dihedral angle generates the required restoring rolling moment.

2.1.2.7 Lift and Load Distribution

According to Prandtl wing theory, the minimum drag resulting from lift, commonly known as induced drag, is achieved when the lift distribution is elliptical. This optimal distribution naturally is achieved when the wing planform is shaped like an ellipse. However, manufacturing an elliptical wing is a challenging and costly endeavor [26].

In comparison to the elliptical planform, the rectangular planform has a few advantages, including lower manufacturing cost and ease of construction, but it is not an optimal choice from an aerodynamic perspective as it has excessive chord length towards the tip which results in the wing generating more lift at the tip than is desirable. Consequently, the spanwise lift distribution of an untwisted rectangular wing is far from elliptical which generates approximately 7% more drag due to lift than an elliptical wing with the same aspect ratio [26].

In addition, the lift distribution determines the bending moment at the wing root. Compared to a rectangular wing, an elliptical wing has a lift load distribution centered closer to the wing root, resulting in lower bending stress concentration at the wing root, leading to lighter

wing structures. Moreover, having the center of the load distribution closer to the fuselage center line is beneficial for lateral control as it enables faster rolling of the aircraft due to the reduced mass moment of inertia [7]. Figure 2.17 displays the lift load distributions for both the elliptical and non-elliptical wing.

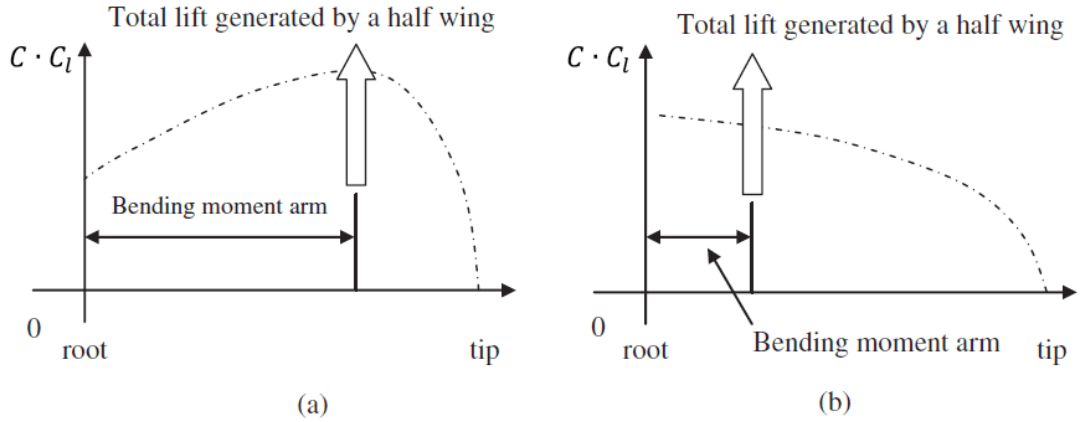

Figure 2.17: Lift load distribution over the semi-span of the wing: (a) non-elliptical; (b) elliptical [7].

2.1.3 Performance

Aircraft performance analysis involves predicting the capabilities of an aircraft, including its speed, service ceiling, maneuverability, payload capacity, range, endurance, and runway requirements for takeoff and landing [5].

2.1.3.1 Constraint Analysis

A constraint analysis is conducted to ensure an aircraft meets specific performance requirements. This analysis evaluates the required wing area or power plant for the design across various flight phases, such as takeoff, climb, cruise, descent, and landing. It also considers the constraints imposed by different in-flight maneuvers such as turns, rolls, and loops [1].

By expressing the performance characteristics of an aircraft in terms of its thrust-to-weight ratio (T/W), it is possible to determine the amount of thrust required for the aircraft to achieve certain desired parameters. The following are some examples of constraints typically applied to fixed-wing aircraft:

- Level constant-velocity turn: Determines the T/W required to maintain a specific banking load factor at a specific airspeed and altitude, without losing altitude.

$$\frac{T}{W_{TO}} = \frac{1}{2}\rho V_C^2 \left[\frac{C_{D_{min}}}{(W/S)} + \frac{(W/S)}{\pi A e} \left(\frac{n}{\frac{1}{2}\rho V_C^2} \right)^2 \right] \tag{2.7}$$

- Rate of climb: Determines the T/W required to achieve a given rate of climb.

$$\frac{T}{W_{TO}} = \frac{V_V}{V_C} + \frac{\frac{1}{2}\rho V_C^2 C_{D_{min}}}{(W/S)} + \frac{(W/S)}{\frac{1}{2}\rho V_C^2 \pi A e} \tag{2.8}$$

- Cruise speed: Determines the T/W required to achieve a given cruising speed at a desired altitude.

$$\frac{T}{W_{TO}} = \frac{\frac{1}{2}\rho V_C^2 C_{D_{min}}}{(W/S)} + \frac{(W/S)}{\frac{1}{2}\rho V_C^2 \pi A e} \tag{2.9}$$

In the above equations, W_{TO} is the aircraft takeoff weight, n is the load factor, V_C is the cruise speed, V_V is the vertical speed, W/S is the wing loading and e is the efficiency/Oswald factor.

2.1.3.2 Endurance and Range

For many aircraft designs, the ability to fly long distances or for extended periods of time is a crucial requirement. The range and endurance of an aircraft are influenced by several factors, including its aerodynamics, propulsion system characteristics, battery capacity, and operational methods [5].

The endurance of an electric aircraft during level flight at a specified velocity is represented by Equation 2.10.

$$E = \frac{L}{D}\frac{E_{sb}\eta_{b2s}\eta_p}{gV}\frac{m_b}{m_{TO}} \tag{2.10}$$

where E_{sb} is the battery specific energy in Wh/kg, η_{b2s} is the total system efficiency from battery to motor output shaft, η_p is the propeller efficiency, V is the velocity in m/s, m_b is the mass of the batteries in kg, m_{TO} is the takeoff mass of the aircraft, also in kg [26].

The range of an electric aircraft can be calculated by simply multiplying the flight time by the velocity, resulting in Equation 2.11.

$$R = \frac{L}{D}\frac{E_{sb}\eta_{b2s}\eta_p}{g}\frac{m_b}{m_{TO}} \tag{2.11}$$

2.1.3.3 Thrust and Power

In order for an airplane to maintain steady level flight, it must achieve equilibrium by generating lift equal to its weight and producing thrust (T) equal to its drag. This means that the airplane's drag determines the amount of thrust required to maintain steady level flight [10].

The drag force is calculated using Equation 2.12.

$$T = D = \frac{1}{2}\rho V^2 S C_D \tag{2.12}$$

The total three-dimensional drag coefficient is calculated by adding the parasite drag coefficient (C_{D_0}) and the induced drag coefficient (C_{D_i}) together, as demonstrated in Equation 2.13.

$$C_D = C_{D_0} + C_{D_i} = C_{D_0} + \frac{C_L^2}{\pi A e} \tag{2.13}$$

The three-dimensional lift coefficient is calculated using Equation 2.14.

$$C_L = \frac{W}{\frac{1}{2}\rho V^2 S} \tag{2.14}$$

The power required for flight is determined by both the thrust required and the flight velocity, as shown in Equation 2.15.

$$P = TV \tag{2.15}$$

All equations presented in this section are derived from [1].

2.1.3.4 Propeller Location

There are two main options for the propeller location on an aircraft: a “tractor” installation, which pulls the aircraft with the propeller in the front, and a “pusher” installation, which pushes the aircraft with the propeller in the rear. The decision between these two options can significantly influence the design of the aircraft and requires careful consideration [26].

The tractor configuration allows the propeller to function in undisturbed flow, which maximises its efficiency and performance. However, the propeller rotation at the front of the aircraft generates a swirling airflow, vortices and helicity that can disrupt the laminar nature of the airflow over the wing. This increases aerodynamic drag and reduces lift, which leads to a decrease in the overall aerodynamic efficiency of the wing [26].

On the other hand, in a pusher configuration, the propeller creates a slipstream in the rear, allowing the aircraft to fly in undisturbed flow, thus reducing its skin-friction drag. Then again, having the propeller at the rear subjects it to the ingestion of turbulent airflow from the fore body and wing, which can lead to a decrease in its efficiency and performance, reducing the aircraft’s speed and altitude capabilities [9]. Figure 2.18 displays both the “pusher” and “tractor” configurations.

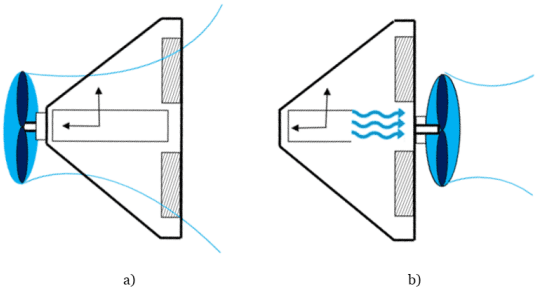

Figure 2.18: Pusher and tractor propeller arrangements on flying wing (adapted) [9].

2.1.4 Stability

The concept of stability refers to the ability of a system, after being perturbed, to restore its equilibrium state by itself. A system is considered stable if two types of stability are achieved: the static stability and the dynamic stability [26].

2.1.4.1 Static Stability

The static stability is classified into three types: positive static stability, negative static stability, and neutral static stability [5]:

A system is considered statically stable if, after being disturbed from its equilibrium position, the resulting forces and moments acting on the system tend to bring it back towards its equilibrium position. On the other hand, a system is considered statically unstable if, when disturbed from its equilibrium position, the resulting forces and moments acting on the system cause it to move further away from its equilibrium position. In the case of a neutrally stable system, the moments remain zero regardless of the disturbance, resulting in a system that remains in constant equilibrium [28]. Figure 2.19 depicts three systems representing the different static stability responses.

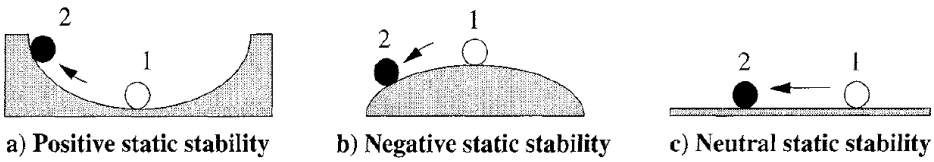

Figure 2.19: Simple systems with positive, negative, and neutral static stability [5].

2.1.4.2 Dynamic Stability

The dynamic stability describes the behaviour of the aircraft over time following its initial static stability response. A system is considered dynamically stable if it can reduce distur-

bances over time.This requires the system to have positive damping, meaning that the forces and moments acting on the system counteract the disturbances. Conversely, a dynamically unstable system amplifies disturbances due to forces and moments acting in alignment with those disturbances. This is also known as negative damping and prevents the system from reaching equilibrium. It is important to note that a statically stable aircraft can either be dynamically stable or unstable, meaning that static stability does not guarantee dynamic stability [28]. Figure 2.20 shows the possible combinations between static and dynamic stability.

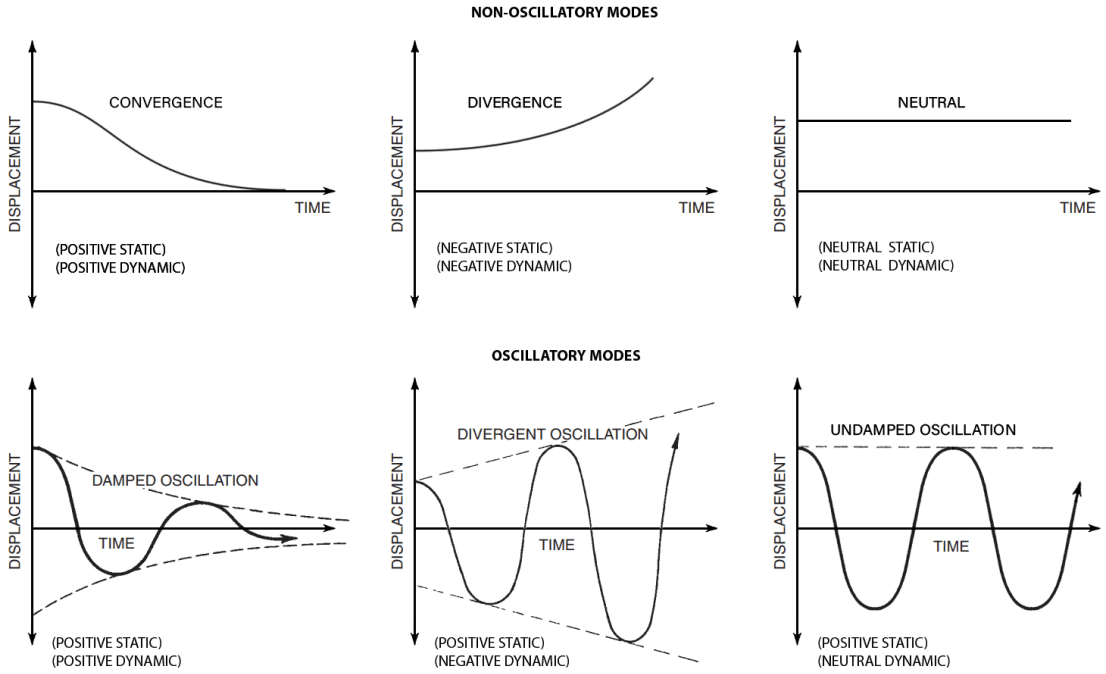

Figure 2.20: Dynamic stability (adapted) [10].

2.1.4.3 Longitudinal Stability

The longitudinal stability refers to the aircraft's response to disturbances in the pitch axis. Those disturbances result in variations in the vertical position and angle of attack of the aircraft, originating static and dynamic responses to counteract them [7].

An aircraft is considered statically stable in the pitch axis if the pitching moment coefficient decreases with the increasing angle of attack, satisfying the condition in Equation 2.16:

$$C_{m_\alpha} < 0 \tag{2.16}$$

This means that if a disturbance causes an increase in the angle of attack, the aircraft generates a negative pitching moment, which makes it return to its initial flight position. Similarly, if a disturbance reduces the angle of attack, the aircraft generates a positive pitching moment. Figure 2.21 presents examples of different types of longitudinal static stability.

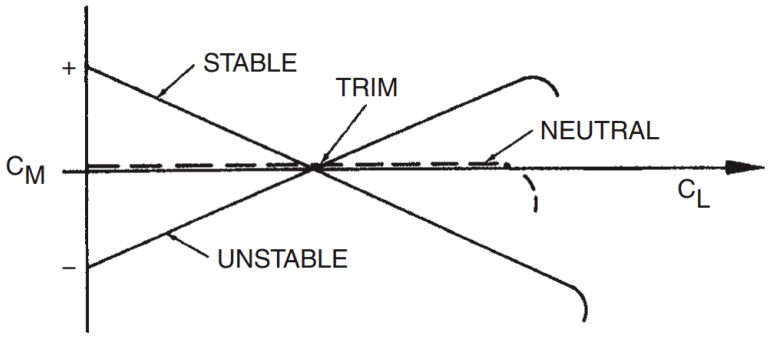

Figure 2.21: Stable, unstable and neutral longitudinal static stability (adapted) [10].

To have a statically stable aircraft, it is necessary to ensure that the aircraft has a positive static margin (SM). The SM is defined as the distance between the aircraft's CG and its neutral point, divided by the mean aerodynamic chord (MAC), as presented in Equation 2.17. The bigger the distance between those two points, the greater the stability of the aircraft. The SM is considered positive if the CG is ahead of the neutral point, negative if the CG is behind the neutral point, and zero if the CG and neutral point coincide [5].

$$SM = \frac{x_{NP} - x_{CG}}{MAC} \tag{2.17}$$

To be considered dynamically stable in the pitch axis, an aircraft must be able to dampen the oscillations caused by disturbances. These oscillations can be classified into two modes: the short-period mode and the phugoid mode. Both modes are characterised by a damping ratio and a frequency [7].

Short-Period Mode

The short-period mode is characterised by a relatively short period oscillation with a high frequency. This behaviour can be attributed to the fact that this mode is typically highly damped. The oscillation occurs around the center of gravity and primarily causes variations in the angle of attack, while the velocity and altitude of the aircraft remain nearly constant during a disturbance [11]. The short-period mode is presented in Figure 2.22.

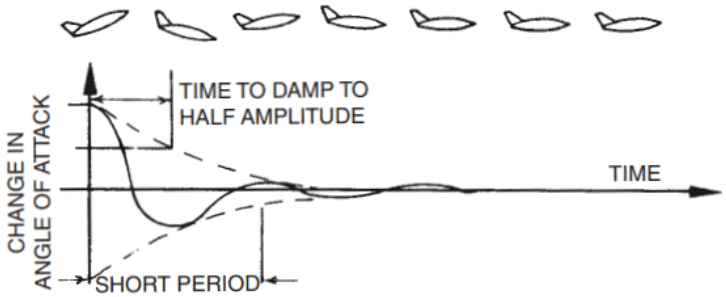

Figure 2.22: Short-period dynamic mode [11].

Phugoid Mode

The phugoid mode is characterised by long-period oscillations which result from a lightly damped low-frequency oscillation. The phugoid oscillation leads to significant fluctuations in the velocity, pitch, and altitude of the aircraft over time, while the angle of attack remains relatively constant [11]. Figure 2.23 depicts the phugoid mode.

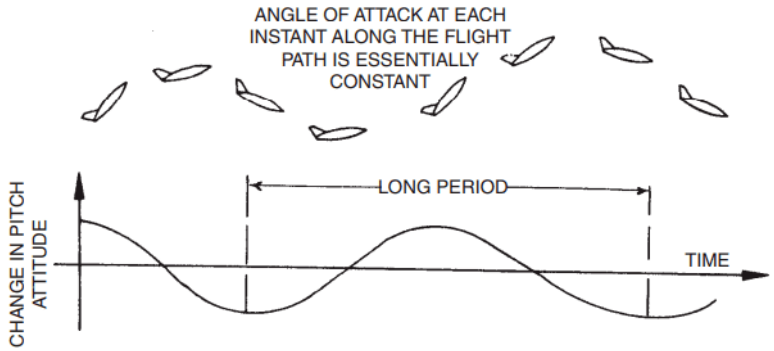

Figure 2.23: Phugoid dynamic mode [11].

2.1.4.4 Lateral-Directional Stability

The lateral-directional stability refers to the aircraft's response to disturbances in the yaw and roll axes. Disturbances in those axes cause the aircraft to move sideways, also known as sideslip, and originate static and dynamic responses to counteract them [7].

An aircraft is considered statically stable in the lateral and vertical axes when the rolling moment coefficient in relation to the sideslip angle (C_{l_β}) is negative and the yawing moment coefficient in relation to the sideslip angle (C_{n_β}) is positive, as shown below:

$$C_{l_\beta} < 0 \tag{2.18}$$

$$C_{n_\beta} > 0 \tag{2.19}$$

This means that, for an aircraft with a positive static lateral-directional stability, a sideslip to the right (positive sideslip angle) will generate a negative moment in the roll axis, causing it to roll to the left and return to the trim position. Simultaneously, it will generate a positive moment around the yaw axis, causing it to yaw to the right, reducing the sideslip angle to zero [5]. Figures 2.24 and 2.25 depict the static directional and lateral stability of a typical aircraft.

To analyse the lateral-directional dynamic stability, it is necessary to account for the interaction between both the rolling and yawing moments. These moments are simultaneously produced during a sideslip and require three lateral-directional modes to recovery: the roll subsidence mode, the spiral mode, and the dutch-roll mode [7].

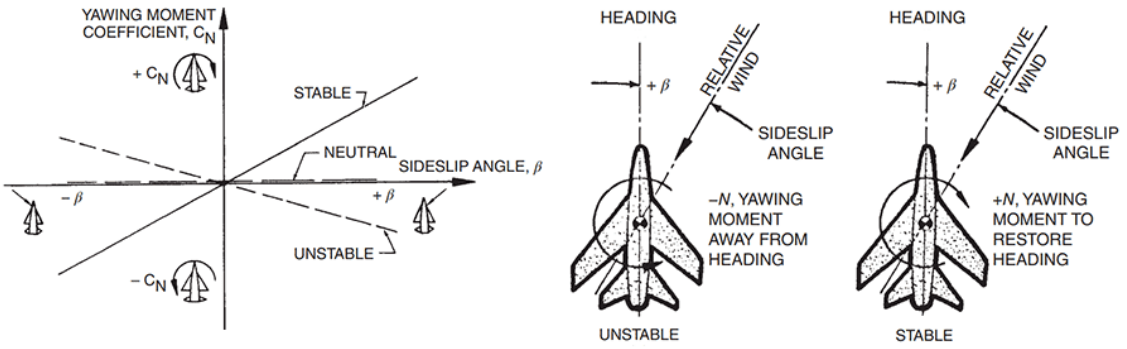

Figure 2.24: Static directional stability [12].

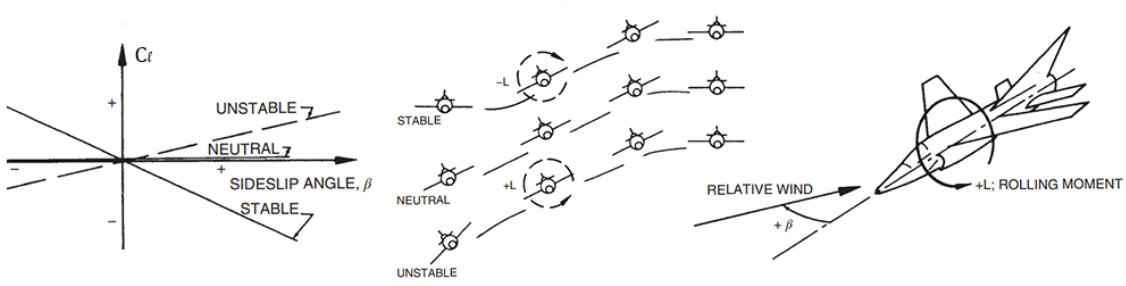

Figure 2.25: Static lateral stability [12].

Roll Subsidence Mode

The roll subsidence mode, also known as the roll mode, is a non-oscillatory lateral characteristic that is exhibited by an aircraft in response to any lateral directional disturbances. This is a heavily damped mode, acting around the roll axis, typically studied independently from the spiral and dutch-roll modes.

The roll subsidence mode is initiated when a disturbance causes the wing to experience a component of velocity perpendicular to it, making the wing uneven. This results in an increase in the incidence on the down-going wing (increasing lift) and a decrease in the incidence of the up-going wing (decreasing lift). The resulting difference in lift generates a restoring rolling moment [11].

Spiral Mode

The spiral mode is characterised by a slow and non-oscillatory behaviour involving complex coupled motion in roll, yaw, and sideslip. This mode is typically initiated by a disturbance that results in a small positive roll angle that, if left uncorrected, results in a small positive sideslip velocity. This sideslip causes the fin to experience a lateral incidence, generating a yawing moment that turns the aircraft into the direction of the sideslip. Consequently, this motion induces differential lift across the wingspan, creating a rolling moment that further increases the roll angle. As a result, the aircraft enters a spiral [11].

Dutch-Roll Mode

The dutch-roll mode is an oscillatory mode in response to lateral-directional disturbances characterised by a damping ratio and a frequency of oscillation. It involves simultaneous roll, yaw, and sideslip motions.

This mode can be initiated by a disturbance in the yaw axis that requires an oscillatory response. As a result, variations in the relative velocity of the air over the wing occur, causing oscillatory perturbations in the differential lift which, in turn, generates a rolling motion. Consequently, the rolling motion disturbs the wing level trim allowing the aircraft to slip sideways, generating an oscillatory sideslipping motion [11].

2.1.5 Control Surfaces

The control of an aircraft is the process of transitioning the flight condition from the initial trim position to a new desired position. This is achieved by manipulating devices referred to as control surfaces [7]. In general, control surfaces can be categorized into conventional and non-conventional, as depicted in 2.26.

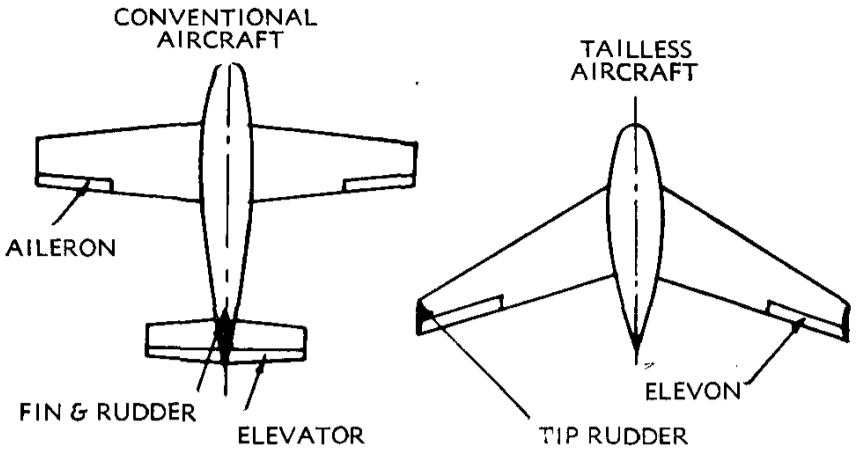

Figure 2.26: Control system for tailless and conventional aircraft [13].

The primary control surfaces of a conventional aircraft are the aileron, the elevator, and the rudder. This surfaces are utilized to control the lateral, longitudinal and directional motions of the aircraft, respectively. In the case of a tailless aircraft, which is a non-conventional aircraft, the primary control surfaces are the elevon and the tip rudders. The elevon combines the design requirements of both aileron and elevator into a single control surface and is responsible for the lateral and longitudinal motions of the aircraft. The tip rudders have the same directional control purpose as a normal rudder but is placed at the tip of the wings since the aircraft has no tail [13].

2.1.5.1 Winglet

The winglet is a vertical surface that extends from the tip of the wing and it is commonly implemented to reduce the induced drag of the wing [26]. However, in certain configurations, the winglet can be utilized as a lifting surface and function as a vertical stabilizer. This enables a tailless design to achieve directional stability and allows for the incorporation of tip rudders, enhancing the directional control of the aircraft. Figure 2.27 shows the geometrical parameters of a conventional winglet.

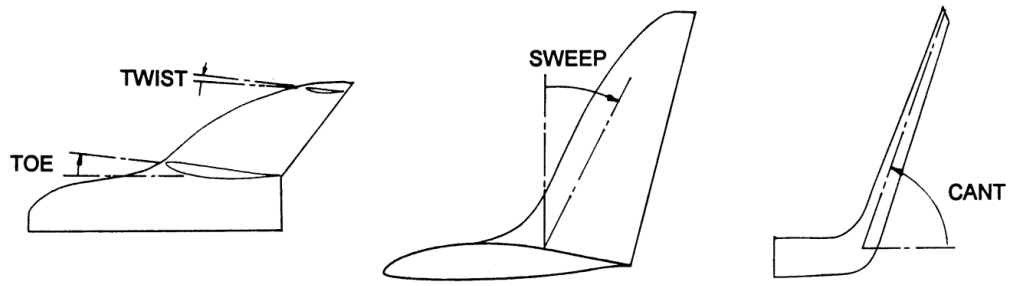

Figure 2.27: Conventional winglet geometrical parameters [14].

2.1.6 Wing Structure and Loads

The wing is arguably the most critical component of an aircraft, as it is responsible for generating the greatest aerodynamic force among all the aircraft components and often incorporates complex mechanical systems which, in turn, will also be exposed to considerable loads. The wing structure is designed to withstand the shear forces and moments produced by lift and drag during flight, incorporating several load-bearing elements that must be meticulously assembled to ensure structural integrity [1]. Figure 2.28 displays an example of a typical wing structure.

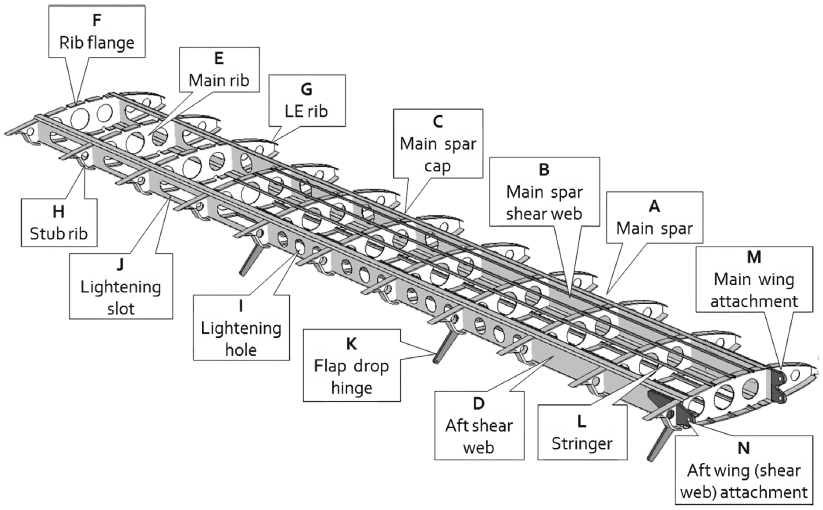

Figure 2.28: Typical structural layout of a wing for general aviation aircraft [1].

Spar

The primary load-carrying element in the wing structure is the main spar, which is designed to counteract wing bending and shear loads. The main spar can have several cross-sectional configurations, but it is typically composed of a relatively slender vertical structure referred to as the main spar shear web, along with two sturdier components known as the main spar caps, which are fastened or bonded to the shear web at the top and bottom edges. The shear web is specifically engineered to withstand a significant portion of the total shear produced by the aerodynamics loads acting on the wing, while the bending moment is counteracted by the spar caps [1].

Ideally, the main spar should be positioned where the bending moments are maximized and the torsional moments are minimized. However, the torsional moments are minimum at the center of pressure, which varies in position depending on the flight condition. Therefore, the main spar is usually placed at the highest thickness point of the airfoil, where its area moment of inertia can be maximized, considering that this point is relatively close to the center of pressure to avoid excessive torsional moments [29]. The secondary spar should be positioned as close as possible to the hinge axis of the control surfaces to minimise their bending and torsion loads, while ensuring that there is enough space to allow for the full range of motion of the surfaces [7].

Stringers

Stringers are slender, elongated components with a relatively small cross-section that are utilized to increase the longitudinal rigidity of skin and prevent it from buckling under load.

Ribs

The ribs are critical structural components that connect to the spars and wing skin. These have several functions, including stabilizing the wing skin, which prevents it from buckling and maintains its intended aerodynamic shape, transferring the wing torsional loads to the spars, and shorten the effective column length of the stringers, increasing their resistance to column buckling. Additionally, they withstand crushing loads caused by wing bending, redistribute concentrated loads (such as those from the landing gear, flap deployment, and engine pylons), and resist diagonal tension loads from the skin in case of skin wrinkling [1].

2.1.6.1 Structural Loads

A well-designed wing structure must be designed to sustain a wide range of different types of loads. Therefore, it is necessary to determine the maximum load that the structure must be capable to withstand to meet the design requirements.

The maximum load that the aircraft is expected to experience during normal operation is

referred to as the limit load. However, to ensure a safety margin, an aircraft structure is always designed to withstand loads that are higher than the limit load. The proof load is the maximum load that an aircraft structure must endure without undergoing permanent deformation. This value is obtained by multiplying the limit load by a proof factor, which can range from 1 to 1.25. The ultimate load is the maximum load that an aircraft structure is designed to sustain without breaking. This value is obtained by multiplying the limit load by an ultimate factor of 1.5 [26].

2.1.6.2 Flight Envelope

The flight envelope, also known as the V-n diagram, displays the specific load factors corresponding to the range of airspeeds in which an aircraft is designed to operate. This diagram helps us understand what the aircraft's structural requirements and limitations are. It also provides valuable information for the pilot, so that he knows how to react depending on the flight circumstance. Typically, to develop a flight envelope, it is necessary to follow some guidelines outlined in aviation regulations specific to the type of aircraft that is being designed. A complete V-n diagram is composed of two separate operating conditions that result in different airframe loadings: the maneuvering loads and the gust loads [1].

2.1.6.3 Maneuvering Loads

The maneuvering loads refer to the forces that the aircraft experiences during normal flight conditions caused by the pilot direct input.

To develop the maneuvering envelope, it is necessary to define the maximum positive and negative load factors of the aircraft. These values can vary depending on the regulation that is being followed, which changes depending on the region that the aircraft is going to operate. Then, the positive and negative stall curves are calculated using Equation 2.20, where V_S is the stall speed. These curves define the limit loads beyond which the aircraft will enter in stall.

$$L = nW_{TO} = \frac{1}{2}\rho V_s^2 S C_{L_{max}} \tag{2.20}$$

The airspeeds at which the stall curves intersect with the maximum positive and negative load factors are known as the positive maneuvering speed (V_A) and negative maneuvering speed (V_F), respectively. These represent the speed below which the aircraft is capable of resisting the loads generated from the full deflection of the control surfaces. Lastly, the diving speed (V_D) needs to be defined. This speed represents the maximum airspeed that the aircraft's airframe is designed to withstand and is another parameter that varies depending on the regulations [1]. Figure 2.29 illustrates a typical maneuvering envelope.

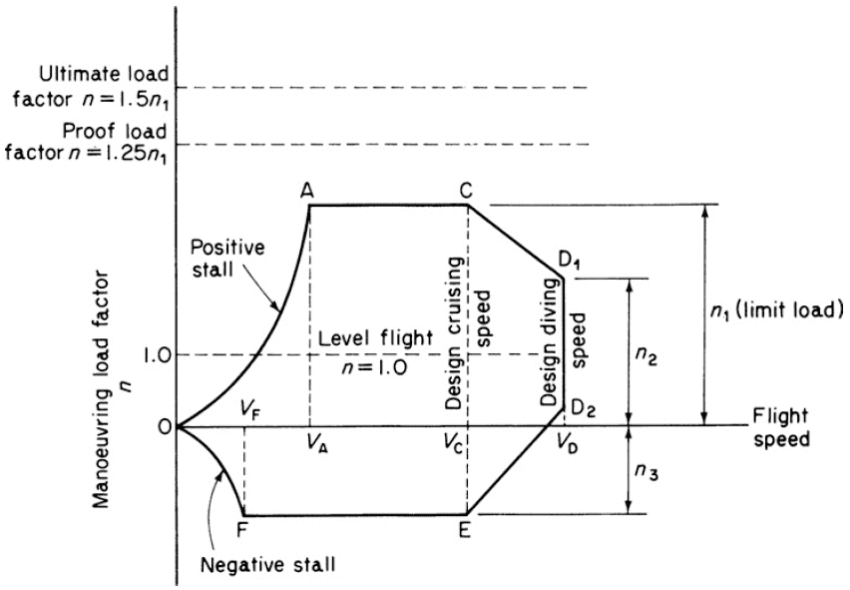

Figure 2.29: Typical maneuvering envelope [15].

2.1.6.4 Gust Loads

A gust can be described as a vertical disturbance in the airflow during flight caused by atmospheric conditions. This phenomenon is commonly known as turbulence. Gusts alter the angle of incidence of the wing, resulting in an increase or decrease in the lift of the wing, which can subject the aircraft to higher loads than those experienced during maneuvering. Therefore, it is important to consider these loads when designing the structure of the aircraft to prevent failure [1] .

Although gusts can be classified as sharp-edged and graded gusts, the first being an instantaneous disturbance and the second being a gradual growth disturbance, the response of the aircraft and the change in angle of attack occurs gradually over a specific period of time. As a result, to calculate the gust loads, its necessary to account for this gradual impact of the gusts on the aircraft, which is referred to as “alleviation” [1].

The gust factor is given by Equation 2.21, where C_{L_α} is the wing subsonic lift coefficient curve slope, K is the gust alleviation factor and u is the vertical gust velocity.

$$n = 1 \pm \frac{\frac{1}{2}\rho V C_{L_\alpha} K u}{W/S} \tag{2.21}$$

The gust alleviation for subsonic flight is calculated in Equation 2.22, using the mass ratio (μ_{mr}).

$$K = \frac{0.88\mu_{mr}}{5.3 + \mu_{mr}} \tag{2.22}$$

The mass ratio is then calculated using the Equation 2.23, where g is the acceleration due to

gravity and $\bar{c}$ is the mean geometric chord.

$$\mu = \frac{2(W/S)}{\rho g \bar{c} C_{L_\alpha}} \tag{2.23}$$

The subsonic lift coefficient curve slope is calculated using the Equation 2.24, where β_M is the mach number parameter (Prandtl-Glauert), k is the ratio of two-dimensional lift curve slope to 2π and $\Lambda_{c/2}$ is the sweep at the mid chord.

$$C_{L_\alpha} = \frac{2\pi A}{2 + \sqrt{\left(\frac{A\beta_M}{k}\right)^2 \left(1 + \frac{tan^2 \Lambda_{c/2}}{\beta_M^2}\right) + 4}} \tag{2.24}$$

All equations presented in this section are derived from [1].

Figure 2.30 shows a typical gust envelope, where U_1, U_2 and U_3 correspond to the high, medium and low velocity gusts, respectively. These values are determined according to the regulation in use.

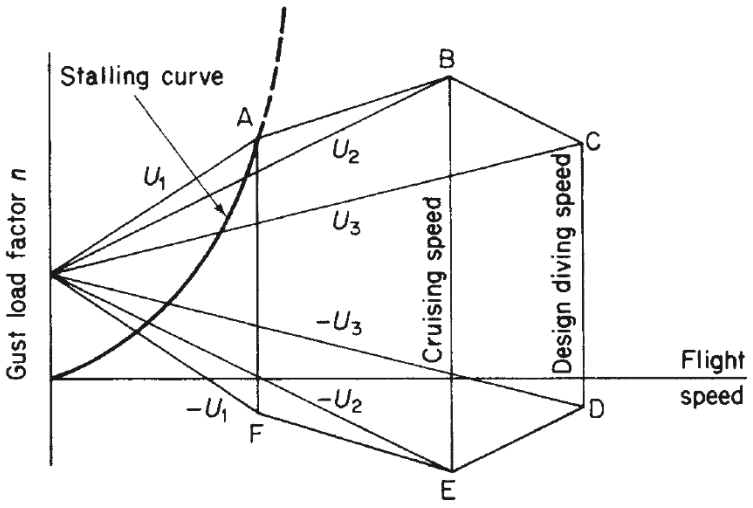

Figure 2.30: Typical gust envelope [15].

2.1.7 Composite Materials

Composite materials are materials formed by combining two or more materials on a macroscopic scale, with the intent of achieving mechanical performance and properties that surpass those of the individual constituent materials. Typically, composites consist of a reinforcement material, often in the form of fibers, and a continuous material called matrix that serves to distribute and transmit the load to the fibers [18]. An example of the composition of composite materials is illustrated in figure 2.31.

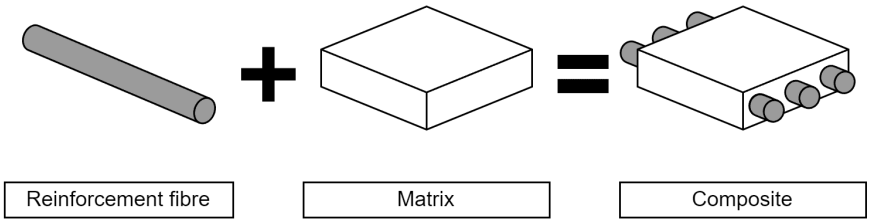

Figure 2.31: Composition of composite material.

2.1.7.1 Classification of Composite Materials

Composite materials composed of two distinct materials are categorized into three main groups depending on the type, geometry, and orientation of the reinforcement fibers, as depicted in Figure 2.32.

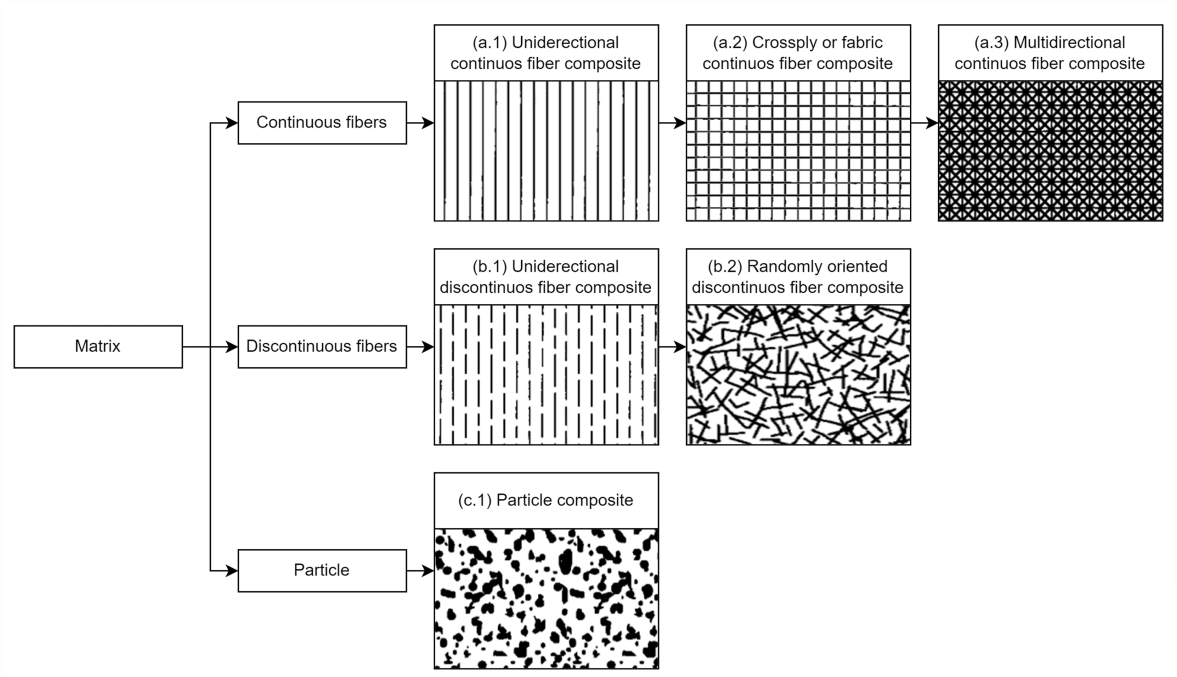

Figure 2.32: Classification of composite material systems (adapted) [16].

Particulate composites (c.1) consist of macro-sized particles of one material randomly dispersed in a matrix of another material. Discontinuous or short-fiber composites consist of short fibers as the reinforcing material oriented along one direction (b.1) or randomly dispersed (b.2) in a matrix of another material. Continuous-fiber composites are reinforced by long, continuous fibers that can be aligned in a single orientation (a.1), perpendicular to one another (a.2) or along multiple directions (a.3) [16].

These materials can be further categorized as isotropic, anisotropic or orthotropic depending on their directional characteristics. A material is considered isotropic if it possesses uniform properties in all directions and is independent of the orientation of the reference axes. It is classified as anisotropic if its properties are different in all directions. And it is considered

orthotropic if its properties are different in three mutually perpendicular planes [17]. Figure 2.33 illustrates the behaviour of these materials when subjected to an axial tension.

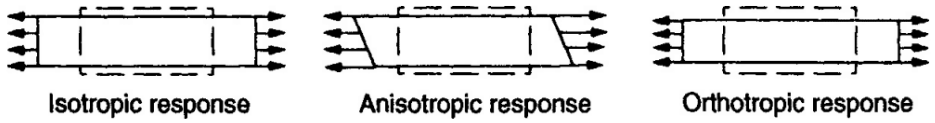

Figure 2.33: Isotropic, anisotropic, and orthotropic materials subjected to axial tension [17].

2.1.7.2 Lamina and Laminates

A lamina, also known as a ply, is a flat or curved sheet composed of, for example, unidirectional or woven (bidirectional) fibers embedded in a matrix material. It is typically considered orthotropic, and its thickness depends on the material used. For analysis purposes, a lamina is often represented with a single layer of fibers throughout its thickness [17].

A laminate is formed by stacking multiple layers of lamina together at specific orientations (θ) to achieve the desired stiffness and thickness, as depicted in Figure 2.34. The layers are bonded together through a curing procedure that varies based on the materials used. The mechanical behaviour of the laminate is influenced by the properties of each lamina and the specific order in which they are stacked [17].

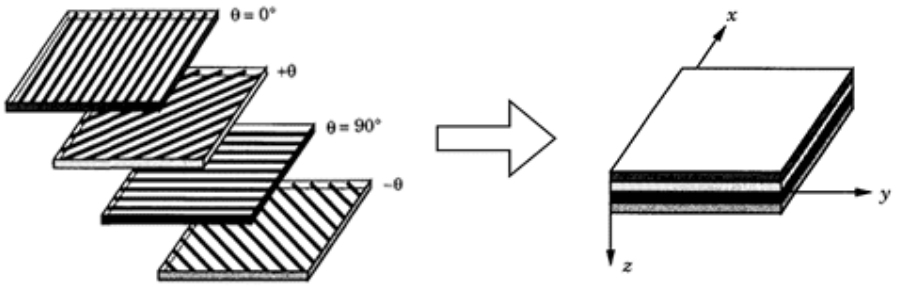

Figure 2.34: A laminate made up of several lamina with different fiber orientations (adapted) [18].

2.1.7.3 Composite Design Rules

To define the stacking sequences of laminates, certain design guidelines are considered. These guidelines aim to create laminates that are less susceptible to high stress concentrations and undesired mechanical coupling effects. According to [30], there are seven rules that should be followed:

1. Symmetry. Whenever possible, stacking sequences should be symmetric about the mid-plane to avoid bending-extension coupling.
2. Balance. Whenever possible, stacking sequences should be balanced, with the same number of $+\theta$ and $-\theta$ plies to eliminate shear-extension coupling.

3. Minimum percentage. There should be a minimum of plies oriented in each direction to minimise matrix degradation.

4. Damage tolerance. External plies should be oriented away from the main load path. Commonly, layers oriented at $\pm 45°$ are placed in the outermost part of the laminate, which increases the buckling resistance.

5. Contiguity. Stacking multiple plies of the same orientation together should be avoided. This minimises interlaminar stresses and ensures a homogeneous stress distribution.

6. Grouping. Layers with $+\theta$ and $-\theta$ orientations can be grouped to reduce bending-twist coupling.

7. Disorientation. The difference in fibre orientation between two adjacent layers should not exceed $45°$ to minimise inter-laminar shear effects.

2.1.7.4 Sandwich Structures

Sandwich structures are highly regarded in the aircraft industry due to their lightweight and high-performance characteristics.

A sandwich panel consist of two thin skins, or facings, of materials with strong mechanical properties bonded to a thicker, lightweight core with low-stiffness. The skins are usually made out of composite laminates and metals, while the cores can be composed of metallic or non-metallic honeycombs, foams, balsa wood, or trusses [16]. Figure 2.35 shows an example of a sandwich structure.

Figure 2.35: Sandwich structure.

The primary function of the skins in sandwich structures is to resist the majority of the bending and in-plane loads, while the core provides stability to prevent the skins from buckling. Additionally, the core increases the distance between the skins which increases the area moment of inertia, resulting in an improvement of the flexural stiffness, out-of-plane shear, and compressive behaviour of the structure [16].

2.2 State of the art / VTOL UAVs

Unmanned aerial vehicles (UAVs), commonly referred to as drones, are aircraft that can be controlled without a pilot on board. These vehicles can be operated remotely or autonomously and can be equipped with various payloads such as cameras, sensors, and com-

munication devices depending on the mission characteristics. Originally designed for military purposes, UAVs are also used in civilian applications such as surveillance, tracking, monitoring, aerial photography, and product delivery [31]. These UAVs are mainly classified into two types, each with its own advantages and drawbacks:

- Fixed-wing UAVs: These UAVs are more suitable when high cruising speed and altitude, high flight efficiency, and a large payload capacity are required. This means that these UAVs are capable of performing many tasks that require the vehicle to carry a heavy payload or achieve long endurance and range. However, their usage can be limited due to the need for a runway or catapult to facilitate takeoff and landing [31].
- Rotary-wing UAVs: These UAVs can takeoff and land vertically, hover, and fly in any direction. This versatility makes them suitable for a wide variety of applications and environments. However, these present low flight efficiency, which limits their ability to perform long range missions [31].

Hybrid vertical takeoff and landing (VTOL) UAVs combine the concepts of fixed-wing and rotary-wing UAVs in a single platform. This configuration has gained significant attention in recent years due to its ability to inherit the advantages and overcome the limitations of traditional fixed-wing and rotary-wing UAVs [32].

2.2.1 VTOL History

According to belief, the beginning of VTOL history can be traced back to Leonardo da Vinci's sketches, with his design of an "aerial screw" in the late 15th century [33]. However, he only made small models and did not seriously explore vertical flight, so the development of the first unmanned helicopter only appeared in 1877 by Italian inventor Enrico Forlanini.

Later, around 1900, many individuals started experimenting with helicopters, but it was French inventor Paul Cornu who achieved the first manned, untethered VTOL flight with his "Cornu Helicopter" in 1907. His flying machine lifted him into the air, untethered, at a height of one foot for twenty seconds. While his subsequent flights achieved greater heights, the Cornu Helicopter proved to be unreliable and unstable, and the project was abandoned. Fourteen years later, the autogyro was invented by Juan de la Cierva and was more stable than helicopters but not a true VTOL aircraft as it required forward movement or a high wind speed to achieve lift [34].

It was not until the late 1930s, after many attempts were made worldwide on helicopters, often with disastrous and lethal results, that helicopters began to become widely available when the German Focke-Wulf Fw 61 was built and in the 1940s, Igor Sikorsky, a Russian-born inventor, collaborated on the design of the R-4, which became the first helicopter to be mass-produced [34].

Then, in the 1950s, the emergence of turbine engines as a popular technology led to the development of the Harrier Jump Jet, known to be the first and most successful VTOL aircraft

in aviation history. Subsequently, the Bell Boeing V-22 Osprey was developed and is considered to be the world's first successful tilt-rotor aircraft. It was from here that aircraft began to look like we know them today and where the basis for most of today's VTOL aircraft is taken from [35].

In 1956, the US Army began investigating "flying jeeps," which would be smaller and easier to fly than helicopters. Several prototypes were developed but research was eventually abandoned after the Army deemed the concept unsuitable for modern battlefields. Other early VTOL projects from the Army included the Hiller VZ-1 Pawnee, a direct-lift rotor aircraft and Bell Rocket Belt, a single-person "jet pack." While these projects were ultimately unsuccessful they paved way for future development of personal VTOL aircraft [34].

Nowadays numerous companies are working on developing and innovating VTOL aircrafts. Some notable examples include Joby Aviation's aircraft with their "electric aerial ridesharing" concept which has been under development since 2009 and is a fixed-wing tilt-rotor VTOL capable of carrying five people with a max range of 240 kilometers [36]. Another great example is EHang AAV an electric passenger-grade autonomous aerial vehicle capable of transporting two people with flights always connected to a network allowing communication with command-and-control center enabling remote control of aircraft and transmission of flight data in real time [37].

2.2.2 VTOL UAV Technologies

There are several different UAV VTOL technologies available, including [38]:

1. **Tail-sitter:** A tail-sitter VTOL is a type of aircraft designed to takeoff and land vertically on its tail. After takeoff, once the desired altitude is reached, the system tilts forward to transition the aircraft to horizontal flight mode.

2. **Tilt-rotor:** A tilt-rotor aircraft is equipped with multiple rotors mounted on tilting shafts or nacelles. During the transition from hover to cruise flight, some or all of the rotors tilt forward in the direction of flight to provide the necessary forward speed until the aircraft achieves its desired cruise flight. This design enables the aircraft to take off and land vertically like a helicopter, but also fly forward at high speeds like a fixed-wing aircraft. However, it presents some challenges, such as the need for complex control systems to manage the tilt of the rotors.

3. **Tilt-wing:** The tilt-wing is a type of aircraft design that involves tilting a portion or the entire wing, along with the rotors, during the transition between flight modes. This design has the same takeoff and landing advantages as the tilt-rotor, but also shares its control disadvantages. However, it presents additional challenges, particularly in terms of mechanical complexity and maintenance.

4. **Rotor-Wing:** The rotor-wing or stop-rotor combines the capabilities of a rotary-wing and a fixed-wing aircraft. It uses a rotary wing that spins to create the necessary thrust

to lift the aircraft during vertical flight, such as takeoff and landing, and then stops spinning to act like a fixed-wing during cruise flight.

5. **Dual System:** A dual-system VTOL UAV operates with two separate propulsion systems designed for hovering and level flight. The UAV lifts off vertically using lifting rotors, similar to a multirotor. After reaching a specific altitude, it transitions to level flight by activating the horizontal motor to establish forward momentum. Once the cruise speed is achieved, the vertical lifting rotors are deactivated, and the UAV operates similarly to a conventional fixed-wing UAV. This separation of the propulsive systems for hovering and level flight allows for the optimisation of each flight mode independently. Compared to other configurations, this has a simpler mechanical design and improved reliability, since it does not require a tilting mechanism. However, the fixed vertical lift rotors create additional aerodynamic drag during flight, which impacts the UAV's performance.

Figure 2.36 presents an example of each of the mentioned UAV VTOL technologies.

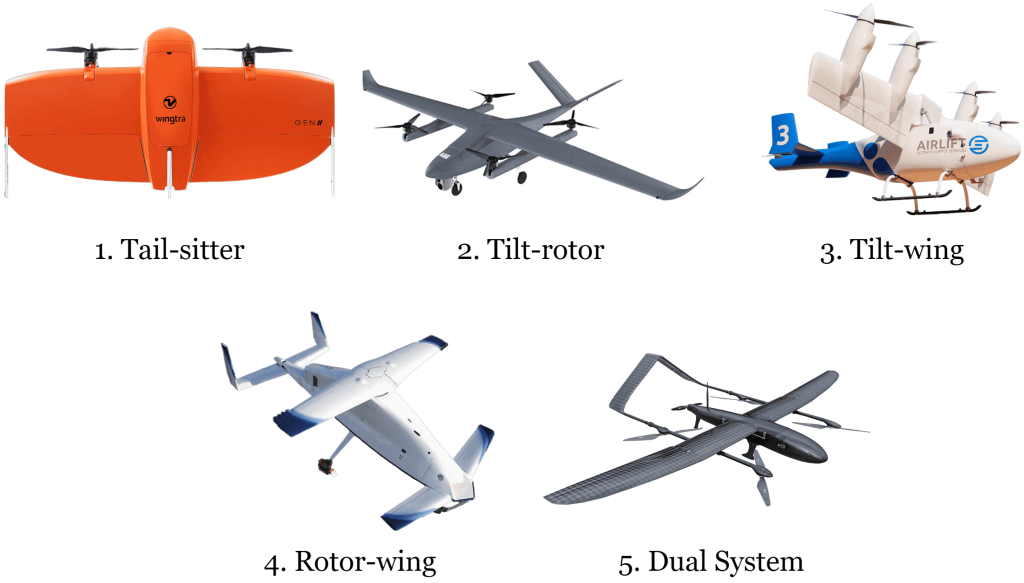

1. Tail-sitter 2. Tilt-rotor 3. Tilt-wing

4. Rotor-wing 5. Dual System

Figure 2.36: Tail-sitter [19], Tilt-rotor [20], Tilt-wing [21], Rotor-wing [22] and Dual system [23] technologies.

2.2.3 VTOL UAV's Market and Applications

According to market research reports, the global VTOL UAV market is expected to grow significantly in the next decade. There is some discrepancy regarding its market valuation, with estimates ranging from 842 million to 6.4 billion in the year 2022, and a projected range of 4.627 billion to 27.5 billion by the year 2030. However, what remains consistent is the expected compound annual growth rate of around twenty percent over the next eight-year period [39].

This expected rise in demand can be attributed to increasing investments in the development of UAV technologies, which have enabled continuous advances in military and defense

applications. These advancements have resulted in reduced material costs and the miniaturization of components, facilitating the development of new and advanced UAVs capable of repeated long flights and equipped with advanced flight control systems. These UAVs are being used in missions, border patrols, and counter-terrorism activities [40].

Another reason for the rising market is the growing use of UAVs in civil and commercial applications. These are used for a wide range of solutions, including security surveillance, emergency response, search and rescue, communications and broadcast facilitation, small package and bulk cargo transport, visual, spectral, and thermal examination of structures, monitoring of linear network infrastructure, photography and cartographic survey, agricultural fertilizer and chemical application, aircraft external maintenance inspection, and atmospheric research [41].

Table 2.1 showcases multiple VTOL UAVs available on the market, along with their respective characteristics.

Table 2.1: Criteria importance and performance of each UAV configuration.

Aircraft	Mass [kg]	Wingspan [m]	Payload [kg]	Speed [m/s]	Endurance [min]
ALTI Transition	5.6	3	1	20	660
Aero 2	208	6.1	40	42	180
Baby shark 260	13	2.5	2.1	30	150
Bat UAS	95	3.6	34	46	580
DeltaQuad Pro	6.2	2.3	1.2	28	120
FDG30 Mako Shark	6	3	1.5	30	360
FDG410	34	4.1	10	25	210
FDG50F	55	4.8	10	26	600
FDVF15	15	2.6	3.5	28	150
FlyDragon FLY-380	50	3.8	15	33	120
HeadHunter	14	3.5	1.5	42	120
P330 PRO	14	2.5	2	21	160
PteroDynamics X-P4	38	4	7	31	60
SatLab SLA-2	6.8	2.4	1	22	75
Skywalker	2.5	2.1	0.5	19	25
Supercam SX350	13.5	3.2	0	33	120
Tilt-rotor Drone G10	33	3.3	5	20	120
Aerospace Goshawk	5	1.8	1	19	150
WingtraOne Gen II	3.7	1.25	0.8	16	59

2.3 Tools

2.3.1 Flow5

Flow5 is a closed-source, user-friendly design and analysis tool for planes and sails that operate at low Reynolds numbers [42]. This program incorporates the functionalities of XFLR5 [43] and sail7 but excludes the capabilities of XFoil [44]. It allows for the analysis of 3D flow using the existing methods of XFLR5 such as the Lifting Line Theory, the two Vortex Lattice Methods, and the volume quad panel method, as well as two more new triangular panel

methods. Despite XFoil not being directly integrated into flow5, the program still allows for 2D direct and inverse airfoil analysis by utilizing XFLR5 as an external back-end to generate the 2D viscous data. In comparison with XFLR5, Flow5 offers a range of new features such as a revamped graphical user interface, an integration with external CAD software enabling the import of fuselage geometries in STEP format, an integration with Intel's MKL library and multi-threading, which results in reduced analysis times. The coupling of these new features with the new analysis methods further improves the accuracy of the obtained results.

2.3.2 Prop Selector

PropSelector is a software program developed by Brian R. Gyles that is used for the selection of propellers. It calculates the performance of propellers, with different numbers of blades, based on its pitch and diameter, relative wind speed, altitude, and engine rotation speed. The program provides information on the traction available, shaft power, power available, and propeller efficiency. The software is based on relationships identified from NACA propeller data described by E.P. Lesley in National Advisory Committee for Aeronautics Technical Note 698 [45].

2.3.3 SolidWorks

SolidWorks is a modeling CAD and computer-aided engineering (CAE) software. It allows for the creation of 2D drawings and 3D models of complex parts and assemblies making it a goof alternative for design and building of mechanical, electrical, and software elements. This software offers a range of powerful and intuitive tools such as CircuitWorks, which is an electronic CAD/ECAD translator that enables engineers to create accurate 3D models of circuit boards, Electrical 3D, which enables users to place electrical components and use SolidWorks routing technology to automatically interconnect electrical design elements, Simulation, which uses finite element analysis to predict a product's real-world physical behaviour by virtually testing CAD models, and Visualize, which allows users to create photo-quality content quickly and easily.

2.3.4 Ansys

Ansys offers a comprehensive suite of software that spans the entire range of physics, providing access to virtually any field of engineering simulation required for a design process. For this project, the most important features of the Ansys software are Ansys Mechanical, which is a FEA tool that offers a dynamic environment with a complete range of analysis tools, and Ansys ACP Pre & Post, which focuses on the design and analysis of layered composites. These tools enable users to prepare geometries for structural analysis, incorporate additional physics, and utilize advanced solver options.

Chapter 3

Conceptual Design

This chapter outlines the process of designing the initial concepts for a wing and its integration with the Casta's platform. The objective of the conceptual design is to consider the project's requirements and constraints, evaluate all feasible configurations, and narrow down the options for the design of the wing. Additionally, it includes some considerations regarding the positioning of specific components and details about the structure of the wing.

3.1 Design Process

The process implemented to design a concept for any aircraft component varies depending on the specific component and the system in which it will be incorporated. In this project, the design and placement of the wing takes into account the usual flight performance requirements, as well as additional restrictions imposed by the platform of the multirotor. Figure 3.1 presents the process adopted to develop the concept of the wing.

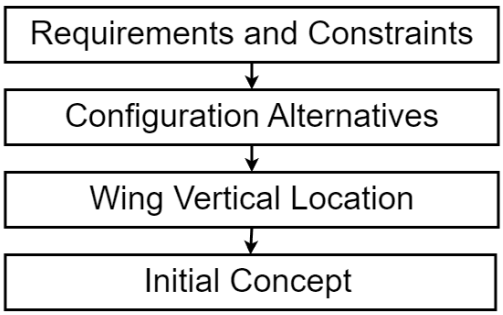

Figure 3.1: Design process of a wing for integration with a multirotor UAV.

3.2 Requirements and Constraints

The development of the wing's design is restricted by certain requirements specified by the AAM business unit, as well as constraints imposed by the geometry of the UAV's frame.

The UAV with the wing attached must not exceed a maximum takeoff mass (MTOM) of 40 kg, including the payload. It must also be capable of operating and maintaining stable flight both with and without the payload. This allows the UAV to travel to its destination fully loaded and return empty, providing flexibility and versatility for a variety of applications.

The design must be capable of operating at high ground altitudes, with a maximum service ceiling set a 3000 meters above sea level. Additionally, it is crucial to maximize the range of the UAV to increase its travel distance, allowing for extended missions across a wide range of environments. To achieve this, the design should include an advanced forward flight propulsive system (FFPS) to ensure optimal performance at these altitudes.

The structure of the wing must be made of composite materials due to their high strength-to-weight ratio, durability, and ease of production. The overall system must be as simple as possible and, to improve its practicality, the wing should be removable with an easy attachment and detachment mechanism. This preserves the ability to operate in confined or urban environments and allows for easy storage and transportation of the UAV.

Another factor that must be taken into account is the dimensional constraints imposed by the frame of the multirotor and the diameter of its propellers, which are shown in Figure 3.2. It is important to avoid any interference between the wing and the downstream of the propulsion system, which sets some initial constraints on the dimensions of the wing.

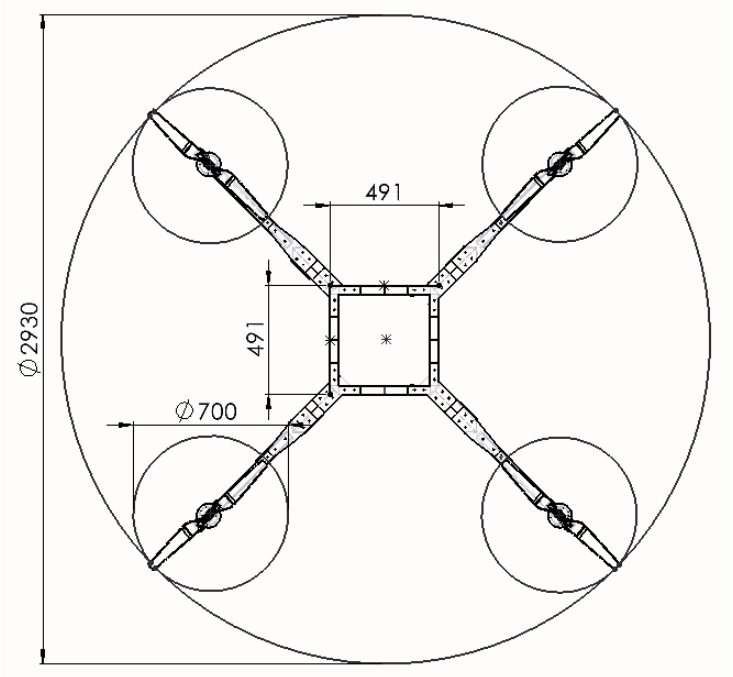

Figure 3.2: Dimensions of the frame and components of the UAV.

3.3 Configuration Alternatives

Given the geometry of the multirotor's frame to which the wing will be attached, the optimal orientation of the frame relative to the flight direction needed to be determined to improve the UAV's aerodynamic performance. Due to the radial symmetry of the frame, there are only two possible orientations to consider, as illustrated in Figure 3.3.

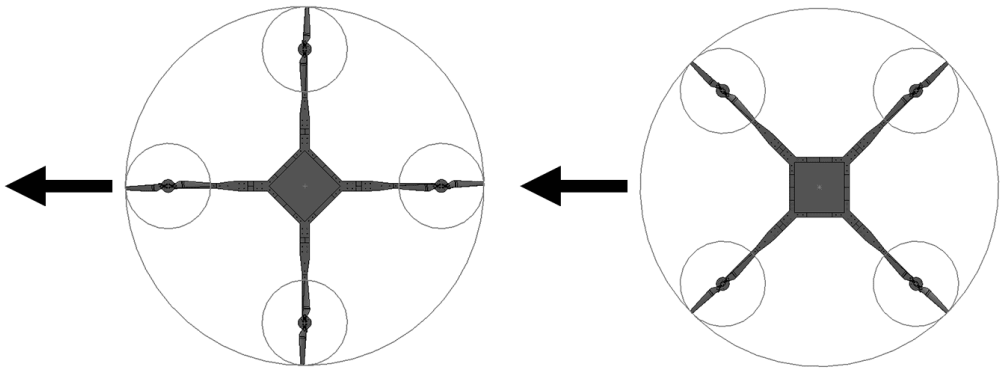

Figure 3.3: Configurations "+" and "×" representative of the frame orientation relative to the flight direction.

To determine the configuration that would provide the best flight conditions, several design concepts were considered for each configuration, with varying wing shapes and sizes. The purpose of these designs was to understand what type of wing would be feasible and what would not. One example for each configuration is shown in Figure 3.4.

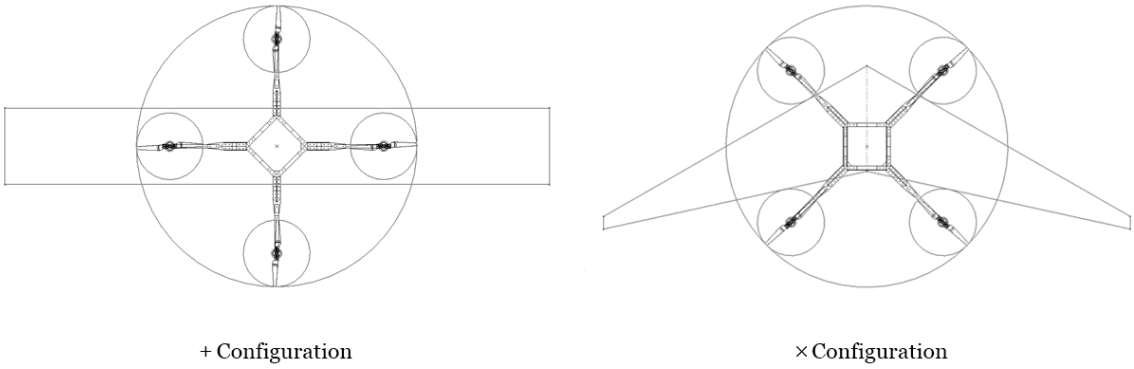

Figure 3.4: Wing shape possibilities of each configuration.

Visualising these possibilities aided in better understanding the major advantages, drawbacks, and limitations of each design. Looking at the "+ configuration", one of the main benefits that seems visually evident is that the structure will generate less drag during flight, especially if it is assumed that the two arms perpendicular to the flight direction are inside the skin of the wing. This characteristic also allows for the possibility of using the frame of the UAV as part of the wing spar, potentially reducing the wing's weight. Additionally, this configuration enables the option of adding an empennage to the design, as one of the arms aligned with the flight direction can serve as a connection point for it.

However, using this configuration would require the wing to be divided into multiple sections and have two openings of significant size to avoid interference with the downstream generated by the propulsion system. These parameters would make the wing structurally complex and restrict its shape by imposing a minimum chord length. This configuration would also require either the empennage, which increases the complexity of the structure,

or a flight control system that uses the vertical propulsive system to achieve stability, which reduces the maximum range and endurance of the UAV. Additionally, implementing a forward flight propulsion system would pose challenges due to the limited available space for its integration.

Regarding the "× configuration", it is possible to create a flying wing shape that operates within the existing constraints. The main advantage of this shape is that it eliminates the need for an empennage and the use of the propulsive system as a stability control, which removes complexity of the structure and the system.

On the downside, the orientation of the frame exposes a significant portion of the wing to turbulent flow and the flying wing design requires a reflex airfoil to maintain longitudinal stability, which results in a wing with reduced aerodynamic efficiency. Moreover,

To compare these configurations more easily and understand which characteristics are most suitable for this case, Table 3.1 presents three configurations with various criteria and corresponding levels of importance (I), ranging from 1 to 10, where 1 indicates a lack of importance and 10 indicates high importance. The scores given to the performance (P) on each criterion also range between 1 and 10, with 1 being very poor and 10 being very good. The "Total" values listed below each column represent the sum of each item's performance criteria multiplied by its corresponding importance score.

Table 3.1: Criteria importance and performance of each UAV configuration.

		+ Config w/ tail		**+ Config w/o tail**		**× Configuration**	
Parameter	***I***	***P***	**Score**	***P***	**Score**	***P***	**Score**
Aerodynamic efficiency	9	10	90	8	72	7	63
Range	10	9	90	5	50	8	80
Overall weight	7	6	42	10	70	8	56
Manufacturing process	6	5	30	7	42	8	48
Manoeuvrability	3	9	27	3	9	4	12
Electric efficiency	9	10	90	6	54	9	81
Structural simplicity	8	5	40	7	56	9	72
Total			409		353		412

Upon analysing the results from Table 3.1, one can conclude that the "× configuration" achieved the best overall result. However, it is worth noting that the "+ configuration with tail" also performed well, losing to the "× configuration by a small margin. This suggests that both configurations are viable options and can effectively be implemented to serve the purpose of the UAV.

Ultimately, the decision was made to choose the "× configuration" since it does not require an empennage. This choice eliminates unnecessary structural complexity, reduces the number of components to be manufactured, and minimizes assembly and disassembly efforts.

3.4 Wing Vertical Location

The vertical location of the wing is an important design parameter that was carefully evaluated. Several options were considered, including low wing, mid wing, high wing, and parasol wing.

The parasol wing configuration was initially considered because the distance between the wing and the propellers could be sufficient to avoid the need for openings in the wings while still maintaining the airflow required for the propulsion. This configuration could also provide easy access to the quadcopter frame and enough space to accommodate the payload on its central platform.

However, this option was ultimately disregarded due to the significant drag and consequent longitudinal instability caused by the underlying frame, which would create serious pitching correction problems for the flying wing and make this configuration completely unfeasible.

Of the remaining three configurations, the mid wing was determined as the most suitable option since it allows for the integration of the frame of the UAV into the wing, reducing the overall air resistance and enabling lift to be generated from the central section of the UAV. In addition to this aerodynamic benefit, this configuration also facilitates the connection between the wing spar and the frame, resulting in a reduction in structural complexity and weight.

3.5 Initial Concept

Based on the chosen configuration and planform, an initial concept of the UAV's appearance was developed to begin aerodynamic analysis and assess its feasibility. The proposed design is essentially a flying wing that wraps around the frame of the multirotor, effectively creating a blended wing VTOL UAV. The conceptual design is presented in Figure 3.5.

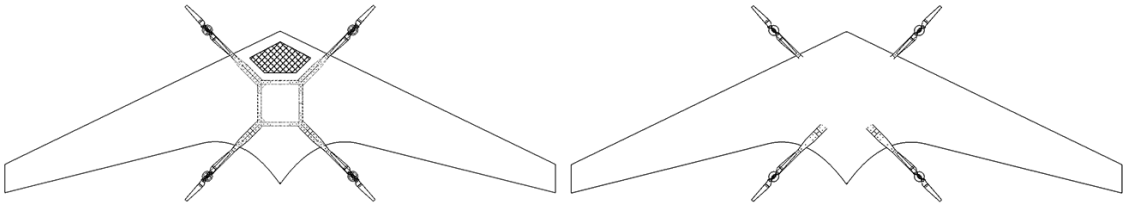

Figure 3.5: Conceptual design of a flying/blended wing for a VTOL UAV.

The design features a swept-back wing that tapers around the circumference of the propellers and has a larger chord length at the root. This provides enough space inside the wing to accommodate the central frame of the UAV, which houses the batteries, and the electrical and avionic systems. Additionally, the extra space in the center of the wing, just in front of the central structure, represented in the figure as the shaded area, is intended for carrying

the payload.

Given the requirement for the wing to be removable, the attachment between the wing and the multirotor should be made by connecting the spars to the lateral beams of the frame. Additionally, given that this configuration does not allow the skin of the wing to be installed in a single piece, the skin is divided into four parts: the left and right wing skins, which are permanently affixed to the ribs and spars, and the top and bottom skin caps, which are attached after the structure of the wing is connected to the frame of the multirotor.

The forward flight propulsive system should be positioned along the center line of the frame to eliminate the need for additional connections through the wing and reduce the weight on its structure. The choice between a pusher or tractor configuration should be made based on the results of the weight distribution and stability analyses.

Chapter 4

Design Methodology

This chapter outlines the iterative process involved in the preliminary design of a flying wing with specific characteristics. It focuses on sizing the wing and its main structural components, considering the weight of the components, the constraints imposed by the frame of the multirotor, the stability requirements, the aerodynamic and gust loads, the manufacturing process and the available composite materials. It also covers the topics of performance and propulsive system selection. The design process of the wing can be represented by a sequential diagram, as shown in Figure 4.1

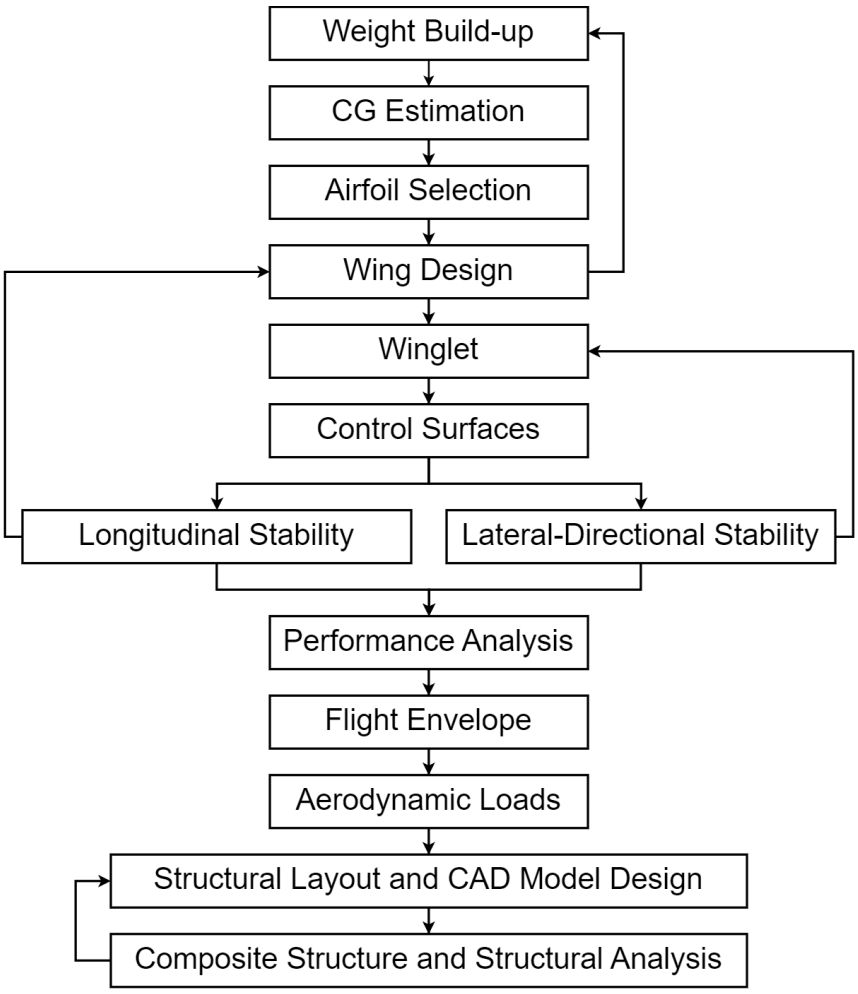

Figure 4.1: Wing aerodynamic and structural design process.

4.1 Weight Build-up

As one of the requirements provided for the UAV is its MTOM of 40 kg, which is equivalent to 392.4 N,there is no need to estimate this value. Similarly, the weights of the frame, electrical systems, vertical propulsive system and batteries did not require any estimation, as they were already established by the AAM business unit.

However, the weight of the remaining components must be carefully estimated to ensure that the maximum takeoff weight is not exceeded. Equation 4.1 presents all the components that are considered to achieve the total weight of the UAV.

$$W_{\text{TO}} = W_{\text{Frame}} + W_{\text{Batteries}} + W_{\text{Systems}} + W_{\text{Wing}} + W_{\text{Payload}} + W_{\text{FFPS}} + W_{\text{Winglet}} \tag{4.1}$$

A description for each component, along with an explanation on how their weight is calculated, is provided below:

- W_{TO}: Refers to the design takeoff weight. Already established.
- W_{Frame}: Is the weight of the frame of the multirotor. Already established.
- $W_{\text{Batteries}}$: Refers to the overall weight of the batteries needed for both vertical takeoff and landing, as well as forward flight. Already established.
- W_{Systems}: Represents the combined weight of the electrical systems, servos and the vertical propulsive system, which consist of four motors and four propellers. Already established.
- W_{FFPS}: Refers to the weight of the forward flight propulsive system, which includes the weight of the motor, propeller and shaft. This weight is determined after evaluating the thrust and power required to ensure that every flight condition is possible and selecting an appropriate motor for the task.
- W_{Wing}: Is the estimate weight of the wing. To estimate the weight of the wing, a composite and sandwich mass prediction model [46] is implemented. This model takes into account the perimeter of the selected airfoil, the wingspan, and its mean geometric chord length. It then estimates the weight of the structure required to withstand a selected load factor.
- W_{Payload}: Is the weight of the payload. It is calculated according to the weight that is available after accounting for all the other components.
- W_{Winglet}: Is the weight of the winglet. It is estimated considering the thickness of the airfoil used on the winglet, its surface area and the density of the material chosen for it.

4.2 Center of Gravity Estimation

In a flying wing, the location of the center of gravity is particularly critical as it drastically impacts the stability of the aircraft, and any significant changes in weight distribution will require adjustments to the geometry of the wing.

Once the weight of all the components is determined, the CG can be calculated using the inertia function of Flow5, which uses a method similar to Equation 4.2. This function automatically calculates the CG of the designed wing (or any model that is imported into the software) and allows for the placement of point masses at any specified location.

$$CG_{(x,y,z)} = \left(\frac{\sum_{i=1}^{n} W_i x_i}{W_{TO}} , \frac{\sum_{i=1}^{n} W_i y_i}{W_{TO}} , \frac{\sum_{i=1}^{n} W_i z_i}{W_{TO}} \right) \tag{4.2}$$

By importing a 3D model of the frame of the multirotor, it is possible to position this structure inside the wing to get a better understanding of the correct disposition of the masses. This way, the masses of the frame, motors, batteries and systems can be precisely positioned, leaving only the location of the additional motor and payload to be defined.

4.3 Airfoil Selection

The first step of the airfoil selection process involves conducting a literature review on low Reynolds number reflex airfoils, which are commonly used in flying wing configurations due to their self-stabilizing properties along the pitching axis. Based on relevant articles, twelve airfoils are selected for analysis and comparative evaluation. The selected airfoils are listed in Table 4.1.

Table 4.1: Considered airfoil selection.

Airfoil	Designer	Plot
E186	Richard Eppler	
E334	Richard Eppler	
FX 69H083	Bell/Wortmann	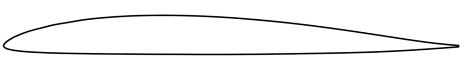
HS132	Hartmut Siegmann	

Continued on next page

Table 4.1: Considered airfoil selection. (Continued)

Airfoil	Designer	Plot
HS522	Hartmut Siegmann	
MH60	Martin Hepperle	
NACA 24112	NACA	
NACA M6	NACA/Munk	
Prandtl-D root	NASA	
PW51	Peter Wick	
S5010	Michael Selig	
S5020	Michael Selig	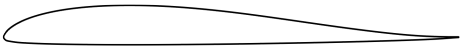

The thickness ratio of these airfoils is subsequently adjusted to ensure sufficient space inside the wing to accommodate the frame of the quadcopter and all of its components. This thickness ratio remains constant from the root to the tip of the wing.

4.3.1 Simulation Parameters

To compare the performance and characteristics of each airfoil, the XFOIL formulation for two-dimensional analysis of airfoils is utilized. The results are obtained through the Multi-threaded Batch Analysis method of XFLR5, which enabled the simultaneous analysis of multiple airfoils within the desired range of Reynolds numbers. Additionally, all the airfoils are globally refined to 200 coordinate points to improve the accuracy of the results.

This analysis is conducted for an angle of attack varying between $-10°$ to $+20°$, with a step size of $0.25°$. Furthermore, the forced transition setting is set to 1 on the top and bottom surfaces. These simulations are also conducted with the forced transition setting is set to 0.3 on both surfaces to have a reference of the airfoil's performance in the case of having a poor wing surface finish, which can lead to early flow separation.

4.3.2 Reynolds Number

To determine the range of Reynolds number within which the aircraft will operate, Equation 2.4 is utilized. The air density and dynamic viscosity are determined according to the U.S. standard atmospheric model [47] for the altitude of the maximum defined service ceiling. For the chord, an estimation of the mean aerodynamic chord of the wing is considered for the analyses. Finally, to optimise performance across various flight conditions, three different speeds are selected. These speeds correspond to the stall, cruise, and maximum speeds at which the UAV is designed to operate.

4.3.3 Proposed Methodology for Airfoil Selection

The methodology used for the selection of the airfoil is based on references [48] and [6], which adopt two different approaches to the problem. Both references are based on analytical methodologies found in the literature related to aviation and airfoil selection.

Instead of assigning arbitrary weights to each characteristic, to reach the conclusion on the most suitable airfoil for the project, Equation 4.5 is utilized to compare the performance (P) of the airfoils against each other. Within this approach, each parameter is evaluated relative to the performance of the best airfoil in that specific parameter, so all parameters are considered to be of equal importance.

For parameters where larger values are desired, the value obtained from each airfoil is divided by the largest value among them, represented in the equation as a component of vector $\boldsymbol{M}$. Conversely, for parameters where a smaller value is preferred, the smallest value obtained from all the airfoils, represented in the equation as a component of vector $\boldsymbol{m}$, is divided by the value of each individual airfoil. Vectors 4.3 and 4.4 contain the maximum and minimum values, respectively, that have been obtained from all the airfoils for each parameter.

$$\boldsymbol{M} = \left[(C_l/C_d)_{max} \; ; \; (C_l^{3/2}/C_d)_{max} \; ; \; C_{l_{max}} \; ; \; \alpha_s \; ; \; BW \; ; \; SQ\right] \tag{4.3}$$

$$\boldsymbol{m} = [C_{d_{min}} \; ; \; C_{m_{mean}}] \tag{4.4}$$

Using this method, the airfoil that performs the best in a specific parameter receives the highest score, that being 1, while the remaining airfoils score less than that.

$$P_1 = \frac{(C_l/C_d)_{max}}{M_1} + \frac{\left(C_l^{3/2}/C_d\right)_{max}}{M_2} + \frac{C_{l_{max}}}{M_3} + \frac{m_1}{C_{d_{min}}} + \frac{\alpha_s}{M_4} + \frac{m_2}{C_{m_{mean}}} + \frac{BW}{M_5} + \frac{SQ}{M_6} \tag{4.5}$$

All these parameters have already been discussed in section 2.1.1. Nonetheless, the following is a simple explanation of their meaning and what is desired from each:

- $C_{l_{max}}$: Is the maximum lift coefficient. Larger values are desirable;
- $C_{d_{min}}$: Is the minimum drag coefficient. Smaller values are desirable;
- $(C_l/C_d)_{max}$: Corresponds to the maximum value of lift-to-drag ratio. Maximizing this parameter also maximizes the range [49]. Larger values are desirable;
- $(C_l^{3/2}/C_d)_{max}$: Corresponds to the maximum value of $C_l^{3/2}/C_d$. Maximizing this parameter also maximizes the endurance [49]. Larger values are desirable;
- α_s: Is the stall angle and corresponds to the angle of attack beyond which the airfoil lift coefficient will start to decrease. Larger values are desirable;
- $C_{m_{mean}}$: Is the average value of the pitching moment coefficients relative to the angle of attack. The design goal is to have a wide range of moment coefficients as close to zero as possible. Smaller absolute values are desirable;
- BW: Represents the bucket width and is the range in which the airfoil operates with high efficiency. This range resulted from the difference between the lift coefficients within an interval of 0.003 from the $C_{d_{min}}$. Larger values are desirable;
- SQ: Represents the stall quality and is a qualitative measurement that evaluates the behaviour of the airfoil after the stall angle is reached. The values are given by initially ranking the behaviour of the airfoils from best to worst, and then categorizing them into groups based on similar performance. This approach is implemented to avoid significant score differences between airfoils with nearly identical stall quality. Larger values are desirable;

Although the aircraft can only be optimised for either maximum range or maximum endurance, both parameters associated to those characteristics are taken into account in the expression. The purpose is to identify which is the optimal airfoil for both requirements. However, given the project's goal to achieve the maximum range, Equation 4.6 is also considered. This equation does not include the parameter associated with the endurance, ensuring that the optimal airfoil for maximum range is not undermined by the introduction of a potentially conflicting parameter.

$$P_2 = \frac{(C_l/C_d)_{max}}{M_1} + \frac{C_{l_{max}}}{M_3} + \frac{m_1}{C_{d_{min}}} + \frac{\alpha_s}{M_4} + \frac{m_2}{C_{m_{mean}}} + \frac{BW}{M_5} + \frac{SQ}{M_6} \tag{4.6}$$

4.4 Wing Design

Given the constraints imposed by the geometry of the multirotor and the lack of a database for similar UAVs to derive typical values from, instead of a typical constraint analysis based on existing aircraft and estimated values, an iterative design process is employed.

4.4.1 Simulation Parameters

The wing surface design analysis is made possible using the Flow5 software, where all the characteristics of the design are defined and analysed. The planform of the wing is composed of three sections: the root, a section aligned with the center of the propellers, and the tip.

For the mesh, the wing is defined with a uniform panel distribution along the span and a cosine distribution in the flight direction. This ensures an even distribution of panels between the selected sections and a denser concentration of panels on the leading edge of the wing. The panel density is chosen to achieve a balance between a coarse and fine mesh while maintaining a proportional number of panels between each section of the wing. This is crucial for obtaining coherent results of distributed loads along the wingspan. Figure 4.2 shows an example of the mesh characteristics.

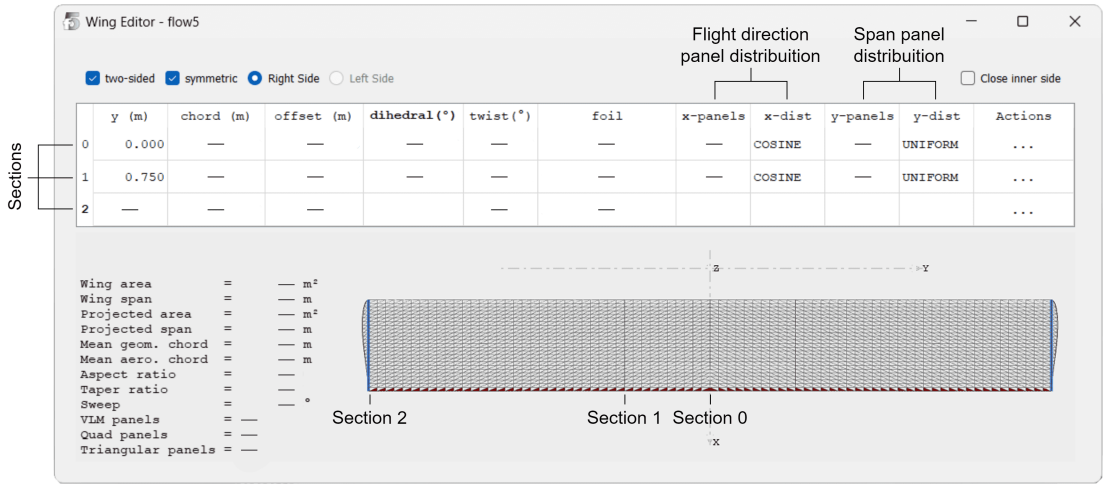

Figure 4.2: Planform sections and mesh characteristics.

The results are obtained through a type 2 “fixed lift” polar analysis, using the uniform density triangular panels method, and considering the air properties at 3000 m of altitude. The polar analysis determines the required speed for the lift to be equal to the weight at each angle of attack within the desired range. The chosen method is based on Galerkin-type triangular formulations and utilizes twice as many panels as the other methods, resulting in slightly better results [50]. Figure 4.3 shows the interface of the software along with the selected parameters for the simulation.

This analysis is conducted for an angle of attack varying between $-10°$ to $+15°$, with a step size of $0.5°$.

4.4.2 Proposed Methodology for Wing Design

For a clearer understanding of the methodology, it is important to note that the wing, similar to the one shown in Figure 4.2, is designed using three sections: the root (first section), the middle section (second section), which is positioned to coincide with the center of the propellers, and the tip (third section).

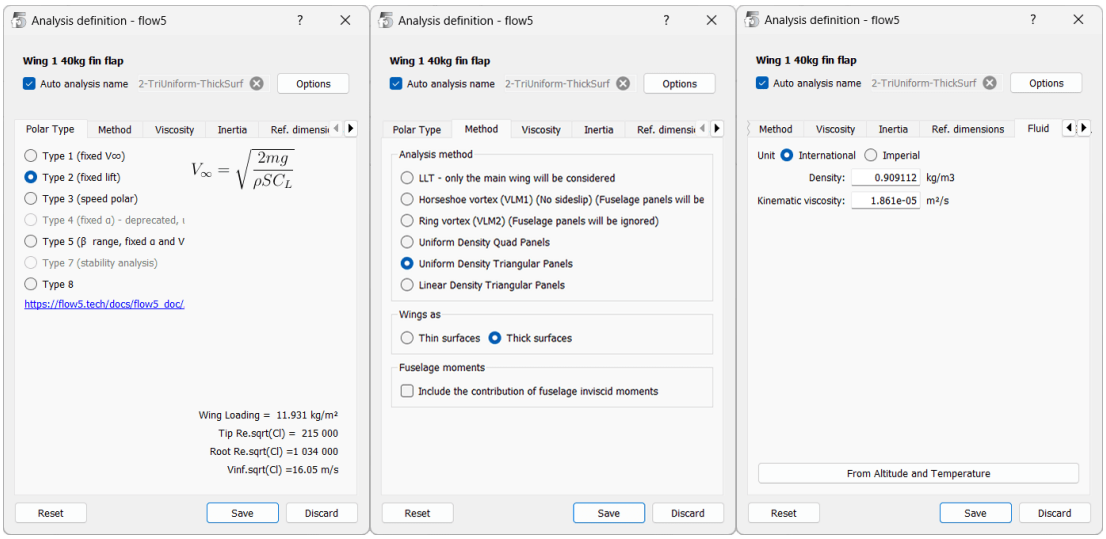

Figure 4.3: Flow5 interface and simulation parameters.

For this particular case, the initial step in the wing design is to determine the root chord length, considering two key factors: the first is that the chord must be sized to ensure that the frame and components of the UAV fit within the limits of the chosen airfoil. The second is that a smaller chord optimises the lift distribution across the wingspan by minimizing the difference in tapering rate between sections. The latter is particularly important considering the constraints imposed on the second section, which result in a considerable variation in chord length between the first and second sections.

Considering these two key factors, the design process also requires the deliberation of other important aspects. For instance, the trailing edge of the second section is defined based on the limits of non-interference with the propellers, while the leading edge and, consequently, the chord length of this section are set considering the sweep angle of the wing.

The sweep angle is incorporated into the design to adjust the aerodynamic center and ensure the longitudinal stability of the aircraft. Due to manufacturing purposes, constant sweep angle is maintained from the root to the tip of the wing.

The tip chord length is established relative to the second section, considering a taper ratio that optimises the lift and load distributions of the wing. This aids in reducing the drag due to lift and excessive bending moments, as explained in section 2.1.2.7.

Using this planform, the wing incidence is set to achieve a zero moment coefficient at zero angle of attack, which will be the cruise condition. The wing twist is then modified to optimise the lift distribution and expand the range of operational angles of attack of the aircraft. These two parameters, together with the swept angle, should be adjusted so that the highest values of C_L/C_D are achieved at the designated cruise condition.

The dihedral of the wing is defined to satisfy the lateral stability requirements of the aircraft.

Lastly, the wingspan is chosen based on desired parameters such as the cruise and stall speeds, power required, range, structural complexity, percentage of wing area that flies in

disturbed flow caused by the UAV's structure, weight of wing, and the remaining available weight to transport payload.

Similarly to the method used for the airfoil selection, Equation 4.7 is utilized to compare the influence of the wingspan on the characteristics and performance of the aircraft.

$$P = \frac{n_1}{W_{Wing}} + \frac{R}{M_1} + \frac{n_2}{A_{dist}} + \frac{P_{req}}{M_2} \tag{4.7}$$

Once again, this approach considers every parameter to be equally significant and evaluates each of them relative to the best value obtained in that specific parameter, using the components of vectors 4.8 and 4.9. Vectors $\boldsymbol{N}$ and $\boldsymbol{n}$ contain the maximum and minimum values, respectively, that have been obtained from each parameter across all the wing spans. The comparison and scoring method is explained in section 4.3.3.

$$\boldsymbol{N} = [R\,;\ P_{req}] \tag{4.8}$$

$$\boldsymbol{n} = [W_{Wing}\,;\ A_{dist}] \tag{4.9}$$

A description for each parameter, and what is desired from them, is given bellow:

- W_{Wing}: Refers to the weight of the wing. Smaller values are desirable;
- R: Is the maximum expected range of the aircraft. Larger values are desirable;
- A_{dist}: Is the percentage of area of the wing that is affected by the disturbed flow caused by the structure. Smaller values are desirable;
- P_{req}: Refers to the power required to sustain cruise speed. Smaller values are desirable;

Additionally, there are two other factors that need to be taken into account. These are subjective parameters and relate to the structural complexity of the wing and the footprint of the UAV when the wing is mounted.

4.5 Winglet

Given that the winglet is designed as a lifting surface for stability purposes, it presents distinct characteristics compared to conventional winglets.

According to the literature, a significant improvement in directional stability can be achieved by incorporating a winglet with a cant angle (φ) of $0°$, a leading edge sweep angle of $25°$ and a taper ratio of 0.65 [51]. Additionally, the NACA 0010 was chosen as the airfoil for the winglet, based on its suitability for stabilizing surfaces [1]. As for the height of the winglet, it should

be determined through an iterative process based on the necessary surface area to meet the lateral-directional stability requirements of the UAV.

4.6 Control Surfaces

Regarding the control surfaces, the main objective is to determine the geometric parameters of the elevon. This is crucial because the size and position of the elevon influences the design of the internal structure of the wing. Additionally, it is necessary to account for the influence of its deflection on the pitching moment distribution.

Being the elevon a combination of an aileron and an elevator, it is sized to meet the requirements of both control surfaces. Table 4.2 shows the typical parameters and requirements for these surfaces.

Table 4.2: Commonly used parameters for aileron and elevator sizing [7].

Aileron	
Parameter	Requirement
S_a/S	$0.05 - 0.1$
b_a/b	$0.2 - 0.3$
c_a/c	$0.15 - 0.25$
$\delta_{a_{max}}[^\circ]$	$-22\,;+18$

Elevator	
Parameter	Requirement
S_e/S_h	$0.15 - 0.4$
b_e/b_h	$0.8 - 1$
c_e/c_h	$0.2 - 0.4$
$\delta_{e_{max}}[^\circ]$	$-25\,;+20$

In Table 4.2, S_a, b_a, c_a and $\delta_{a_{max}}$ represent the area, span, chord length, and maximum deflection of the aileron, respectively. Similarly, S_e, b_e, c_e and $\delta_{e_{max}}$ represent the area, span, chord length, and maximum deflection of the elevator, respectively. Finally, S_h, b_h, c_h represent the area, span, and chord length of the horizontal tail.

The most important parameters to consider are the areas of the aileron and elevon. Once the characteristics of the wing planform are defined, the area of the aileron can be easily calculated according to the requirements in Table 4.2. However, to determine the area of the elevator, it is necessary to calculate the area of the hypothetical horizontal tail using Equation 4.10.

$$v_h = \frac{l_h \cdot S_h}{\bar{c} \cdot S} \tag{4.10}$$

where v_h is the horizontal tail volume coefficient and l_h is the estimated distance from the tail quarter-chord to the wing quarter-chord.

In this instance, the value of v_h is determined based on typical values found in the literature [26], while the value of l_h is calculated from the distance between the quarter-chord of the wing and the furthest point where the elevon can be placed.

The area of the elevator is calculated by considering the value of the area of the hypothetical horizontal tail and the requirements specified in Table 4.2. With the areas of both the aileron and elevator, the area of the elevon is chosen to satisfy the area requirements of both control surfaces.

Finally, the chord percentage of the elevon is chosen from the same range as that of the aileron. This determines the span by default, considering the relationship between the area and chord of the elevon.

4.7 Stability Analysis

Regarding the stability analysis, it is performed using the theory of Etkin and Reid implemented in Flow5 [52]. This method calculates the stability derivatives using forward finite differences.

The stability analysis is performed for the angle of attack at which the moment coefficient of the aircraft is zero, using the uniform density triangular panels method, and considering the air properties at 3000 m of altitude.

This analysis evaluates the static and dynamic stability for both the longitudinal and lateral-directional conditions, as well as the static margin of the aircraft. The results of the longitudinal stability are presented in two symmetrical short-period modes and two symmetrical phugoid modes, while the lateral stability results are presented in a roll damping mode, a spiral mode, and two symmetrical dutch-roll modes.

The results obtained are subsequently used to conduct an evaluation of the handling qualities of the UAV. This is done to ensure that the UAV is statically stable on every axis and to verify if the dynamic modes align with the required values outlined in [7]. It is important to note that the handling quality standards are established for manned aircraft. Small UAVs typically exhibit higher natural frequencies, meaning that the results may appear worse than they actually are in practice [53].

4.8 Performance Analysis

The performance parameters of the UAV are evaluated in two different ways. Some parameters are calculated using the aerodynamic results, while others are defined to ensure the UAV can carry out all flight phases or perform certain maneuvers. These defined parameters or restrictions result in a minimum thrust and power required for the UAV.

The range and endurance are calculated for the cruise condition using Equations 2.11 and 2.10, using the aerodynamic characteristics of the wing and the specifications of the chosen battery. The required power curve is also calculated for the range of operating speeds of the aircraft using Equations 2.12 and 2.15, which take into account the geometrical and aerodynamic characteristics of the wing.

The performance parameters with defined restrictions include level constant-velocity turn, rate of climb, and cruise speed, which are mentioned in Section 2.1.3.1. Given that the UAV has VTOL capabilities, the parameters for takeoff and landing are not considered. With these

results and the weight of the fully loaded UAV, the minimum thrust required to meet all the conditions is calculated. Subsequently, a motor and propeller kit is selected ensuring it can generate at least this amount of thrust.

Furthermore, the available power across the defined range of operating speeds is assessed using the methodology described in [54]. This method takes into account the aerodynamic data of the wing, the specifications of the chosen motor, and the characteristics of the propeller to calculate the power available at any given airspeed. It factors in variations in current intensity and voltage to match motor shaft speed and power with propeller speed and absorbed power to obtain propulsive efficiency and propulsive power.

4.9 Flight Envelope

The maneuvering and gust envelopes are calculated using a combination of data obtained from the analysis of the wing and the maneuvering and gust load equations, which are presented in Section 2.1.6.2.

After obtaining these results, both envelopes are joined together using the same principles described in [1], which create a comprehensive flight envelope for the aircraft.

4.10 Aerodynamic Loads

Aerodynamic forces induce bending and torsional moments along the wingspan, making it crucial to compute their distribution. The semi-span lift distribution, bending moment, and shear force are obtained from Flow5 and imported into a spreadsheet program. These results are then adjusted to account for the required load factor along with the safety factor to determine the forces acting on the aircraft in its critical condition. The lift load is subsequently calculated and utilized in the structural analysis.

4.11 Structural Layout and CAD Model Design

The CAD model is an important step in the wing design process. Using the dimensions obtained from the wing design, the structure of the wing is created with the desired characteristics. This model allows to obtain the exact dimensions and define the correct distribution of the components. Given that the purpose of the model is to conduct structural analysis, these two aspects are essential to achieve accurate results. To better comprehend the process outlined below, it is important to have an understanding of the sections that were considered in the wing design, which are explained and displayed in Section 4.4.1.

Using SolidWorks, the design of the wing structure is created by following this steps:

1. Wing-shaped solid body: The first step is to import the curve of the airfoil into three separate panels and adjust these curves to the correct length and inclination. Next, three lines are generated to connect the airfoils together: a straight line connecting the leading edges, another straight line connecting the trailing edge of the airfoils on the second and third panels, and a curved line tangent to the latter one, connecting the trailing edges of the airfoils in the first and second panels. With these sketches, the *Loft Boss/Base* tool is used to create a solid body with the shape of the wing. This solid is then multiplied a number of times, using the *Move/Copy Bodies* tools, for a reason that is explained in the next step.

2. Main and rear spars: The spars are designed with a box shape for two main reasons: they are simpler to manufacture compared to I-shaped spars, and they offer superior torsional rigidity than C-shaped spars. To create the spars, two rectangles are sketched at specific percentages of the airfoil chord in the second and third panels. These rectangles are then connected using the *Loft Boss/Base* tool to form two solid bodies. A copy of the wing-shaped solid body is then combined with these bodies using the *Combine* tool, which creates two new solids from their common parts. This results in two spars that precisely follow the curvature of the airfoil, avoiding interferences or gaps when connecting the spars to the skin. Finally, the spars are extended from the second panel to the frame of the UAV using the *Extrude* tool. Note that the location of the second panel defines the maximum height of the spars and it is chosen considering the skin attachment concept presented in Section 3.5. The layout considers a rear spar mainly to act as the support structure of the elevon and to withstand the loads it generates.

3. Wing skin: To create the skin of the wing, the dimensions of the elevon are entered into a sketch and, using the *Extrude Cut*, this area is removed from a copy of the wing-shaped solid body. Afterward, the *Split* tool and the second panel are used to divide the body into two separate parts.

4. Ribs: To create the ribs, a sketch is made with a certain number of rectangles that have a defined thickness. The *Extrude Cut* tool is then used to cut the inverted area of these rectangles from a copy of the wing-shaped solid body, resulting in airfoils with the specified thickness. A copy of the solid bodies of the spars is then subtracted from these airfoils using the *Combine* tool, creating multiple new solids that form the parts of the ribs. The number of ribs is determined through an iterative process based on the results of the FEA.

5. Surface structure: The final step is to convert the solid bodies of the skin and spars into surfaces using the *Offset Surface* tool with an offset of 0 mm. This makes it possible to stack layers of materials on these surfaces, simplifying the process of defining their appropriate thickness. Since the ribs already have a defined thickness, they can remain solid bodies.

After the CAD model is completed, the spars, ribs, and wing skin are exported as three separate IGS files so that they can be imported into Ansys.

4.12 Composite Structure and Structural Analysis

The Ansys software is employed to assign materials and perform a static structural analysis on the wing. This requires a group of systems, which include three *Mechanical Model* systems, two *ACP (Pre)* systems, one *Static Structural* system, and two *ACP (Post)* systems. Figure 4.4 presents the Ansys workbench interface as well as the project schematic and the selected component and analyses systems.

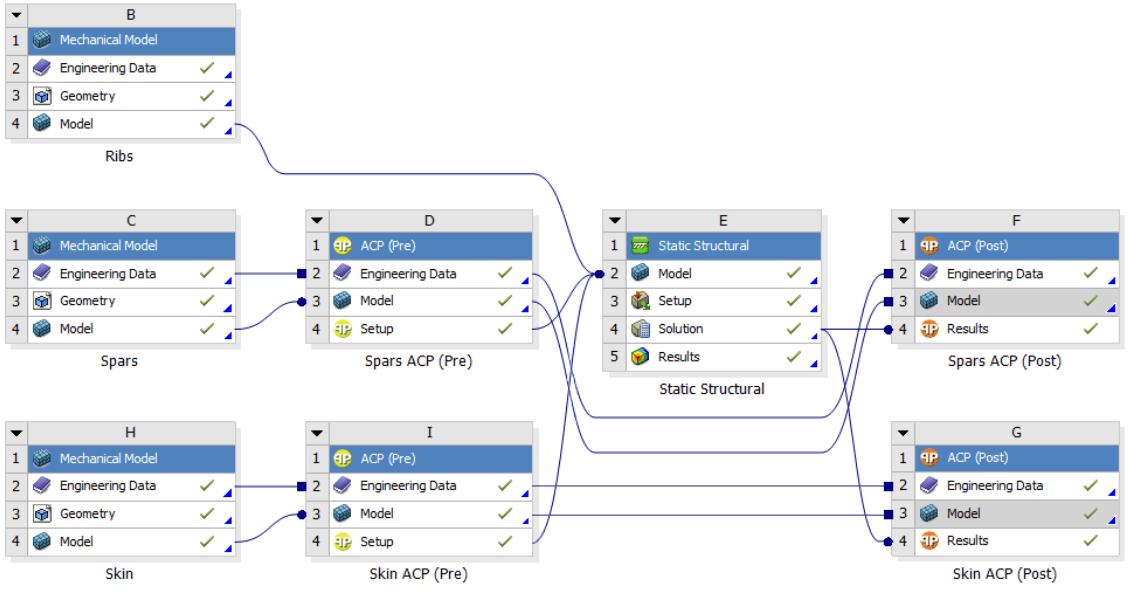

Figure 4.4: Ansys project schematic and systems.

The *Mechanical Model* systems are added to import the IGS files of the structural components of the wing and to select the desired materials that are going to be applied in each of those components. The mesh and element sets of the components are defined separately in the model section of each system. Additionally, since the ribs are intended to be made of a single material and are imported as solid bodies with their desired thickness already defined, their material is defined in this system.

The *ACP (Pre)* systems are added to create and apply laminates and sandwich materials to the spars and wing skin, which are imported as surfaces and defined separately. In the setup section of each system, the desired fabrics are created using the previously selected materials. Using these fabrics as plies, stackups are created by selecting the quantity and orientation of those plies to form the desired laminate. Next, rosettes are added to each element set to define the reference direction for the plies. Oriented selection sets are created to associate the rosettes with the element sets and to define the orientation of thickness. Finally, with the oriented selections and the stackups, modeling groups are created to determine in which surface each stackup should be attributed to.

The *Setup* of both *ACP (Pre)* systems, along with the *Model* of the ribs, are transferred to the *Static Structural* system to perform the FEA. The spars and wing skin are transferred as shell bodies, while the ribs are transferred as solid bodies. In this system, the contacts between

all the components are automatically generated and defined as bonded. The *contact tool* is then used to verify if all the contacts are closed. Subsequently, the boundary conditions are established by inserting a fixed support on the cross-section of the spar where it connects to the frame of the UAV and applying the semi-span lift load to the line representing the center of pressure across the wing, which is determined based on the CP distribution obtained from Flow5. This approach not only applies the correct bending moments and shear forces across the semi-span of the wing, but also accounts for the pitching moment that induces wing twist during level flight.

With the setup complete, the parameters of the analysis must be selected to obtain the desired solutions. The *Composite Failure Tool* is used to select the failure criteria and to implement the inverse reserve factor (IRF), which indicates the inverse of the structure's margin of failure. When the values of IRF range from 0 to 1, the integrity of the structure is non-critical. However, when the value exceeds 1, the structure demonstrates failure [55].

For the analysis, all fiber and matrix failure criteria are selected for both reinforced and sandwich materials to ensure that no type of failure is overlooked. The analysis utilizes the default constants from the the *Engineering Data* for the *Tsai-Wu*, *Puck*, and *LaRC* criteria. The selected failure criteria are depicted in Figure 4.5, and further details about each criterion can be found in [55].

Reinforced Ply Criteria	
Maximum Strain	On
Maximum Stress	On
Tsai-Wu	On
Tsai-Hill	On
Hoffman	On
Hashin	On
Puck	On
LaRC	On
Cuntze	On
Sandwich Criteria	
Face Sheet Wrinkling	On
Core Failure	On
Shear Crimping	On

Figure 4.5: Details of the *Composite Failure Tool*.

The analysis also takes into account the equivalent stress of the ribs, to ensure they can withstand the loads without fracturing, and the total deformation of the structure, to determine the maximum deflection at the wingtip. The results were obtained using the direct solver method, which is generally more effective than the iterative solver [56].

Once the analyses are complete, the *Solution* of the *Static Structural* system is transferred to separate *ACP (Post)* systems, one for the spars and another for the wing skin. This enables the visualization of the behaviour of each individual ply. Based on the results obtained from this analysis, the configuration of the stackups is adjusted to ensure that the structure can withstand the specified loads and that no critical failures occur in any of the composite layers.

Chapter 5

Preliminary Design

In this chapter, the steps that are described in the methodology are followed to determine the weights and distribution of the UAV's components; select the airfoil; size the wing, winglet, and control surfaces; analyse the aerodynamics, handling qualities, and performance of the UAV; calculate the flight envelope and aerodynamic loads applied to the structure; build a CAD model, determine the laminate composition of the structures, and conduct a finite element analysis on the final structure design.

5.1 Mass, Weight and Center of Gravity

As outlined in Section 4.2, the CG of the UAV is calculated using the inertia function of Flow5. This involves defining the weights or masses, and the mass center positions for each component of the UAV, as detailed in Section 4.1. Table 5.1 presents these components, along with their disposition, numeration, masses and weights.

Table 5.1: Mass center positions, masses and weights of the UAV's components.

#		1	2	3	4	5	6	7
Component		**Frame**	**Quad motors**				**Systems**	**Batteries**
Mass Center Position (m)	x	0.421	−0.355	−0.355	1.225	1.225	0.421	0.421
	y	0	0.795	-0.795	0.795	−0.795	0	0
	z	0.01	0.15	0.15	−0.02	−0.02	0.01	0.01
Mass [kg]		8.14	1.06	1.06	1.06	1.06	0.70	4.92
Weight [N]		79.85	10.40	10.40	10.40	10.40	6.87	48.27

#		8	9	10	11	12	13	14
Component		**Winglets**		**Payload**	**FFPS**	**Servos**		**Wing**
Mass Center Position (m)	x	1.076	1.076	0.502	1.1	0.9	0.9	0.547
	y	3	−3	0	0	2.08	−2.08	0
	z	0	0	0.01	−0.05	0	0	0.008
Mass [kg]		0.33	0.33	9.34	0.9	0.05	0.05	11
Weight [N]		3.24	3.24	91.63	8.83	0.49	0.49	107.91

Considering all these components, the method outlined in Section 4.2 is employed to determine the CG of the UAV, which is displayed in Table 5.2.

It's important to note that due to the mass center position of the payload, the CG of the UAV remains practically unchanged when the payload is removed. This design choice was made to ensure that the UAV retains its handling characteristics regardless of whether it is fully loaded, half-loaded, or not loaded at all.

Table 5.2: Center of gravity position, mass and weight of the UAV with payload.

CG		
Mass Center Position (m)	x	0.503
	y	0
	z	0.008
Mass [kg]		40
Weight [N]		392.4

For a clearer understanding of the disposition of the components and the coordinate system in use, Figure 5.1 illustrates the planform of the wing and the frame of the multirotor, with the components distributed and numbered according to Table 5.1.

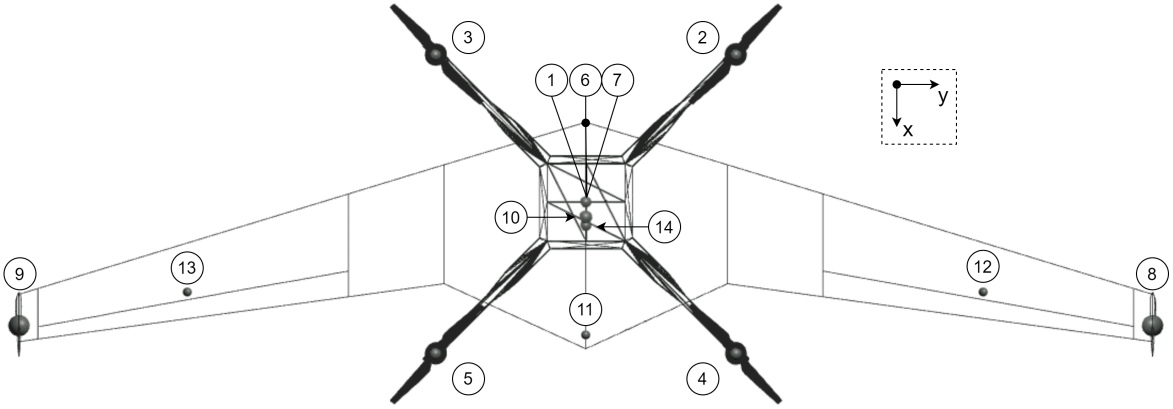

Figure 5.1: Mass center position distribution of the UAV's components.

The black dot on the leading edge at the center of the wing is the origin of the coordinate system and the direction of its axes is indicated within the square located above the right side of the wing.

5.2 Airfoil Selection

5.2.1 Reynolds Number

To determine the range of Reynolds number within which the aircraft will operate, Equation 2.4 is utilized. The values were obtained considering a maximum service ceiling of 3000 m which, according to the U.S. standard atmospheric model [47] and considering a temperature of $-4.5°$ Celsius during flight, corresponds to an air density of 0.9093 kg/m^3 and a dynamic viscosity of $1.694 \cdot 10^{-5}$ N.s/m^2.

For the chord length, the proposed conceptual design was used as a reference for the initial dimensions. Due to the large variation in chord length along the wing, the mean aerodynamic chord, equal to 0.868 m, was considered for the analyses.

Lastly, to ensure the best performance in various flight conditions, three different speeds were selected. These are detailed in Table 5.3.

Table 5.3: Reynolds number for stall, cruise and max speed.

	Desired Values for V [m/s]	**Reynolds number**
Stall Speed V_s	10	$500,000$
Cruise Speed V_c	20	$900,000$
Maximum Speed V_{max}	30	$1,300,000$

Since the Reynolds numbers constantly vary between different missions, it is not imperative to have exact calculations. Therefore, the numbers in Table 5.3 were rounded to the nearest hundred thousand to make them more practical to use.

5.2.2 Selection Results

As mentioned in Section 4.3, it was necessary to ensure sufficient space inside the wing to accommodate the frame of the quadcopter and all of its components. Considering this, an initial analysis was performed to the airfoils adjusted to a thickness ratio of 12%, based on the information gathered by the National Advisory Committee for Aeronautics (NACA), [57], which demonstrates that, for a variety of airfoils, this thickness ratio provides the highest value of lift coefficient. However, after it was observed that the initially best-performing airfoil demonstrated superior performance at a thickness ratio of 14%, the analysis was revisited for the airfoils adjusted to this thickness ratio. This allowed for a reassessment to determine if that particular airfoil continued to outperform the others.

With all the parameters defined, the relevant data points resulting from the analyses are extracted and transferred to a spreadsheet. Although XFLR5 provides a visual representation of the results through graphical displays, which are presented in Appendix A.1, transferring the data points to a spreadsheet allows for the precise measurement of the characteristics of each airfoil.

Tables 5.4 through 5.6 provide the measurements for the selected parameters of interest for each airfoil, which were outlined in Section 4.3.3, for the three Reynolds numbers previously defined.

Table 5.4: Results at Re $1,300,000$.

Airfoil	$(C_l/C_d)_{max}$	$(C_l^{3/2}/C_d)_{max}$	$C_{l_{max}}$	$C_{d_{min}}$	α_s	$C_{m_{mean}}$	BW	SQ
E186	100.16	94.36	1.25	**0.0051**	14.5	0.0267	1.22	**5**
E334	**129.02**	**149.90**	1.57	0.0061	14.5	0.0271	1.07	3
FX 69H083	97.62	96.97	1.43	**0.0051**	16	0.0223	0.93	4
HS132	103.29	112.54	1.46	**0.0051**	16.25	0.0108	1.04	4
HS522	110.08	115.57	1.58	0.0059	17	0.0115	1.36	4
MH60	107.95	110.85	1.49	0.0060	16	0.0061	**1.54**	3
NACA 24112	111.75	123.83	1.57	0.0063	16	0.0068	1.32	3
NACA M6	99.51	98.47	1.47	0.0055	**17.5**	0.0069	0.88	4
Prandtl-D root	119.08	113.84	1.25	0.0055	15	0.0221	1.12	3
PW51	104.06	112.62	**1.62**	0.0061	17	**0.0040**	1.53	3
S5010	112.11	118.30	1.53	0.0057	16	0.0046	1.32	4
S5020	114.54	121.24	1.58	0.0056	16	0.0043	1.18	4

Table 5.5: Results at Re $900,000$.

Airfoil	$(C_l/C_d)_{max}$	$(C_l^{3/2}/C_d)_{max}$	$C_{l_{max}}$	$C_{d_{min}}$	α_s	$C_{m_{mean}}$	BW	SQ
E186	100.99	93.79	1.21	0.0058	14	0.0243	1.31	**5**
E334	**117.68**	**138.55**	1.55	0.0060	14	0.0273	0.64	4
FX 69H083	98.01	97.24	1.36	**0.0056**	14.75	0.0238	0.95	4
HS132	99.04	103.20	1.43	**0.0056**	**16.5**	0.0131	0.99	4
HS522	100.30	104.86	1.51	0.0064	**16.5**	0.0124	1.27	4
MH60	98.51	100.71	1.46	0.0064	15.75	0.0066	1.45	3
NACA 24112	101.88	111.90	1.53	0.0068	15.5	0.0076	1.16	3
NACA M6	96.71	93.01	1.39	0.0058	15.75	0.0099	0.86	4
Prandtl-D root	117.57	114.81	1.23	0.0060	16	0.0248	1.16	3
PW51	94.66	101.69	**1.57**	0.0065	16.25	**0.0046**	**1.42**	3
S5010	102.22	107.26	1.49	0.0061	15.25	0.0048	1.26	4
S5020	104.61	109.77	1.53	0.0061	15.5	0.0049	1.20	4

Table 5.6: Results at Re $500,000$.

Airfoil	$(C_l/C_d)_{max}$	$(C_l^{3/2}/C_d)_{max}$	$C_{l_{max}}$	$C_{d_{min}}$	α_s	$C_{m_{mean}}$	BW	SQ
E186	89.18	85.39	1.18	0.0074	11	0.0218	**1.40**	**5**
E334	97.46	**112.13**	**1.51**	0.0083	13.75	0.0411	0.84	4
FX 69H083	91.21	92.10	1.27	**0.0069**	13.25	0.0297	1.04	4
HS132	87.57	87.94	1.33	0.0070	16.25	0.0173	1.28	4
HS522	84.66	86.96	1.41	0.0075	15	0.0138	1.18	4
MH60	83.06	83.89	1.39	0.0072	15.25	0.0080	1.28	3
NACA 24112	83.18	91.59	1.45	0.0077	14.75	0.0099	0.79	3
NACA M6	87.37	89.20	1.27	0.0075	**16.75**	0.0149	0.97	4
Prandtl-D root	**103.34**	105.61	1.21	0.0079	15	0.0322	1.30	3
PW51	79.18	83.68	1.47	0.0075	15	0.0063	1.27	3
S5010	85.90	88.31	1.41	0.0074	15	**0.0053**	1.22	4
S5020	87.53	91.22	1.44	0.0074	15.25	**0.0053**	1.16	4

The overall performance of the airfoils is presented in Table 5.7. Columns 2, 3, and 4 show the values obtained from Equation 4.5, while columns 5 and 6 show the average results obtained for the three Reynolds numbers considered, using Equations 4.5 and 4.6, respectively.

Table 5.7: Overall airfoil performance.

Airfoil	**Re** $1,300,000$	**Re** $900,000$	**Re** $500,000$	**Average 1**	**Average 2**
E186	5.94	6.23	6.23	6.13	5.45
E334	6.07	6.17	6.13	6.12	5.13
FX 69H083	5.78	5.96	6.06	5.93	5.22
HS132	6.23	6.34	6.49	6.35	5.61
HS522	6.46	6.52	6.37	6.45	5.69
MH60	6.51	6.64	6.51	6.56	5.84
NACA 24112	6.43	6.43	6.05	6.30	5.51
NACA M6	6.22	6.17	6.26	6.21	5.53
Prandtl-D root	5.75	6.11	6.20	6.02	5.18
PW51	6.95	6.98	6.65	6.86	6.15
S5010	6.94	7.07	7.05	7.02	6.27
S5020	**6.98**	**7.09**	**7.09**	**7.05**	**6.29**

Analysing the results presented in Table 5.7, it is possible to conclude that the S5020 airfoil, modified for 14% thickness ratio, exhibited the best overall performance and demonstrated the most consistent results throughout the analyses. Note that, even if considered an ex-

pression without the parameter associated with the maximum endurance, represented by "Average 2" in the table, the S5020 airfoil still exhibits superior performance. It was also verified that the results remained consistent when the trip location was changed to 0.3.

5.3 Wing Dimensions

As mentioned in Section 4.4.2, the wingspan is chosen based on certain desired parameters and on the results of the performance Equation 4.7. To better understand which is the optimal wingspan for the design, Table 5.8 presents the values of the selected parameters along with the results of the performance equation for five different wingspans.

Table 5.8: Characteristics and performance of wing planforms with different wingspans.

Wingspan [m]	$\mathbf{W_{Wing}}$ **[kg]**	**R [km]**	$\mathbf{A_{dist}}$	$\mathbf{P_{req}}$	**P**
4	7.2	132.5	84.1	423.2	2.82
5	9	144.2	67.9	336.6	2.95
6	11	152.9	55.9	282.6	3.12
7	12.8	160.8	48.5	246.6	3.30
8	14.5	166.9	42.7	220.5	3.50

Upon analysing Table 5.8, it becomes evident that a larger wingspan results in better overall performance. However, factors such as structural complexity and footprint must also be considered. A larger wingspan on a UAV results in a larger footprint, which can be a disadvantage given the intention of flying in urban environments. Additionally, a larger wingspan, in this particular case, results in a wing with higher aspect ratio, which requires a more robust structure and consequently increases the weight of the wing. Considering these two points, it was decided to opt for a middle ground and select a wingspan of 6 meters.

Table 5.9 presents the results of the methodology proposed in Section 4.4.2 for a wing with the selected wingspan. It provides detailed information on the characteristics of the wing, allowing for a comprehensive analysis of the design.

Table 5.9: Wing characteristics.

Parameter	**Symbol**	**Value**
Wing area [m^2]	S	3.353
Wingspan [m]	b	6
Aspect ratio	A	10.74
Mean aerodynamic chord [m]	MAC	0.663
Mean geometrical chord [m]	$\overline{c}$	0.56
Root chord [m]	c_r	1.20
Mid chord [m]	c_m	0.63
Tip chord [m]	c_t	0.25
Taper ratio	λ	0.4
Sweep angle [º]	Λ	12.6
Root angle of incidence [º]	α_{i_r}	4
Tip angle of incidence [º]	α_{i_t}	0
Wing twist [º]	α_{twist}	-4
Dihedral angle [º]	Γ	0

Note that the angle of incidence remains constant between the first and second sections, indicating that the wing twist only occurs from the second to the third section and, between those sections, the twist occurs linearly. Additionally, it is important to mention that the value of the taper ratio is calculated from the difference in chord size between the second and third sections.

Figure 5.2 depicts the final design of the wing planform, including some of the parameters mentioned above.

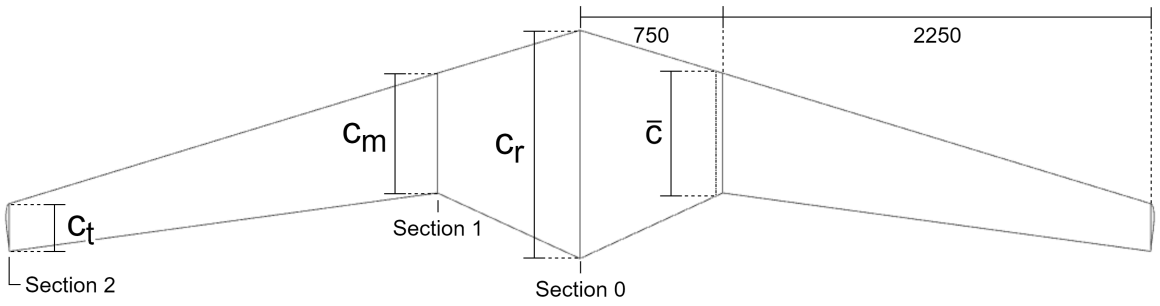

Figure 5.2: Wing planform.

5.4 Winglet

As mentioned in Section 4.5, the winglet is designed to ensure that the UAV meets the lateral-directional stability requirements. Table 5.10 presents the characteristics of the winglet.

Table 5.10: Winglet characteristics.

Parameter	Symbol	Value
Winglet area [m^2]	S	0.164
Winglet span [m]	b	0.8
Aspect ratio	A	3.9
Root chord [m]	c_r	0.25
Tip chord [m]	c_t	0.16
Taper ratio	λ	0.64
Sweep angle [°]	Λ	21.5
Toe angle [°]	α_{toe}	0
Winglet twist [°]	α_{twist}	0
Cant angle [°]	φ	0

The surface area of the winglet required for the UAV to fulfill the stability requirements is too large for a conventional winglet, as it would lead to an impractical vertical span and require additional structural components to prevent the winglet from failing. Consequently, it was decided that a winglet similar to a wingtip fence is better suited for this particular case. The fence can be designed with an equivalent surface area to the conventional winglet, but with the benefit of having only half of the vertical span, which results in less structural complexity for the overall design. Figure 5.3 depicts the final design of the winglet planform, including some of the parameters mentioned above.

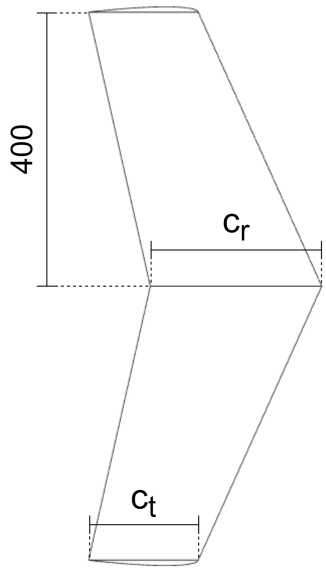

Figure 5.3: Winglet planform.

5.5 Control Surfaces

In this section, whenever a parameter related to the wing planform is mentioned, the values are taken from the results of Section 5.3.

To determine the appropriate area of the elevon, it is necessary to calculate the areas of both the aileron and elevator. However, to calculate the latest, an estimate the area of the hypothetical horizontal tail is needed. This is achieved using Equation 4.10, considering that v_h is equal to 0.5 and that l_h is around 0.7 m.

$$S_h = \frac{v_h \bar{c} S}{l_h} = \frac{0.5 \times 0.56 \times 3.353}{0.7} \approx 1.34$$

With this result and considering the parameters in Table 4.2, the areas of both the aileron and elevator can be determined and fall within the range of values presented in Equations 5.1 and 5.2.

$$S_a \in [0.05S, 0.1S] \equiv S_a \in [0.168, 0.335] \tag{5.1}$$

$$S_e \in [0.15S_h, 0.4S_h] \equiv S_e \in [0.201, 0.536] \tag{5.2}$$

Based on the results, it was decided to approximate the area of the elevon to the maximum area of the aileron, with a chord length equal to 25% of the wing chord. Additionally, a gap of 0.1 m was left between the tip of the wing and the tip of the elevon to ensure a sturdy foundation to attach the winglet. The final values of the elevon are presented in Table 5.11, where S_n is the sum of the area of both elevons.

Table 5.11: Elevon specifications.

Parameter	Symbol	Value
Elevon tip chord [m]	c_{n_t}	0.067
Elevon root chord [m]	c_{n_r}	0.136
Elevon span [m]	b_n	1.645
Elevon area [m^2]	S_n	0.334

To better understand the results, Figure 5.4 illustrates the wing planform along with the elevons and some of the respective parameters.

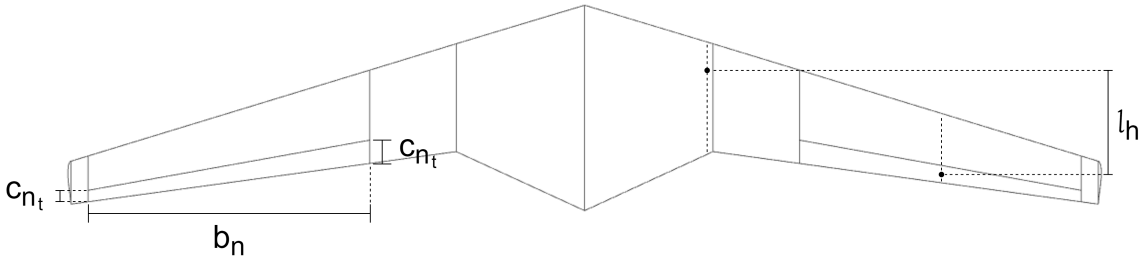

Figure 5.4: Elevon size and parameters.

5.6 Aerodynamic Characteristics

The key aerodynamic characteristics of the final wing design were extracted from Flow5 and are presented in Table 5.12 for both flight conditions, with and without payload. The wing model used for the analysis, along with the mesh quality, can be found in Appendix B.1.

Table 5.12: Aerodynamic characteristics.

Parameter	Symbol	With payload	Without payload
Maximum lift coefficient	$C_{L_{max}}$	1.23	1.23
Minimum drag coefficient	$C_{D_{min}}$	0.008	0.008
Lift coefficient at 0º	$C_{L_{\alpha_0}}$	0.405	0.405
Drag coefficient at 0º	$C_{D_{\alpha_0}}$	0.0126	0.013
Lift to drag ratio at 0º	$C_{L_{\alpha_0}}/C_{D_{\alpha_0}}$	32.15	31.21
Drag coefficient at zero lift	C_{D_0}	0.009	0.009
Stall speed [m/s]	V_S	14.4	12.6
Cruise speed [m/s]	V_C	25.2	22
Dive speed [m/s]	V_D	35.3	30.8
Wing Loading [kg/m^2]	W/S	117	89.7

Additionally, Figure 5.5 presents the aerodynamic results along the UAV operating range of angle of attack. Note that the obtained results do not account for the existence of a structure protruding from the wing. This means that it is probable that the lift coefficient results are overestimated, and the drag coefficient results are underestimated.

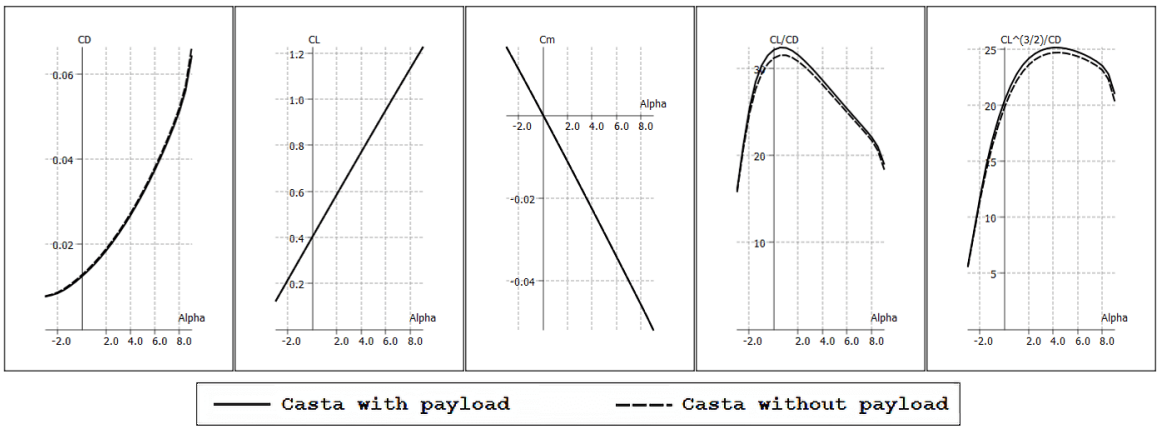

Figure 5.5: Aerodynamic characteristics of the wing with and without payload.

5.7 Handling Qualities

Given that the CG of the UAV remains unchanged when the payload is removed, the static stability results are identical for both the flight conditions, with payload and without payload. Therefore, Table 5.13 presents the static stability results that are representative of both flight conditions.

Table 5.13: Static stability analysis.

Requirement	Value	Result
$SM > 0$	0.06	Stable
$C_{m_\alpha} < 0$	-0.319	Stable
$C_{l_\beta} < 0$	-0.062	Stable
$C_{n_\beta} > 0$	0.037	Stable

Upon analysing Table 5.13, one can conclude that the all the static stability parameters indicate that the UAV is stable. However, the static margin is notably low and, depending on the reference considered, its value falls below typical values. Reference [7] indicates typical SM values within the range of 0.1 to 0.3, while reference [26] suggests a range of 0.05 to 0.2.

Conversely, the dynamic stability results are affected by the presence of the payload. Therefore, Tables 5.14 and 5.15 present the dynamic stability results of the UAV when it is not carrying the payload.

Table 5.14: Longitudinal dynamic stability flight quality results (without payload).

Mode	Eigenvalue	ω_n[rad/s]	ζ	Level
Short Period	$-7.178 \pm 10.367i$	12.6	0.569	1
Phugoid	$0.00043 \pm 0.548i$	0.55	0	3

Table 5.15: Lateral-directional dynamic stability flight quality results (without payload).

Mode	Eigenvalue	ω_n[rad/s]	ζ	$\zeta\omega_n$	T [s]	Level
Spiral	0.018	-	-	-	38.6	1
Dutch-Roll	$-0.127 \pm 2.884i$	2.88	0.044	0.127	-	2
Roll	-17	-	-	-	0.3	1

Tables 5.16 and 5.17 present the dynamic stability results of the UAV when it is carrying the payload.

Table 5.16: Longitudinal dynamic stability flight quality results.

Mode	Eigenvalue	ω_n[rad/s]	ζ	Level
Short Period	$-7.436 \pm 11.873i$	14	0.531	1
Phugoid	$-0.001 \pm 0.493i$	0.5	0.002	2

Table 5.17: Lateral-directional dynamic stability flight quality results.

Mode	Eigenvalue	ω_n[rad/s]	ζ	$\zeta\omega_n$	T [s]	Level
Spiral	0.016	-	-	-	44	1
Dutch-Roll	$-0.090 \pm 3.290i$	3.29	0.027	0.09	-	2
Roll	-19.44	-	-	-	0.24	1

The levels in the tables represent the level of acceptability of each parameter. These levels range from 1 to 3, with 1 meaning that the value of the parameter is clearly adequate for the flight phase, and 3 meaning that the aircraft is hardly controlled and the value is inadequate. This means that the minimum requirement is a level 3, but it is recommended to have at least a level 2 for every parameter.

However, as highlighted in Section 4.7, these handling quality standards are originally established for manned aircraft. Research has indicated that level 2 ratings and lower on small UAVs are equivalent to level 1 ratings in manned aircraft [53]. This can be attributed to the typically higher natural frequencies exhibited by small UAVs, implying that the stability results obtained are, in fact, better than they initially appear.

Analysing the tables, it is possible to conclude that all the results are satisfactory, with the exception of the phugoid mode, which is unstable in the manned aircraft standards. However, this instability is marginal to the extent that the damping remains at zero, implying that it can be practically categorised as level 2 in terms of acceptability. This issue can be further dismissed when considering that the UAV is designed to operate autonomously, and the autopilot is capable of effectively manage this problem.

5.8 Performance

5.8.1 Endurance and Range

As mentioned in Section 4.8, the endurance and range of the UAV are calculated for the cruise flight condition using Equations 2.10 and 2.11. Only one battery was considered, identical to those already in use in the UAV [58], with a mass of 2.46 kg and a specific energy of 198.5 Wh/kg. The propulsive system efficiency is considered to be 0.8, and the propeller efficiency is 0.72 at cruise speed based on results obtained from PropSelector. Table 5.18 presents the range and endurance results obtained for both flight conditions, with payload and without payload.

Table 5.18: Range and endurance results of the UAV.

Parameter	With payload	Without payload
Range [km]	82.97	105.13
Endurance [h]	0.92	1.32

Once again. it is important to note that, in addition to the overestimation of the C_L/C_D ratio obtained in the aerodynamic results, the value considered for the efficiency of the propulsive system may also be overestimated. Therefore, these results should be interpreted as representing the most favorable outcome.

5.8.2 Constraint Analysis

The constraint analysis was conducted based on the three parameters mentioned in Section 2.1.3.1. The calculations were performed considering both the cruise and maximum wing loading conditions, which represents the UAV at cruise speed with its payload.

The constraint for cruise speed is calculated using Equation 2.9, with the maximum service ceiling of 3000 m taken into consideration. This consideration also applies to all subsequent parameters.

$$\frac{T}{W_{TO}} = \frac{0.5 \times 0.91 \times 25.2^2 \times 0.0126}{117} + \frac{117}{0.5 \times 0.91 \times 25.2^2 \times \pi \times 10.7 \times 0.8} = 0.046$$

The constraint for the level constant-velocity turn is calculated using Equation 2.7, considering a 45^o bank angle turn, which is equivalent to a load factor of 1.41 during the maneuver.

$$\frac{T}{W_{TO}} = 0.5 \times 0.91 \times 25.2^2 \times \left[\frac{0.0126}{117} + \frac{117}{\pi \times 10.7 \times 0.8}\left(\frac{1.41}{0.5 \times 0.91 \times 25.19^2}\right)^2\right] = 0.061$$

The constraint for rate of climb is calculated using Equation 2.8, with a vertical speed of 3 m/s taken into consideration.

$$\frac{T}{W_{TO}} = \frac{3}{25.2} + \frac{0.5 \times 0.91 \times 25.2^2 \times 0.0126}{117} + \frac{117}{0.5 \times 0.91 \times 25.2^2 \times \pi \times 10.7 \times 0.8} = 0.165$$

Analysing the results, it is determined that the minimum thrust-to-weight ratio that satisfies all conditions is 0.165. With this value, the minimum thrust required is calculated using Equation 2.15.

$$T = 0.165 \times W_{TO} = 0.165 \times 40 \times 9.81 = 64.84\ N$$

Considering the minimum thrust required as a reference, the T-Motor AT5220 with a 19x10 propeller kit was chosen as the forward flight propulsive system of the UAV. This system not only delivers sufficient thrust but also achieves its highest propeller efficiency at a speed close to the cruise speed of the UAV. The specifications of this motor are presented in Table 5.19.

Table 5.19: T-Motor AT5220 specifications [24].

Parameter	Value
Static thrust [N]	73.7
Electrical power [W]	1957
Current [A]	96.8
Voltage [V]	20.2
Speed constant [rpm/V]	380

5.8.3 Power Curves

The required power curve for the UAV's range of operating speeds is calculated using the equations outlined in Section 2.1.3.3, resulting to the following formula:

$$P = \frac{1}{2}\rho V^3 S \left(C_{D_0} + \frac{\left(\frac{W/S}{\frac{1}{2}\rho V^2}\right)^2}{\pi A e} \right) = 0.5 \times 0.909 \times V^3 \times \left(0.008 + \frac{\left(\frac{117}{0.5 \times 0.909 \times V^2}\right)^2}{\pi \times 10.7 \times 0.8} \right)$$

The available power curve was obtained following the method described in Section 4.8, considering the motor and propeller kit presented in Section 5.8.2. The outcomes of both power curves are depicted in Figure 5.6.

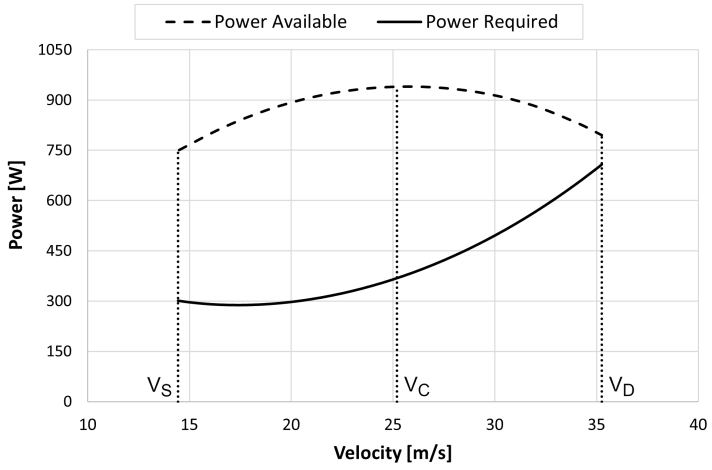

Figure 5.6: Available power and required power.

Upon examining Figure 5.6, one can conclude that the selected motor and propeller kit is well-suited for its intended purpose as the forward flight propulsive system as it provides sufficient power to cover the entire range of operating speeds for the UAV. However, it is important to mention that the values of the power required only consider the drag polar of the wing, as the aerodynamic analysis did not account for the effects of the exposed frame and landing gear of the UAV.

5.9 Flight Envelope

5.9.1 Maneuvering Loads

As mentioned in Section 2.1.6.3, the positive and negative limit manoeuvring load factors need to be defined and, according to EASA airworthiness standards [59], the positive limit load may not be less than 3.8 and the negative limit load may not be more than -1.5. Taking these specifications into account and considering that the UAV in intended for utility purposes, it was chosen to use those limit loads to ensure the maximum structural safety. The dive speed is another parameter that needs to be established and, according to the standards, it may not be less than 1.4 times the value of the cruise speed. Lastly, to calculate the stall curves, Equation 2.20 can be reformulated in a way that is possible to obtain the load:

$$n = \frac{\frac{1}{2}\rho V^2 C_{L_{max}}}{W/S} = \pm \frac{0.5 \times 0.9093 \times V^2 \times 1.21}{117}$$

5.9.2 Gust Loads

As mentioned in Section 2.1.6.4, the gust loads can be obtained using Equation 2.21. However, its necessary to calculate the subsonic lift-curve slope first. According to the literature, the value of k is typically assumed to be 1 across all Mach numbers and the value of β, for low airspeeds, is often assumed to be 1 as well. Using this approach, the lift-curve slope can be determined as follows:

$$C_{L_\alpha} = \frac{2\pi \times 10.74}{2 + \sqrt{\left(\frac{10.74 \times 1}{1}\right)^2 \left(1 + \frac{tan^2(12.635)}{1^2}\right) + 4}} = 5.117$$

Then, the mass ratio is obtained using the following equation:

$$\mu = \frac{2 \times 117}{0.9093 \times 9.81 \times 0.56 \times 5.117} = 9.159$$

Which leads to the calculation of the alleviation factor for subsonic flight:

$$K = \frac{0.88 \times 9.159}{5.3 + 9.159} = 0.557$$

Lastly, the gust load factors can be calculated by substituting the values obtained above into Equation 2.21. Additionally, it is also necessary to determine the speeds of the vertical gusts that occur during flight. According to EASA airworthiness standards, gusts of 15.24 m/s at cruise speed and gusts of 7.62 m/s at diving speed must be considered. Therefore, the gust load factor at cruise speed can be expressed as:

$$n = 1 \pm \frac{0.5 \times 0.903 \times V_C \times 5.117 \times 0.557 \times 15.24}{117}$$

And the gust load factor at diving speed is given by:

$$n = 1 \pm \frac{0.5 \times 0.903 \times V_D \times 5.117 \times 0.557 \times 7.62}{117}$$

5.9.3 Envelope Results

Using the previously presented equations, the positive and negative limit loads and the defined speeds on Table 5.12, the maneuvering and gust loads are calculated for the range of speeds within which the UAV is expected to operate. Figure 5.7 displays both the maneuvering and gust loads, along with the combined envelope.

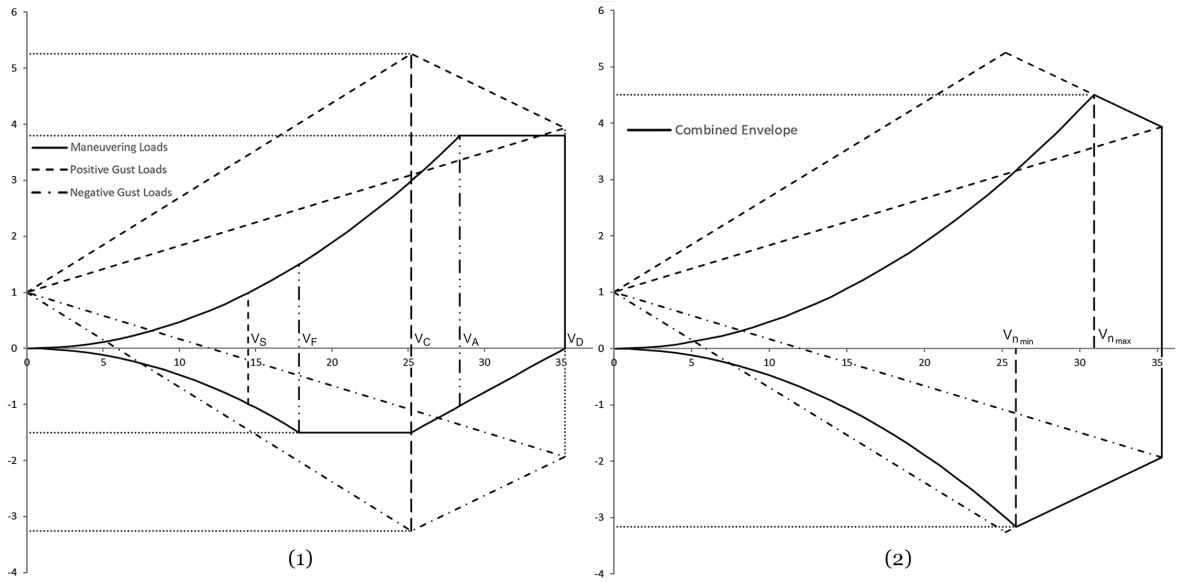

Figure 5.7: Maneuvering and gust loads (1) and combined envelope (2).

The relevant data from the plotted graphs is shown in Table 5.20, where $V_{n_{max}}$ represents the speed at which the load is maximum, and $V_{n_{min}}$ represents the speed at which the load is minimum.

Table 5.20: Combined envelope specifications.

	V [m/s]	**n+**	**n-**
V_S	14.5	0.99	-0.99
V_C	25.2	2.99	-1.50
V_D	35.3	3.80	0
V_A	28.4	3.80	-1.02
V_F	17.8	1.50	-1.50
$V_{n_{max}}$	30.9	4.50	–
$V_{n_{min}}$	55.9	–	-3.16

Analysing the results, it is possible to conclude that the maximum load factor the UAV can

experience, and needs to withstand, is 4.5. Therefore, this is the load factor utilized to size the structure of the wing.

5.10 Aerodynamic Loads

The semi-span lift distribution, bending moment and shear stress are illustrated in Figures 5.8, 5.9 and 5.10, respectively. The values used to generate these graphs are obtained from Flow5 and scaled by the load factor of 4.5 and a safety factor of 1.5. This results in values 6.75 times greater than the original values.

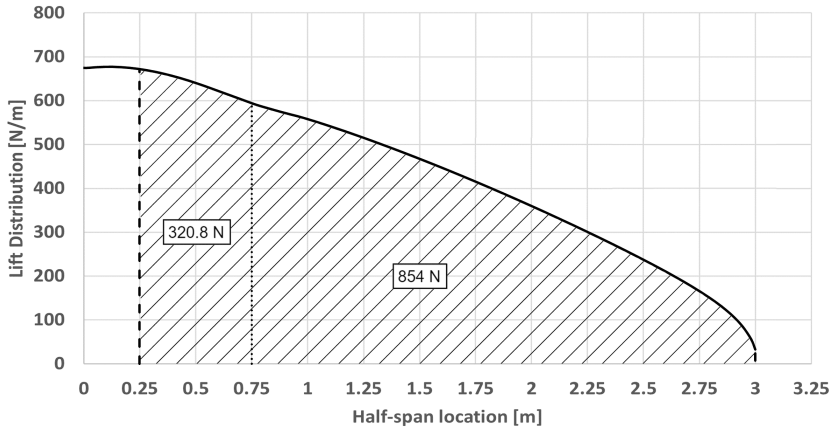

Figure 5.8: Lift distribution.

The hatched area in Figure 5.8 consists of two sections that equate to a total lift of 1174.8 N. The first sections represents the lift applied to the spar, while the second represents the lift applied to the wing skin. This is further explained in Section 5.13.2 with more detail.

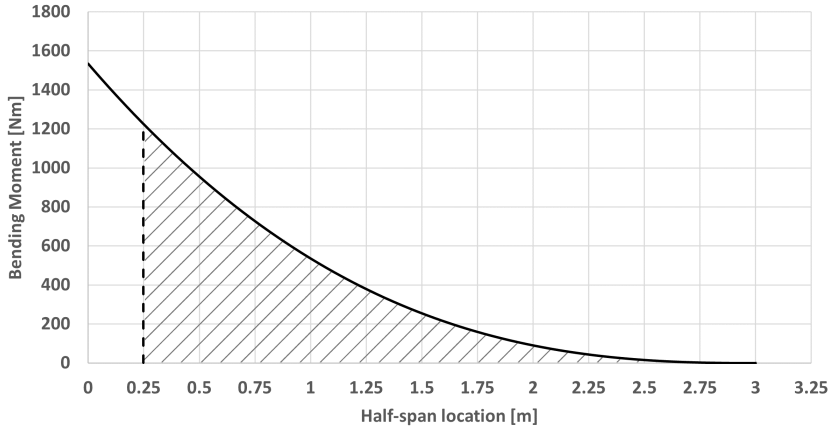

Figure 5.9: Bending moment.

The hatched area of the graphs represents the loads or forces that act on the structure of the wing since the connection between the wing and the structure of the UAV occurs at a distance of 0.25 m from the center line.

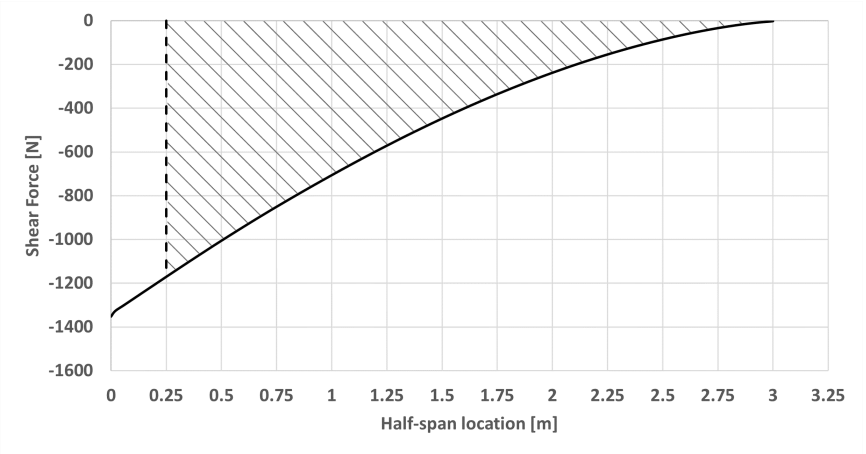

Figure 5.10: Shear stress.

5.11 Structural Layout and CAD Model Design

Figure 5.11 depicts the wing-shaped solid body along with the three airfoil curves that define the shape of the wing. The design process for this part is detailed in the first step of the CAD design, presented in Section 4.11, and takes into account the measurements from Table 5.9 to determine the part's dimensions.

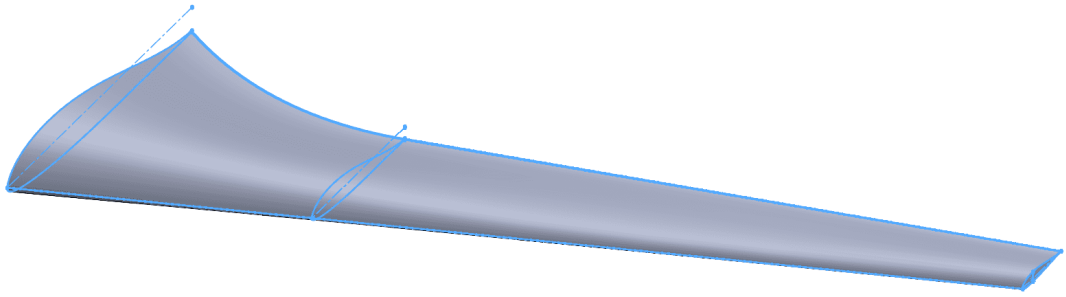

Figure 5.11: Wing-shaped solid body.

Figure 5.12 presents the result of the second step of the CAD design from which results the main and rear spars. The center of the spars, represented as the rectangles in the sketch, were set at a 27.7% and 75% of the chord. This means that the main spar is located at the thickest point of the airfoil, while the rear spar is positioned as far back as possible, considering the dimensions of the elevon. Both of these decisions are supported by the information presented in Section 2.1.6.

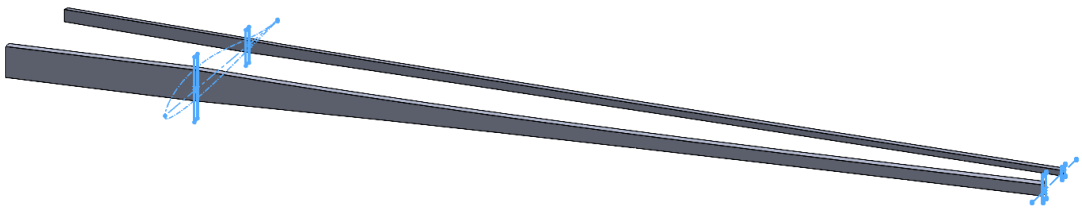

Figure 5.12: Spar solid bodies after *Combine* and *Extrude*.

Figure 5.13 showcases the solid body of the wing skin, which results from the third step in the CAD design process. This corresponds to the portion of the wing skin between sections 1 and 2, which are depicted in figure 5.2.

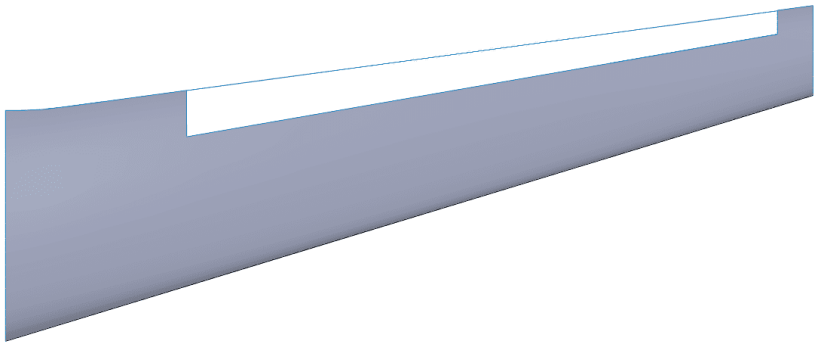

Figure 5.13: Wing skin solid body.

Figure 5.14 presents the rib parts obtained through the process described in the fourth step of the CAD design. It was determined that a minimum of five ribs were required: one rib at each end of the wing skin, one rib at each end of the elevon, and one rib aligned with the center of the aileron. This configuration was chosen to ensure that the wing skin retains its shape and efficiently transfers loads to the spars, which was later confirmed in the structural analysis.

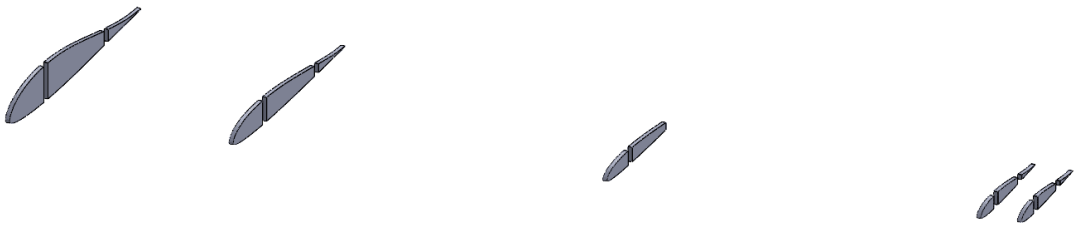

Figure 5.14: Rib parts.

Finally, Figure 5.15 presents the final wing structural model. The spars and wing skin are modeled as surfaces and the rib parts as solid bodies.

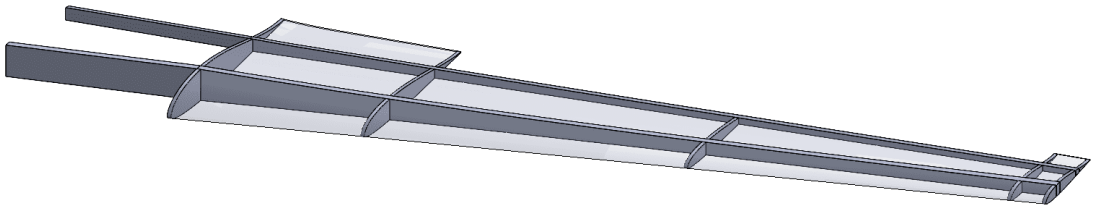

Figure 5.15: Wing structural components.

5.12 Composite Structure

5.12.1 Material Selection

Table 5.21 presents the materials considered for the structure of the UAV, where "E" is the Young's modulus, "G" is the shear modulus, and "ν" is the Poisson's ratio. The values are sourced from the engineering data sources of Ansys, as well as from references [60] and [61].

Table 5.21: Material characteristics and properties.

Material	Epoxy carbon UD prepreg	Epoxy carbon woven prepreg	PVC foam
Thickness [mm]	0.142	0.195	20
Density [kg/m^3]	1540	1480	80
E_1 [N/mm^2]	209000	91820	102
E_2 [N/mm^2]	9450	91820	102
G_{12} [N/mm^2]	5500	3600	39
ν_{12}	0.27	0.05	0.3

The epoxy carbon unidirectional (UD) prepreg was selected as the primary material for the spar caps, as it provides the highest tensile and compressive strength, along with the highest bending stiffness in the fiber direction.

The epoxy carbon woven prepreg was employed for the spar webs and the top and bottom layers of the spar caps. This decision was based on the material's similar shear resistance and reduced matrix tension relative to epoxy carbon UD prepreg in a stacking sequences of $[45/-45]$. The structural analysis also demonstrated that the epoxy carbon woven prepreg is more effective in distributing the load across the spar, which reduces the maximum stress at the root of the spars. This material is also utilized as the sandwich facings of the wing skin due to its resistance to impact forces and crack growth.

The PVC foam was selected as the core material for the wing skin due to its low density and easy availability. The use of this material in a sandwich composite core offers the added benefit of providing 100% contact area with the facings, which distributes impacts over a larger area compared to honeycomb materials, for example. The PVC foam was also chosen for the ribs due to its tensile and compressive strength, which is sufficient to transfer the wing torsion to the spars, and due to its rigidity, which is enough to maintain the intended shape of the wing skin, all while remaining lightweight.

It was decided to use a foam-cored carbon fiber sandwich for the wing skin due to its high flexural stiffness, which prevents the skin from buckling. This allows the skin to maintain its original shape, thereby preserving optimal aerodynamic properties.

5.12.2 Stacking Sequence

The stacking sequence of lamina that constitutes the components was established considering the composite design rules, outlined in Section 2.1.7.3, and the manufacturing process.

However, it was not possible to adhere to all the design rules as they would either make the manufacturing process impossible or add unnecessary weight to the structure. The stacking sequence of the components of the structure are presented in Table 5.22, along with their corresponding thickness.

Table 5.22: Composite details of each component.

Component	Composite Sequence	Thickness [mm]
Main spar cap	$[45_{W_2}/0_{U_4}]_S$	1.916
Main spar web	$[45_W]_S$	0.39
Rear spar cap	$[45_{W_2}/0_U]_S$	1.064
Rear spar web	$[45_W]_S$	0.39
Wing skin	$[45_W/Core_{PVC}/45_W]$	2.39

To better comprehend the information on Table 5.22, consider the following:

- In the composite sequence, the subscript "W" denotes that the material of the corresponding lamina is an epoxy carbon woven prepreg and the "U" signifies it is an epoxy carbon UD prepreg. For the sandwich core, the subscript "PVC" indicates that the applied material is PVC foam. Additionally, the "S" signifies that the sequence is symmetric, essentially doubling the designated layers.
- The numbers adjacent to the subscripts represent the quantity of consecutive layers of that specific material.
- The fiber orientation depends on the specific component to which the material is applied. In the case of the spars, a 0^o orientation implies that the fibers are aligned with the direction of the respective spar. For the wing skin, a 0^o orientation indicates that the fibers are aligned parallel to the direction of flight.

5.12.3 Manufacturing Process

The envisioned manufacturing process involves vacuum bag molding, which aligns with the equipment available at CEiiA.

Main Spar

Given that the main spar is practically symmetrical along the vertical axis, it can be manufactured using a single "C" shaped female mold. The proposed manufacturing process of the main spar consists of three steps:

1. Laminate the established amount of layers of epoxy carbon UD prepreg at a 0^o angle in either the left or right side of the mold, followed by laminating a "C" shaped profile using a single layer of epoxy carbon woven prepreg at a 45^o angle. This process is then repeated to obtain to identical parts.

2. Bond the two parts together, inserting a solid piece of foam in between, to create a rectangular component with the epoxy carbon UD prepreg layers on opposite sides. The foam aids in bonding the two parts in the desired shape and provides additional structural benefits such as preventing the spar webs from buckling and improving the stiffness of the spar.

3. Laminate the top, bottom and left side of the component with a single layer of epoxy carbon woven prepreg at a 45^{o} angle, followed by laminating the top, bottom and right side of the component with a another single layer of epoxy carbon woven prepreg at a 45^{o} angle.

Figure 5.16 illustrates the three steps of the manufacturing process proposed for the main spar, along with the cross-section of the component that displays the orientations considered, which aids in understanding the steps described in the manufacturing process and serves as a reference for the structural analysis.

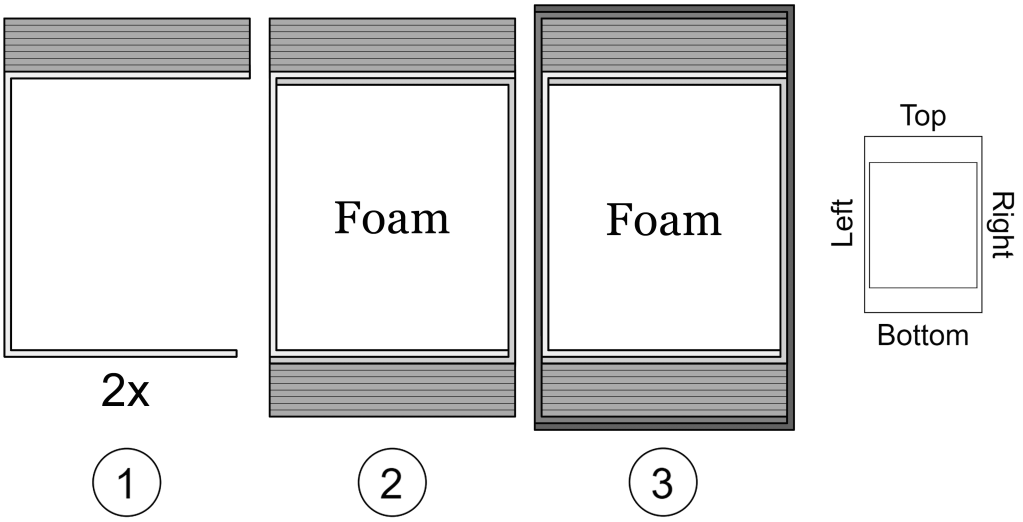

Figure 5.16: Manufacturing process of the main spar and orientations considered.

Rear Spar

The rear spar can be manufactured following the same principles presented for the main spar. The main differences in the manufacturing process include the number of epoxy carbon UD prepreg layers applied to spar caps and the need for two molds to create the first two parts of the spar due to its asymmetrical shape along the vertical axis.

Wing skin

The manufacturing process of the wing skin can be accomplished in a single step. Using a male mold of the shape of the wing, a layer of epoxy carbon woven prepreg at a 45^{o} angle is placed on the mold, followed by the PVC foam as the core material, and another layer of

epoxy carbon woven prepreg, also angled at 45^{o}. If the mold proves to be too complex, the processes can be divided into two steps, manufacturing the top and bottom parts of the skin separately using two female molds. These parts are then bonded to the structure after all the other components have been assembled.

5.12.4 Wing Structural Mass

The mass of the structural components of the wing were obtained using the *sensor* functionality of the Ansys *ACP (Pre)* system and are presented in Table 5.23. The total mass indicated in the table results from multiplying the mass of each component by its respective quantity. This value is then multiplied by 1.1, which corresponds to a mass increased of 10%, to account for the additional material required to bond all the components together.

Table 5.23: Mass of each structural component.

Component	Mass [kg]	Quantity
Main spar	0.742	2
Rear spar	0.342	2
Rib parts	0.058	2
Wing skin	1.255	2
Top cap	0.969	1
Bottom cap	0.953	1
Elevon	0.210	2
Winglet	0.285	2
Total ($\times 1.1$)	8.477	

Given that structural analyses was not conducted on components such as the top and bottom skin caps, the elevon, and the winglet, the composition of these components was not determined. However, to account for their weight, it is assumed that they are composed as follows:

- The top and bottom caps are made of a foam-cored carbon fiber sandwich, identical to that defined for the wing skin.
- The elevon and the winglet are made of PVC foam with a single layer of epoxy carbon woven prepreg on the outside.

5.13 Structural Analysis

5.13.1 Mesh Details

The mesh for each component was generated using quadratic elements with varying sizes depending on the component. To simplify the mesh setup, the element size was kept uniform across the entire model of the components. The mesh details for each component are provided in Table 5.24.

Table 5.24: Mesh details of each component.

Component	Element size [mm]	Number of nodes	Number of elements
Spar	2	172384	172262
Skin	5	61805	61137
Ribs	3	165870	32680

Given that the spars are the the primary load-bearing components of the structure, their mesh was generated with a finer size to increase the accuracy of the results. The mesh was minimized as much as possible, taking into account hardware limitations. The mesh of the remaining components also kept as fine as possible, but due to the large number of elements in the analysis and the limited computational power, these components were assigned a larger mesh size. The analyses were conducted on a laptop that is equipped with an Intel i7 8th gen processor and 16 GB of RAM. Figure 5.17 displays the mesh of the structural components in the final 50 mm of the wing.

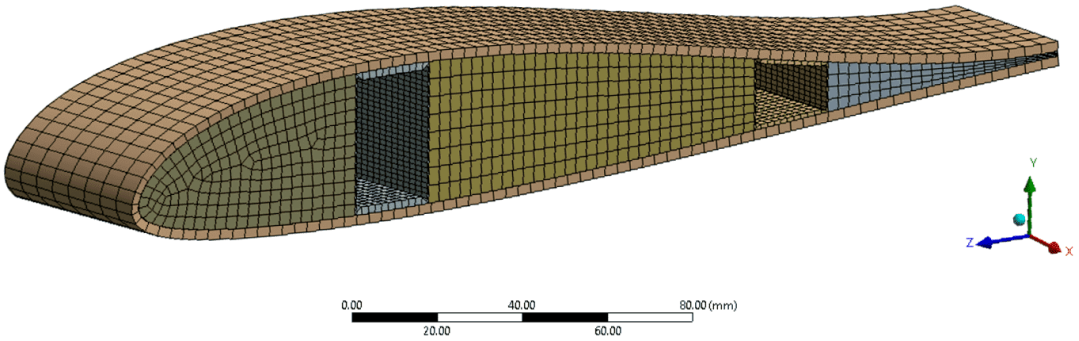

Figure 5.17: Mesh details of the structural components.

To reduce the computational time and processing power required to perform the analyses, the adaptive meshing method could have been employed. This approach would result in components with a fine mesh on the elements where the stress or strain are concentrated, and a coarse mesh elsewhere in the component. This would achieve the same level of result accuracy as a component with a uniformly fine mesh, but with significantly fewer elements [62]. However, this method requires additional steps during the mesh setup process and it was determined that a uniform mesh with the specified sizes in Table 5.24 was adequate to obtain accurate results.

5.13.2 Boundary Conditions

Although there should be an attachment and detachment system to connect the structure of the wing to the frame of the UAV, to simplify the structure and the analysis, the spars are considered to be fixed at the root, where they connect to the frame of the UAV.

The lift load should be applied at the center of pressure of the wing, extending from the root of the spar (where the spar connects to the UAV's frame) to the wingtip. However, given that the skin caps are attachments and are not considered in the analysis, the total lift is divided

into two parts: the lift distribution from the spar root to the start of the skin is applied to the visible portion of the main spar cap, and the lift distribution from the start of the skin to the wingtip is applied to the line on the surface of the skin. This line represents the center of pressure distribution across that section and is detailed in Table 5.25. This leads to a force of 320.8 N being applied on the spar cap and a force of 854 N on wing skin, resulting in a total of 1174.8 N that the structure needs to withstand. These values already account for the load factor of 4.5 and the safety factor of 1.5 and have been previously determined in Section 5.10.

Table 5.25: Center of pressure distribution along the semi-span.

Semi-span location [m]	CP position [% of the chord]
0.00	20.50
0.50	22.84
1.00	24.47
1.50	24.73
2.00	25.03
2.50	25.53
3.00	21.61

Splitting the lift load into these two parts is a feasible approach for two reasons: Firstly, given that the loads are applied as uniformly distributed loads, this division allows for a more precise allocation of the lift load, resulting in a more realistic representation of the real scenario. Secondly, considering that the position of the spar is closely aligned with the center of pressure, the torsion due to lift in the section is not significantly underestimated. The boundary conditions are shown in Figure 5.18.

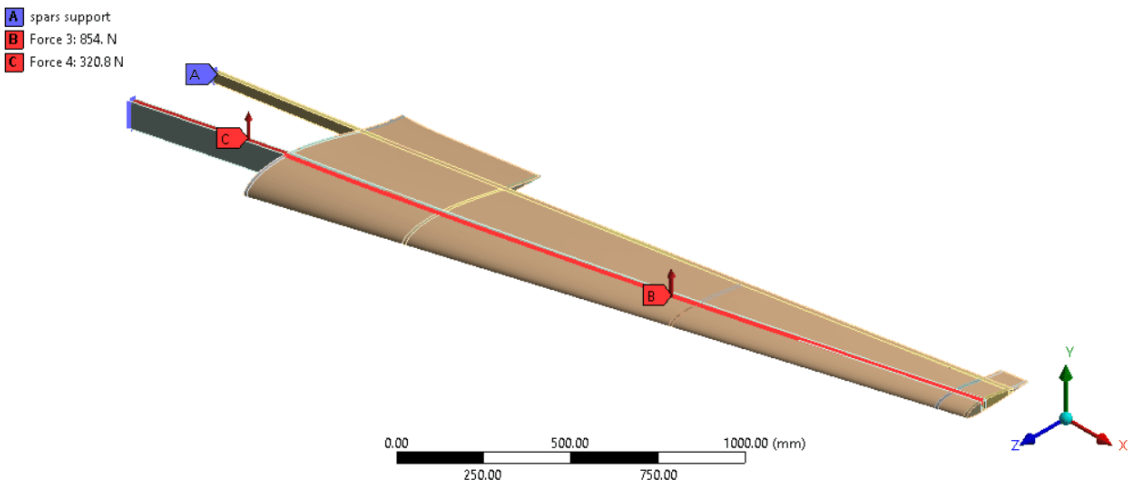

Figure 5.18: Boundary conditions applied to the structure.

Table 5.26 presents the elements included in the analysis, along with their respective description and application.

Table 5.26: Element types, classification and application [25].

Element	Element code	Description	Application
Solid	SOLID186	3-D 20-Node Structural Solid 20 nodes 3-D space DOF: UX, UY, UZ	Rib parts
Shell	SHELL181	4-Node Structural Shell 4 nodes 3-D space DOF: UX, UY, UZ, ROTX, ROTY, ROTZ	Spars and wing skin
Contact	CONTA174	3-D 8-Node Surface-to-Surface Contact 8 nodes 3-D space DOF: UX, UY, UZ, TEMP, VOLT, MAG	Connections
Target	TARGE170	Contact 3-D Target Segment 8 nodes 3-D space DOF: UX, UY, UZ, TEMP	Connections
Surface	SURF156	3-D Structural Surface Line Load 3 to 4 nodes 3-D space DOF: UX, UY, UZ	CP distribution line
	SURF154	3-D Structural Surface Effect 4 to 8 nodes 3-D space DOF: UX, UY, UZ	Main spar cap top surface

5.13.3 FEA Results

As mentioned in Section 4.12, the analysis was conducted to determine the total deformation and IRF of the structure, and the equivalent stress of the ribs.

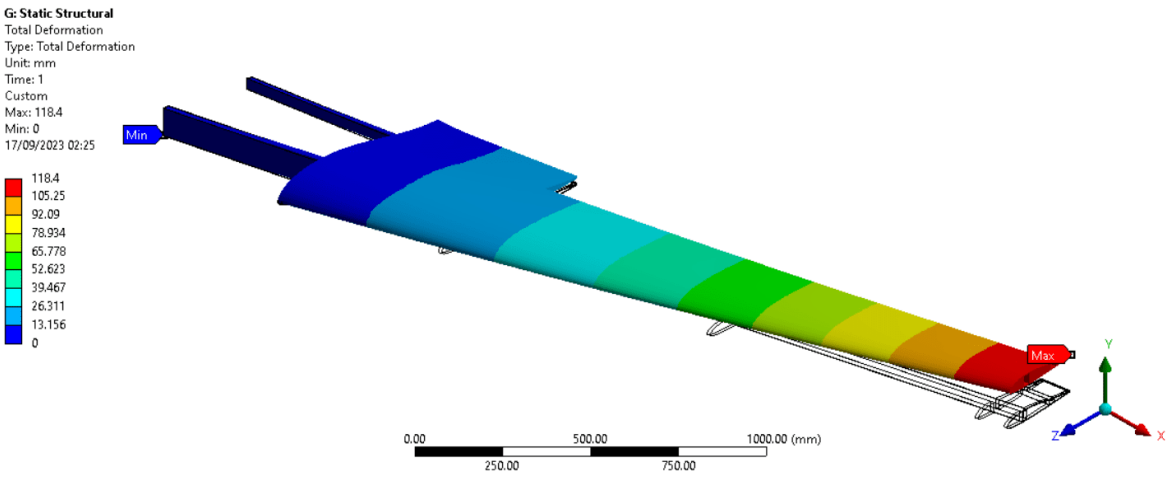

Figure 5.19: Total deformation [mm].

The total deformation results are illustrated in Figure 5.19, showing that the wingtip reaches a maximum deflection of 118.4 mm, which equates to approximately 4% of the semi-span. Additionally, using probes to measure the displacement of two different points on the wing tip, it was determined that the wingtip experiences a maximum torsion of 1°. Both of these measurements are quite satisfactory, as they indicate that the shape of the wing does not undergo significant alterations.

The IRF results are displayed in Figure 5.20 along with a detailed view of the most critical section of the wing. Upon examining the figure, it can be deduced that the structure can

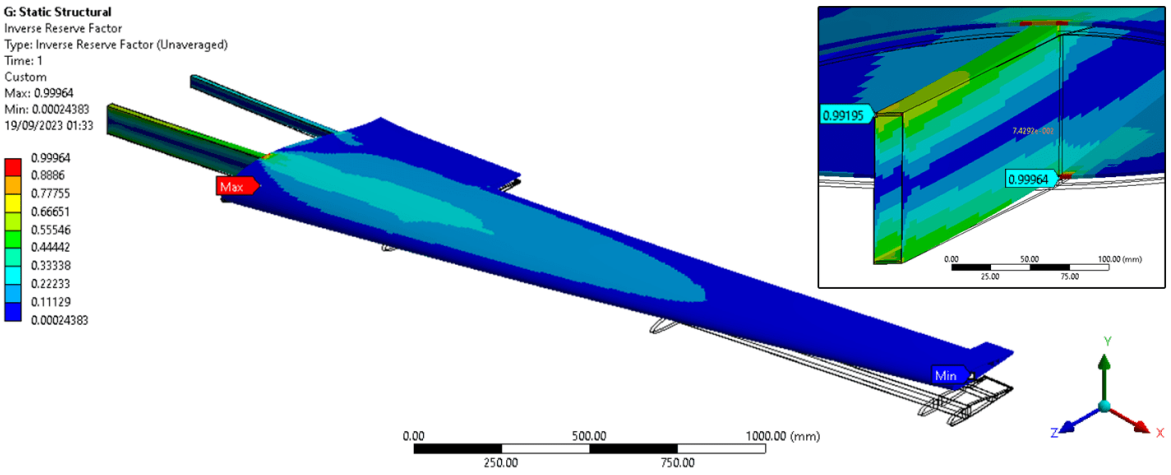

Figure 5.20: Inverse reserve factor.

withstand the applied loads without reaching critical failure. The forces are primarily concentrated on the spar caps near the root, with a peak IRF of 0.992. This value was obtained in the left layer of the main spar's right shear web and is associated with the Tsai-Wu failure criterion. However, the maximum IRF in the structure was found in the wing skin in the region where it connects to the spar. The IRF reaches a value of 0.999 in the core material, which is related to the core failure criterion.

Figure 5.21 displays the equivalent stress results of the ribs along with a zoomed-in section highlighting the area with the highest stress values. It can be observed that the forces are primarily concentrated around the perimeter of the ribs where they connect to the spars and wing skin. The maximum stress value is 0.843 MPa, which is less than half of the material's tensile strength. This demonstrates that the material can comfortably withstand the applied loads.

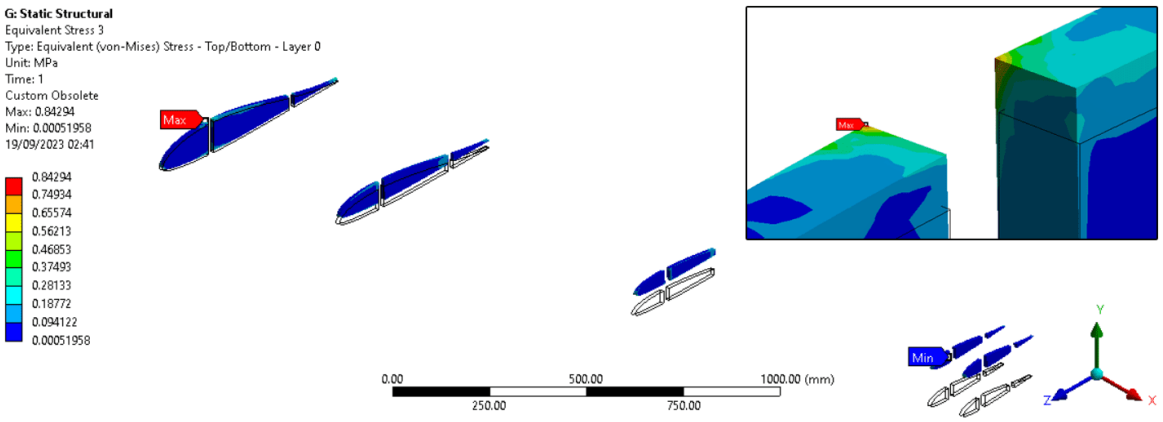

Figure 5.21: Ribs equivalent stress.

It is worth mentioning that the analysis was conducted without a foam core inside the spars, which was an option that was discussed as a viable addition to the manufacturing process in Section 5.12.3. This suggests that if the foam core was to be incorporated, the structure's ability to withstand applied loads would presumably increase.

5.14 3D Models

5.14.1 Aerodynamic Design

The aerodynamic design refers to the 3D model obtained from the aerodynamic analysis, which was developed using the Flow5 software. Figures 5.22 and 5.23 display the wing model from two distinct perspectives.

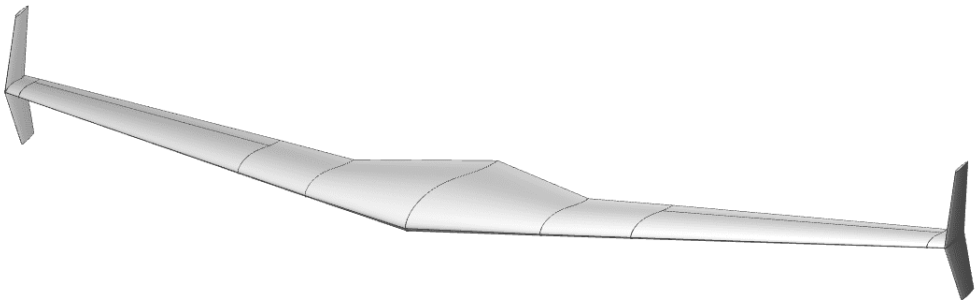

Figure 5.22: Aerodynamic wing model - dimetric view.

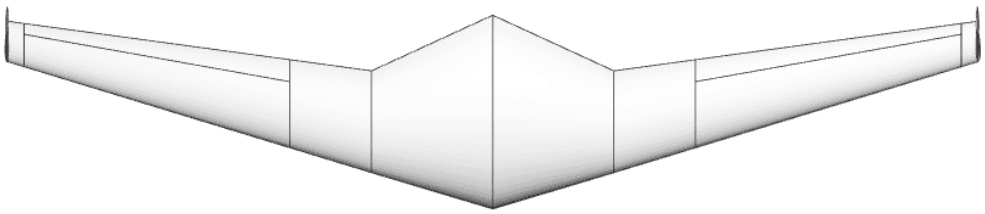

Figure 5.23: Aerodynamic wing model - top view.

Additional figures of the aerodynamic wing model, integrated with the model of the multirotor's frame, are available in Appendix B.2. These models were merged in the Flow5 software to verify the alignment and dimensions of the wing.

5.14.2 Structural Design

The structural design refers to the 3D model obtained from the structural analysis, which was developed using the SolidWorks software. Figure 5.24 displays the structural model integrated with the frame of the UAV.

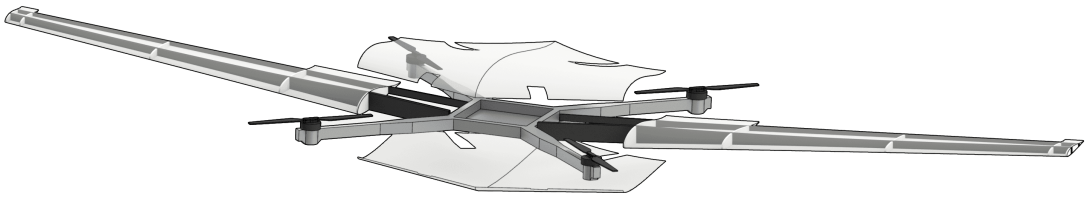

Figure 5.24: Final structural design with transparent wing skin and caps - dimetric view.

5.14.3 Final Design

The final wing design is shown in Figures 5.25 and 5.26 from two distinct angles. The model was developed using the SolidWorks software, considering the aerodynamic characteristics, the structural layout, and the constraints imposed by the frame of the UAV.

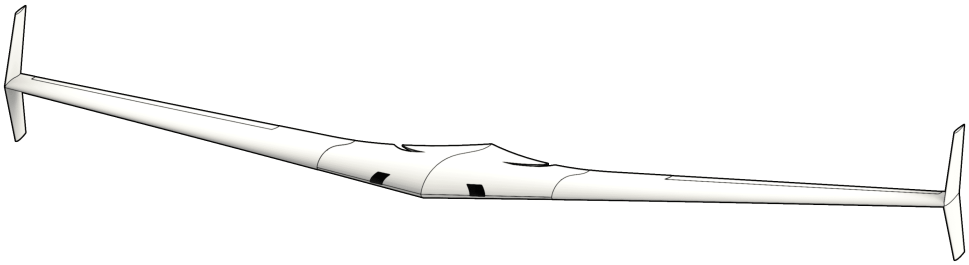

Figure 5.25: Final wing model - dimetric view.

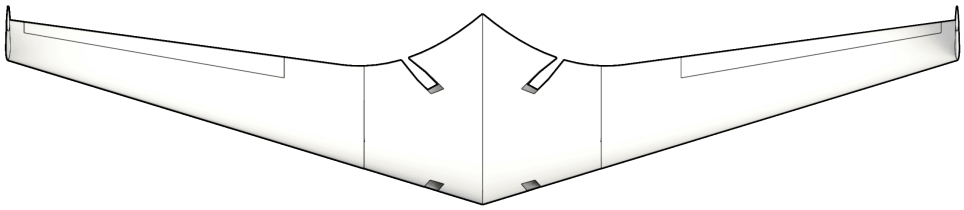

Figure 5.26: Final wing model - top view.

Upon examining the figures, it can be seen that the top and bottom caps include some openings, which are designed to ensure they can close without interfering with the frame of the UAV. The functionality of these openings can be better understood by examining figures 5.27 and 5.28, which display the wing integrated with the UAV frame.

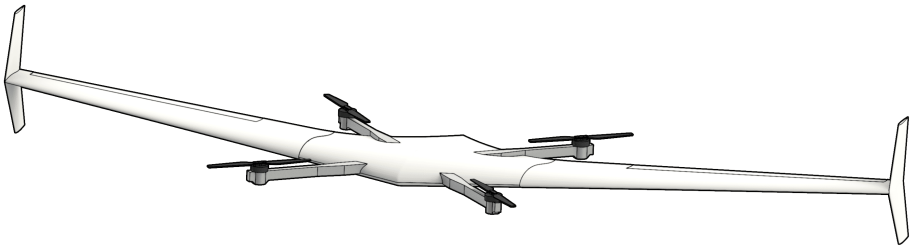

Figure 5.27: Final design - dimetric view.

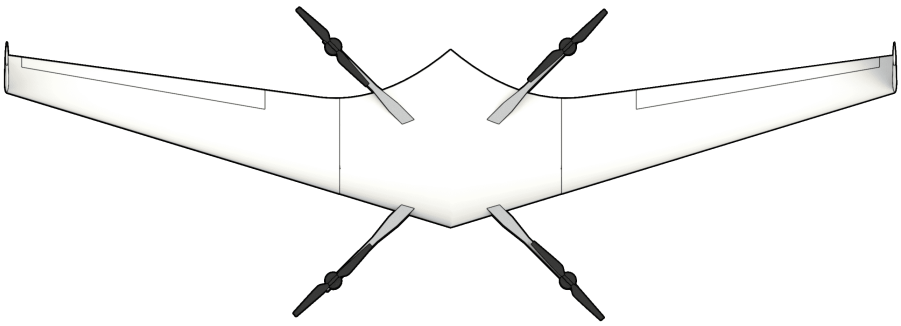

Figure 5.28: Final design - top view.

Chapter 6

Conclusions and Future Work

The primary objective of this dissertation was to design a wing for a VTOL UAV that met the requirements established by CEiiA. This chapter contains the conclusions drawn from this work, which are detailed in Section 6.1, along with some suggestions for future work presented in Section 6.2.

6.1 Main Conclusions

The research conducted in this dissertation led to the development of a flying wing. This design proved to be the most suitable option to integrate with the multirotor, given the initial requirements and the physical constraints imposed by the frame of the multirotor.

The design aimed to achieve optimal aerodynamic properties to maximize the range of the UAV, while maintaining an equilibrium between parameters such as weight, aerodynamic efficiency and footprint. The design also accounted for the disposition of the components and payload to ensure the UAV can fulfill the stability requirements in both fully loaded and empty conditions. This resulted in a wing with a 6-meter wingspan that, when integrated with the multirotor and not accounting for the drag of the exposed frame, is theoretically capable of performing 82.97 km missions over a duration of 0.92 h when fully loaded, and 105.13 km missions over a duration of 1.32 h when empty, both in their respective cruise conditions. The wing achieves this results while maintaining nearly identical flying handling qualities in both conditions and powered by a single battery with a specific energy density of 198.5 Wh/kg.

The layout of the wing structure consists of two carbon fiber spars and five foam ribs on each side, along with a foam-cored carbon fiber sandwich skin. This structure is capable of withstanding loads 6.75 times greater than the aerodynamic forces exerted on the UAV in its cruise condition and has total mass of approximately 8.5 kg.

Regarding some of the parameters and results obtained in the preliminary design, here are some observations:

- **Handling qualities:** While the stability results are satisfactory, the handling qualities were evaluated based on requirements for manned aircraft, which may not be entirely applicable. Therefore, if the UAV is intended to transport dangerous goods, it is advisable to conduct extensive flight tests to ensure its reliability under all conditions.

If necessary, the integration of a tail could be considered to improve the stability of the design.

- **Static margin and component disposition:** Although the static margin is within the acceptable range, this value is relatively small. For that reason, efforts should be made to accurately allocate the components to ensure that the weight distribution aligns as closely as possible with the distribution defined in the preliminary design.
- **Payload location:** Throughout the design process, the mass of the payload was continuously reallocated to coincide with the position of the CG of the UAV in its empty condition. This approach was adopted to prevent shifts in the location of the CG when adding or removing payload, which would impact the handling properties of the UAV. As a result, the UAV can travel to a destination fully loaded and return empty while maintaining the same flight conditions. However, placing the payload at the center of the UAV's frame means that there may not be enough space to fully utilize the UAV's 9.34 kg payload capacity, depending on the type of payload being carried, as this space is also used for the placement of system components. This means that it might be necessary to design a cargo area beneath the wing to increase the storage space and fully take advantage of the UAV's capabilities.
- **Wing mass estimate:** The initial estimated mass of the wing structure, which was used throughout the aerodynamic design, was 11 kg and was determined using a composite and sandwich mass prediction model [46]. The actual mass of the structure, calculated after the structural analyses and using Ansys to compute the masses, was approximately 8.5 kg, which corresponds to a difference of 2.5 kg. However, the mass of the structure does not include the required attachment and detachment system to connect the wing to the frame of the UAV, nor the structure needed to attach the top and bottom caps of the skin. If both these factors are accounted for, the discrepancy from the initial estimate should reduce significantly.

6.2 Future Work

The ultimate goal of this project is to develop a working model of this wing and successfully integrate it into the UAV. To achieve this, future work should involve some of the following studies:

- Development of the attachment and detachment mechanism to connect the wing to the frame of the multirotor.
- Assessment of the lift generated by the top and bottom skin caps, and development of an appropriate method for their attachment to the frame of the multirotor.
- Evaluation of the space available within the wing skin near the aircraft's center of gravity to determine if there is a need to increase the storage space to fully take advantage

of the UAV's payload capacity. This study could include designing a cargo area beneath the wing to allocate the payload.

- Development of the internal structure of the winglet and elevon, along with a method for their attachment to the wing.

Other studies that are not compulsory for the conclusion of the project but should be taken into consideration are:

- Determination of the benefits of segmenting the elevon and the optimal number of parts it should be divided into. The purpose of this study is to minimize trim drag during maneuvers that do not require the engagement of the entire elevon area.
- Computational fluid dynamics (CFD) analysis on the model of the wing with the frame of the multirotor to obtain more accurate lift and drag results. This study provides a better insight into the capabilities of the UAV, such as its the range and endurance.
- Fatigue and damage tolerance analysis on the structure to assess the degradation of the structural strength over numerous cycles, which can lead to reductions in safety margins or functional capabilities of the UAV. This analysis can also provide insights into when a component might need to be replaced.
- Assessment of the thickness and IRF of the spar caps across the semi-span of the wing and development of a spar with a variable thickness cap, which will ideally have a decreasing number of material layers as it approaches the tip. This study prevents unnecessary material usage in sections where it is not needed, which reduces the weight of the structure and results in cost savings on materials.

Bibliography

[1] S. Gudmundsson, *General aviation aircraft design: applied methods and procedures*. Elsevier, 2014. xv, xvi, 5, 6, 7, 17, 19, 26, 27, 28, 29, 30, 53, 56

[2] M. R. Birajdar and S. A. Kale, "Effect of Leading Edge Radius and Blending Distance from eading Edge on the Aerodynamic Performance of Small Wind Turbine Blade Airfoils," *International Journal of Energy and Power Engineering*, vol. 4, No. 5-1, 2015, pp. 54-58. doi: 10.11648/j.ijepe.s.2015040501.19, 2015. xv, 6

[3] S. Wang, Y. Qiao, and Z. Zhang, "Influence of camber on aerodynamic performance of airfoil based on CFD technology," *Journal of Physics: Conference Series 2276 012027*, 2022. xv, 7

[4] M. Dongli, Z. Yanping, Q. Yuhang, and L. Guanxiong, "Effects of relative thickness on aerodynamic characteristics of airfoil at a low Reynolds number," *Chinese Journal of Aeronautics*, 2015. xv, 8

[5] S. A. Brandt, R. J. Stiles, J. J. Berlin, and R. Whitford, *Introduction to Aeronautics: A Design Perspective*. AIAA, 2004. xv, 5, 7, 9, 10, 11, 13, 17, 18, 20, 22, 23

[6] I. K. Kapoulas, J. C. Statharas, A. Hatziefremidis, and A. K. Baldoukas, "Fast Airfoil Selection Methodology for Small Unmanned Aerial Vehicles," *MDPI, Applied Sciences*, 2022. xv, 9, 10, 49

[7] M. H. Sadraey, *Aircraft design: A systems engineering approach*. Wiley, 2013. xv, xix, 5, 8, 12, 14, 15, 16, 17, 21, 22, 23, 25, 27, 54, 55, 69

[8] A. Abdulhalim and T. Selim, "The effect of aspect ratio on aerodynamic performance and low separation behavior of a model wing composed from different profiles," *Journal of Energy Systems*, 2018. xv, 13

[9] T. A. Shams, S. I. A. Shah, A. Shahzad, A. Javed, and K. Mehmod, "Experimental Investigation of Propeller Induced Flow on Flying Wing Micro Aerial Vehicle for Improved 6DOF Modeling," *IEEE Access*, 2020. xv, 19, 20

[10] H. H. Hurt, *Aerodynamics For Naval Aviators*. Office of the Chief of Naval Operations, Aviation Training Division, 1959. xv, 18, 21, 22

[11] M. V. Cook, *Flight Dynamics Principles*. Elsevier, 2007. xv, xvi, 22, 23, 24, 25

[12] C. E. Dole, J. E. Lewis, J. R. Badick, and B. A. Johnson, *Flight Theory and Aerodynamics*. John Wiley & Sons, Inc, 2017. xvi, 24

[13] W. Bishop, "The Development of Tailless Aircraft and Flying Wings," *The Aeronautical Journal*, 2016. xvi, 25

[14] M. D. Maughmer, “Design of Winglets for High-Performance Sailplanes,” *AIAA*, 2016. xvi, 26

[15] T. H. G. Megson, *Aircraft Structures for engineering students*. Elsevier, 2007. xvi, 29, 30

[16] I. M. Daniel and O. lshai, *Engineering mechanics of composite materials*. Oxford University Press, Inc, 2006. xvi, 31, 33

[17] G. H. Staab, *Laminar Composites*. Butterworth-Heinemann, 2015. xvi, 32

[18] J. N. Reddy, *Mechanics of laminated composite plates and shells: theory and analysis*. CRC Press LLC, 2003. xvi, 30, 32

[19] Wingtra. (2021) Wingtra One Gen 2. [Online]. Available: https://wingtra.com/mapping-drone-wingtraone/ xvi, 36

[20] China Defense. (2021) Tilt-rotor Drone G10. [Online]. Available: https://pt.militarydrones.org.cn/tilt-rotor-drone-g10-p00103p1.html xvi, 36

[21] Dufour Aerospace. (2021) Aero2 - The Swiss Army Knife of Drones. [Online]. Available: https://www.dufour.aero/aero2 xvi, 36

[22] Boeing. (2021) X-50A Dragonfly UCAV. [Online]. Available: https://secure.boeingimages.com/archive/X-50A-CRW-UAV-Wind-Tunnel-Model-2F3XC5K152D.html xvi, 36

[23] Fly Dragon. (2021) VTOL UAV 6 hours long endurance with 1KG payload for survey and serveillance. [Online]. Available: https://www.dronefromchina.com/product/VTOL-UAV-6-hours-long-endurance-with-1KG-payload-for-survey-and-serveillance.html xvi, 36

[24] Brushless Motors Parade. (2021) T-Motor AT5220. [Online]. Available: https://brushlessmotorsparade.com/brushless-motor/t-motor-at5220-long-shaft-380kv xix, 72

[25] ANSYS inc. (2011) ANSYS Mechanical APDL Element Reference. [Online]. Available: https://www.mm.bme.hu/~gyebro/files/vem/ansys_14_element_reference.pdf xx, 84

[26] D. P. Raymer, *Aircraft Design: A Conceptual Approach*. AIAA, 2018. 5, 6, 7, 8, 10, 11, 14, 16, 18, 19, 20, 26, 28, 54, 69

[27] E. L. Houghton and P. W. Carpenter, *Aerodynamics for Engineering Students*. Elsevier, 2003. 13, 15

[28] D. J. Newman, *Interactive Aerospace Engineering and Design*. McGraw-Hill, 2002. 20, 21

[29] V. de Brederode, *Aerodinâmica Incompressível: Fundamentos*. Intituto Superior Técnico (IST Press), 2014. 27

[30] G. Ntourmas, F. Glock, F. Daoud, G. Schuhmacher, D. Chronopoulos, and E. Özcan, "Mixed Integer Linear Programming formulations of the stacking sequence and blending optimisation of composite structures," *Composite Structures*, 2016. 32

[31] A. A. Laghari, A. K. Jumani, R. A. Laghari, and H. Nawaz, "Unmanned aerial vehicles: A review," *Cognitive Robotics*, 2022. 34

[32] H. Gu, X. Lyu, Z. Li, S. Shen, and F. Zhang, "Development and experimental verification of a hybrid vertical take-off and landing (vtol) unmanned aerial vehicle (uav)," *ReseachGate*, 2017. 34

[33] Leonardo Da Vinci Inventions. (2019) Leonardo da Vinci's Aerial Screw Invention. [Online]. Available: https://www.da-vinci-inventions.com/aerial-screw 34

[34] JetPack Aviation. (2019) The History Of Personal VTOL Technology. [Online]. Available: https://jetpackaviation.com/history-of-personal-vtol-technology/ 34, 35

[35] A. Doddi, "Vertical Take-off and Landing (VTOL)," *AIAA*, 2016. 35

[36] Joby Aviation. (2023) Electric Aerial Ridesharing. [Online]. Available: https://www.jobyaviation.com/ 35

[37] EHang. (2023) EHang AAV. The Era of Urban Air Mobility is Coming. [Online]. Available: https://www.ehang.com/ehangaav/ 35

[38] A. S. Saeed, A. B. Younes, C. Cai, and G. Cai, "A survey of hybrid unmanned aerial vehicles," *Progress in Aerospace Sciences*, 2018. 35

[39] Research and Markets, "VTOL UAV: Global Strategic Business Report," *Global Industry Analysts, Inc*, 2023. 36

[40] Markets and Markets, "Fixed-wing VTOL UAV Market by Application (Military, Government & Law Enforcement, Commercial), Propulsion (Electric, Hybrid, Gasoline), Mode of operation (VLOS, EVLOS, BVLOS), Endurance, Range, MTOW and Region," *Global Forecast to 2030*, 2022. 37

[41] Regulation (EU) 2019/945. (2023) Unmanned Aerial Systems (UAS). [Online]. Available: https://www.skybrary.aero/articles/unmanned-aerial-systems-uas#The_civil_applications_of_UAS 37

[42] André. (2023) Flow5, An analysis tool for planes and sails operating at low Reynolds numbers. [Online]. Available: https://flow5.tech/ 37

[43] ——. (2023) XFLR5, an analysis tool for airfoils, wings and planes. [Online]. Available: http://www.xflr5.tech/xflr5.htm 37

[44] Mark Drela. (2013) XFOIL Subsonic Airfoil Development System. [Online]. Available: https://web.mit.edu/drela/Public/web/xfoil/ 37

[45] E. P. Lesley, "Report No. 698, Propeller tests to determine the effect of number of blades at two typical solidities," *National Advisory Committee for Aeronautics*, 1939. 38

[46] G. Garcia and P. Gamboa, "Mass prediction models for air cargo challenge aircraft," *The Aeronautical Journal*, vol. 126, pp. 249–296, 2021. 46, 90

[47] U. S. C. on Extension to the Standard Atmosphere, *U.S. Standard Atmosphere, 1976 NOAA - SIT 76-1562*. National Oceanic and Atmospheric Administration, 1976. 49, 62

[48] T. A. Shams, S. I. A. Shah, A. Javed, and S. H. R. Hamdani, "Airfoil Selection Procedure, Wind Tunnel Experimentation and Implementation of 6DOF Modeling on a Flying Wing Micro Aerial Vehicle," *MDPI, Micromachines*, 2020. 49

[49] J. D. Anderson, "Aircraft Performance and Design," *Tata McGraw-Hill*, 2012. 50

[50] André. (2019) Triangle-based Galerkin panel methods. [Online]. Available: https://flow5.tech/wp-content/uploads/2019/11/Galerkin.pdf 51

[51] J.M.T. Horwitz. (2021) Parametric design of the Flying-V Winglets for Improved Lateral-Directional Stability and Control. MSc Thesis, Delft Technical University. [Online]. Available: http://resolver.tudelft.nl/uuid:d7513b36-b9fd-4f8a-8726-f5c7ee7f3a6b 53

[52] B. Etkin and L. D. Reid, *Dynamics of Flight: Stability and Control*. Wiley, 1996. 55

[53] Tyler M. Foster. (2005) Dynamic Stability and Handling Qualities of Small Unmanned-Aerial-Vehicles. MSc Thesis, Brigham Young University. [Online]. Available: https://scholarsarchive.byu.edu/cgi/viewcontent.cgi?article=1218&context=etd 55, 70

[54] P. F. G. L. F. de Albuquerque, *Mission-Based Multidisciplinary Design Optimization Methodologies for Unmanned Aerial Vehicles with Morphing Technologies, Doutoramento em Engenharia Aeronáutica*. UBI, 2017. 56

[55] ANSYS inc. (2017) ANSYS Composite PrepPost User's Guide. [Online]. Available: https://www.ansys.com 59

[56] FEA Tips. (2023) ANSYS Solver Control Settings Explained. [Online]. Available: https://featips.com/2023/05/15/ansys-solver-control-settings-explained/ 59

[57] I. H. Abbott, A. E. V. Doenhoff, and J. Louis S. Stivers, "Report No. 824, Summary of airfoil data," *National Advisory Committee for Aeronautics*, 1945. 63

[58] Aerial Drone Photography and Video Services. (2021) Tattu 22000mAh 22.2V 30C 6S Lipo Battery with XT90-S Plug for UAV Drone. [Online]. Available: https://1updrones.com/product/tattu-22000mah-22-2v-30c-6s-lipo-battery-with-xt90-s-plug-for-uav-drone/ 70

[59] EASA eRules. (2018) Easy Access Rules for Very Light Aeroplanes (CS-VLA) (Amendment 1). [Online]. Available: https://www.easa.europa.eu/en/document-library/easy-access-rules/easy-access-rules-very-light-aeroplanes-cs-vla 73

[60] Skywell. (2020) Unidirectional Carbon Fiber Prepreg 395 GPA 0.142mm Thickness. [Online]. Available: https://www.carbonfiberrawmaterial.com/china-unidirectional_carbon_fiber_prepreg_heat_resistance_395_gpa_0_142mm_thickness-12525884.html 78

[61] HEXCEL. (2013) Prepreg Properties - HexPly® 8552 Woven Carbon Prepregs (AS4 Fibre). [Online]. Available: https://energy.ornl.gov/CFCrush/materials/uou/8552_eu.pdf 78

[62] K. Suresh and S. P. Regalla, "Effect of mesh parameters in finite element simulation of single point incremental sheet forming process," *Procedia Materials Science*, 2014. 82

Appendix A

Airfoil Selection

This appendix showcases the graphical representation of the aerodynamic coefficients obtained from the airfoil analysis, for the two considered trip locations and the three specified Reynolds numbers.

A.1 Airfoil Measurements - Trip Location set to 1

Figures A.1 through A.3 display the data of the selected parameters of interest for each airfoil, which are outlined in Section 4.3.3, at three different Reynolds numbers, defined in Section 5.2.1, with a trip location set to 1.

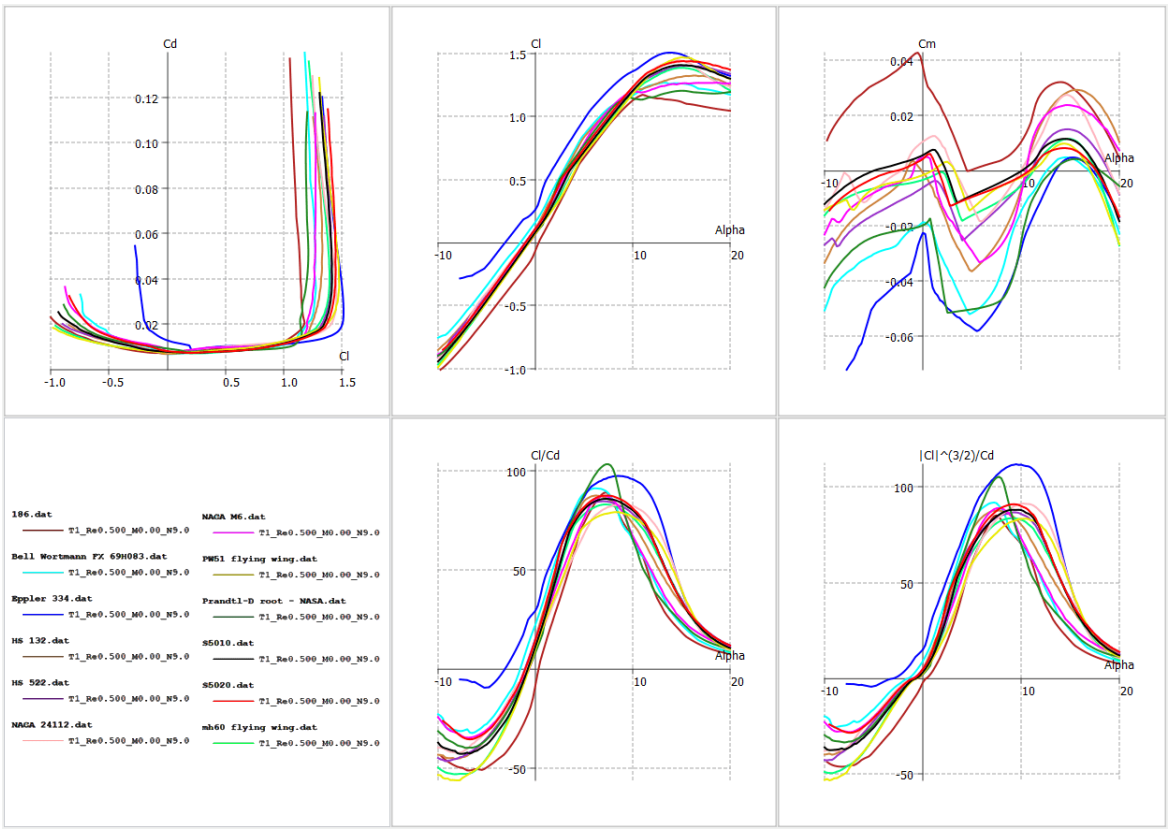

Figure A.1: Airfoil characteristics at 500,000 Re and with trip location set to 1.

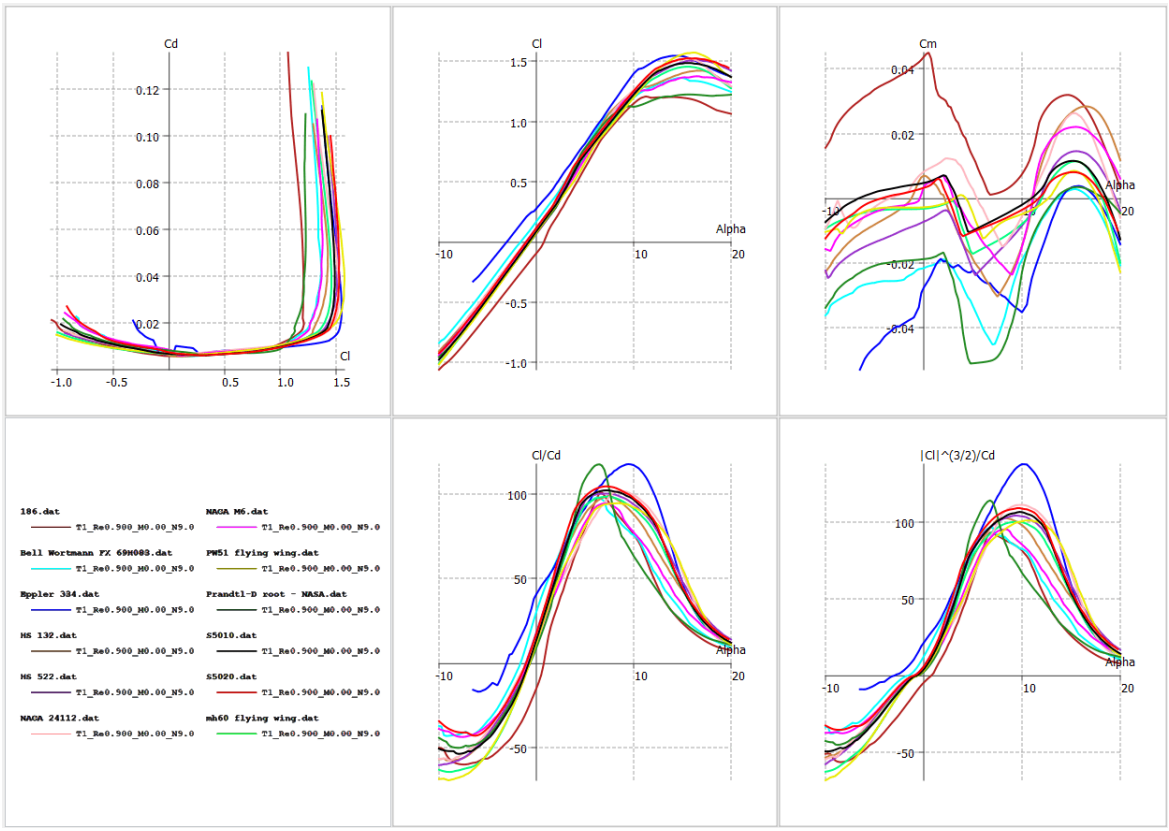

Figure A.2: Airfoil characteristics at 900,000 Re and with trip location set to 1.

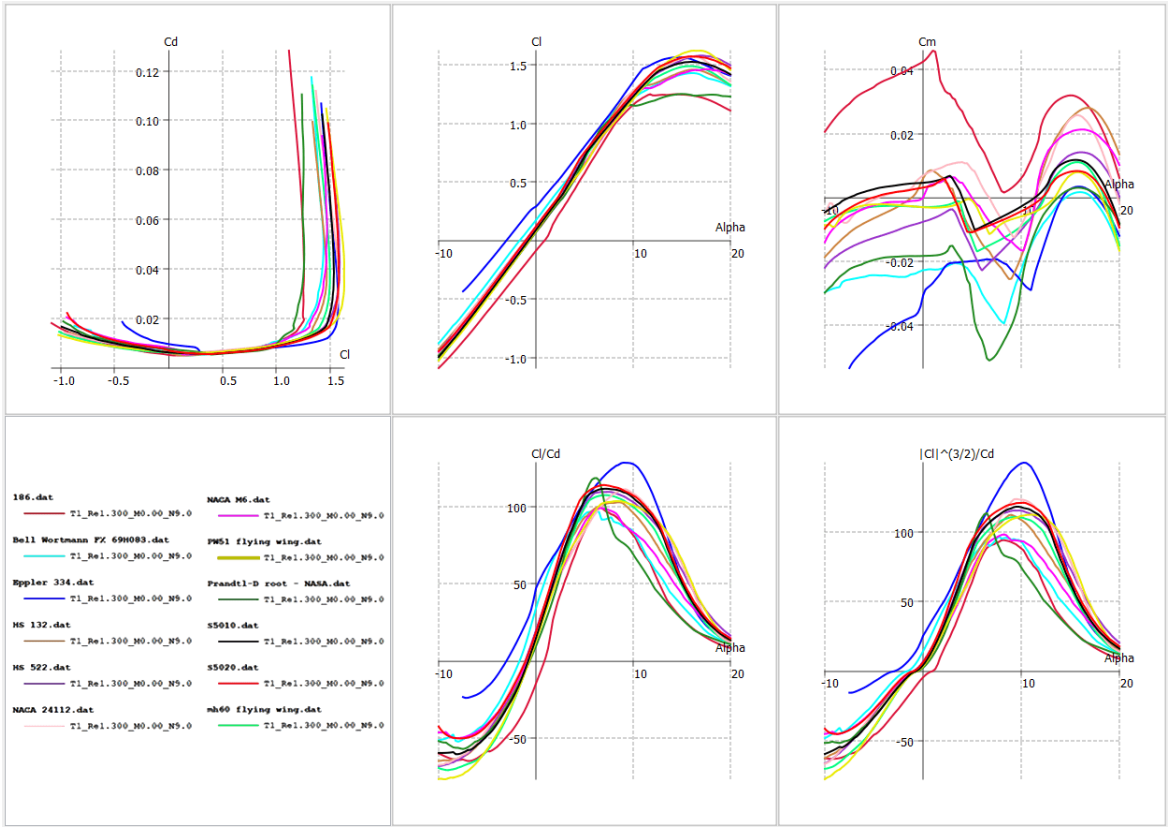

Figure A.3: Airfoil characteristics at 1,300,000 Re and with trip location set to 1.

A.2 Airfoil Measurements - Trip Location set to 0.3

Figures A.4 through A.6 display the data of the selected parameters of interest for each airfoil, which are outlined in Section 4.3.3, at three different Reynolds numbers, defined in Section 5.2.1, with a trip location set to 0.3.

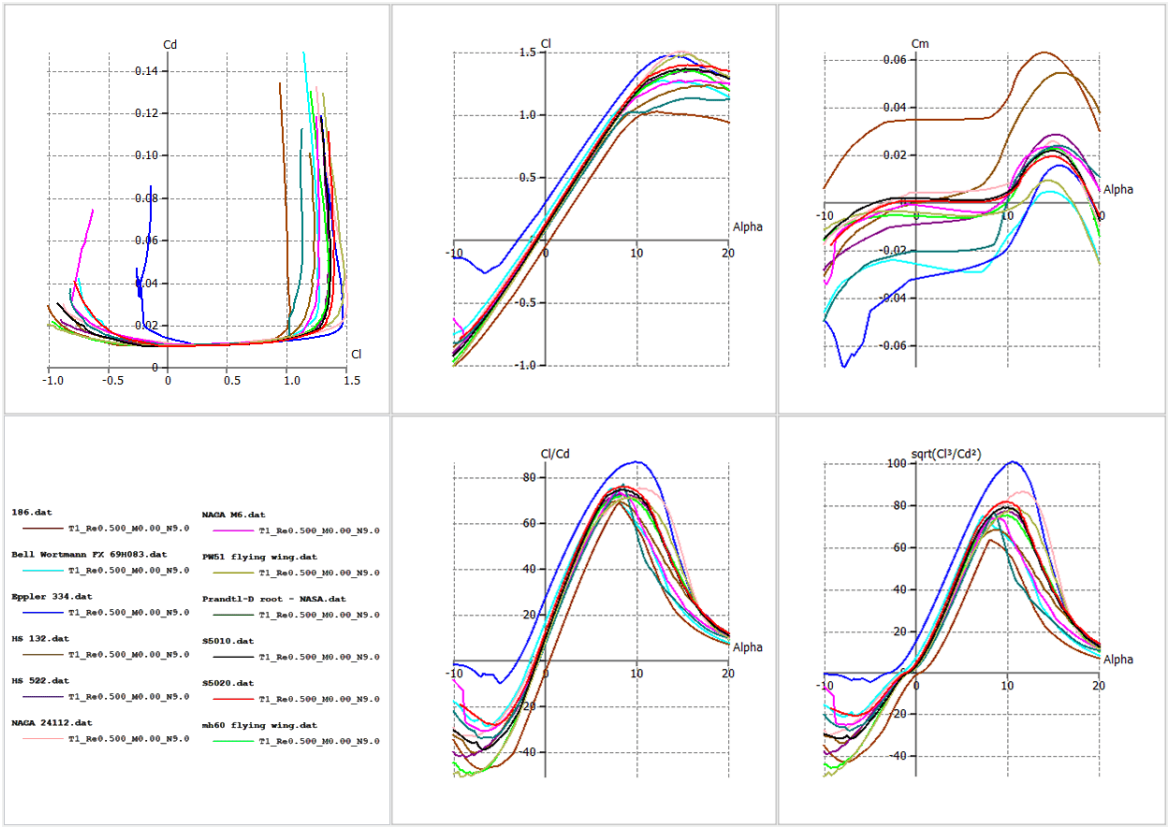

Figure A.4: Airfoil characteristics at 500,000 Re and with trip location set to 0.3.

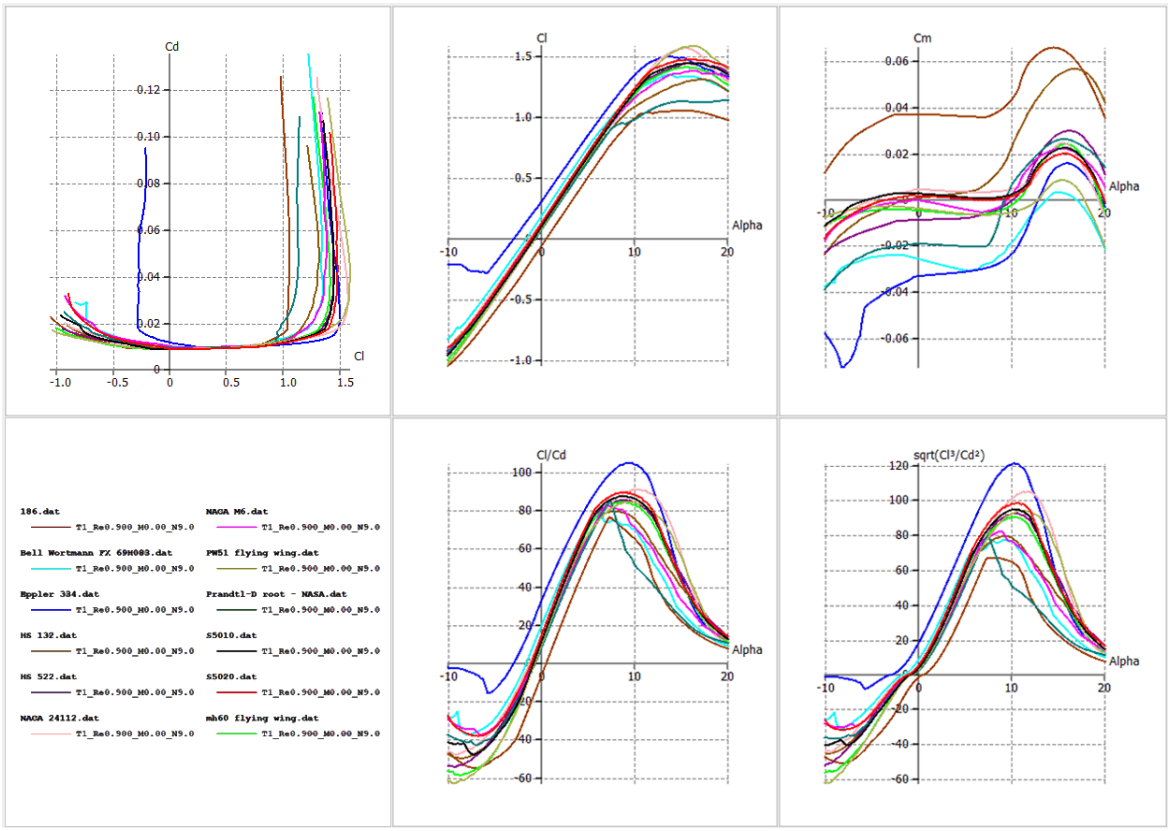

Figure A.5: Airfoil characteristics at 900,000 Re and with trip location set to 0.3.

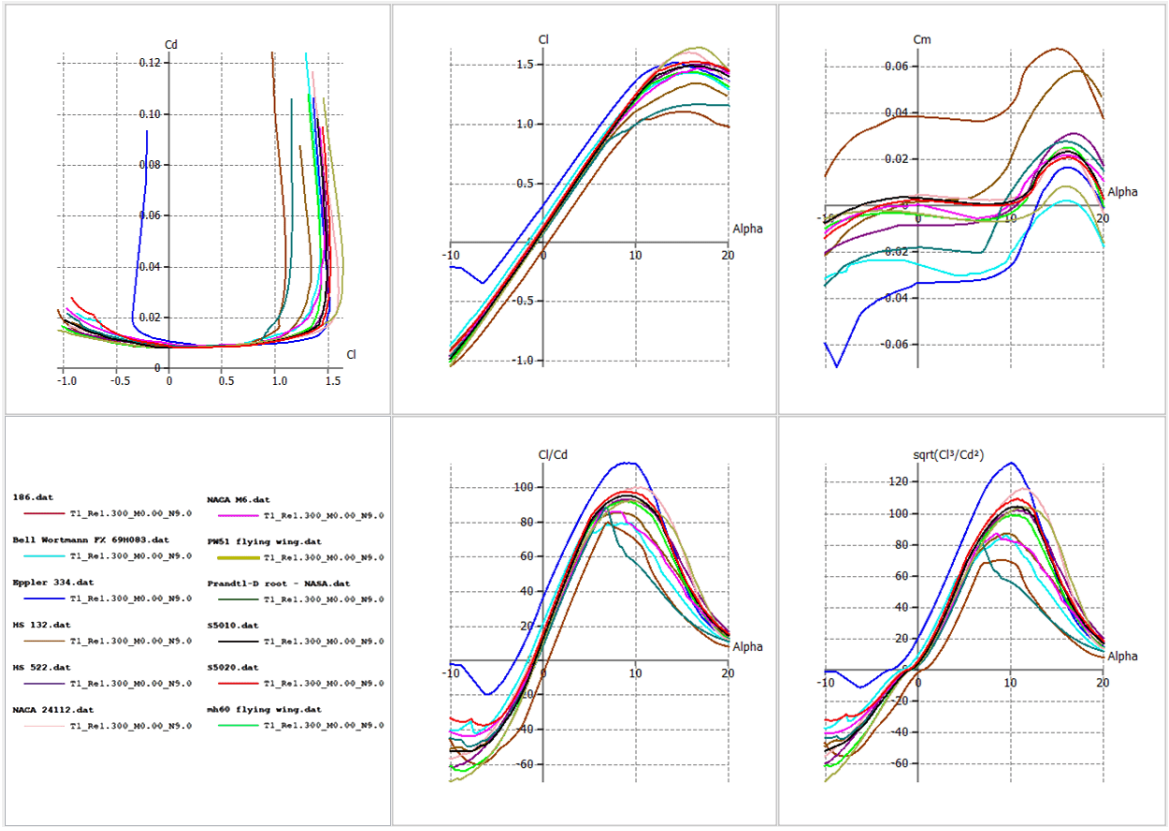

Figure A.6: Airfoil characteristics at 1,300,000 Re and with trip location set to 0.3.

Appendix B

Aerodynamic Model

This appendix displays the final model utilized to perform the aerodynamic analyses, along with its integration with the frame of the multirotor. Both of these processes were achieved using Flow5 software.

B.1 Analysis Model

Figures B.1 through B.3 showcase the wing analysis model and the defined mesh quality from three different perspectives.

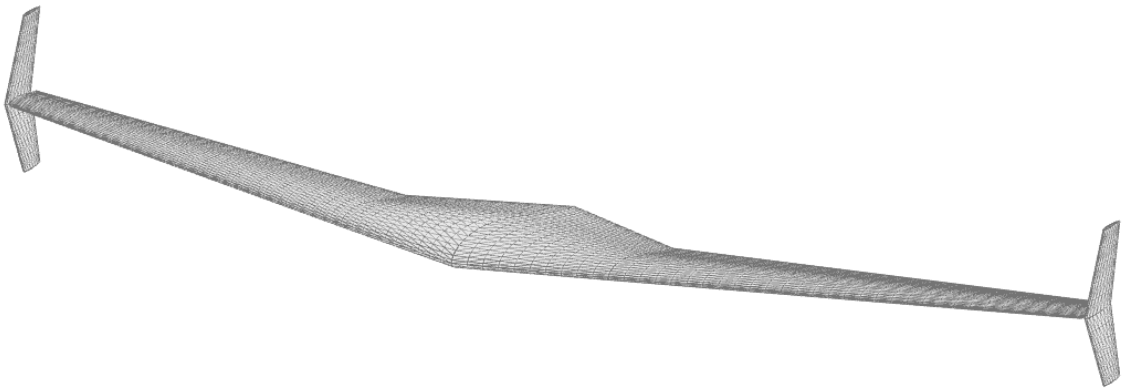

Figure B.1: Wing analysis model - dimetric view.

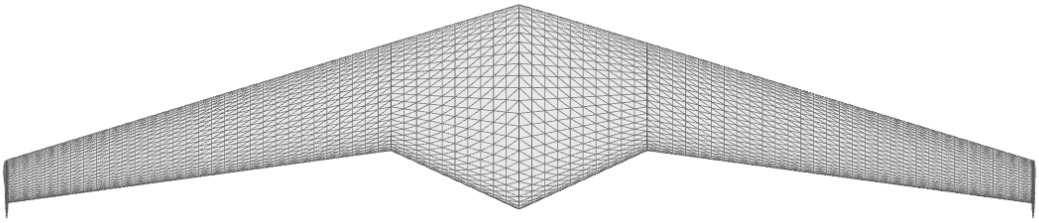

Figure B.2: Wing analysis model - top view.

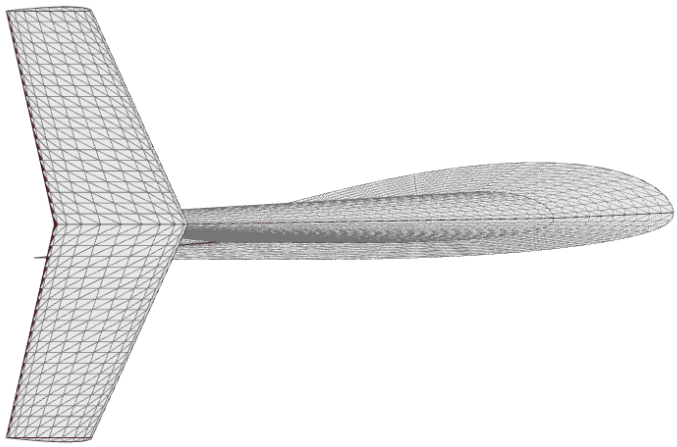

Figure B.3: Wing analysis model - side view.

B.2 Model Integration

Figures B.4 and B.5 illustrate the integration of the wing model with the model of the multirotor's frame. The process of combining these two models aided in determining whether there was sufficient space within the wing to accommodate the central part of the frame and whether the dimensions of the wing were correctly sized.

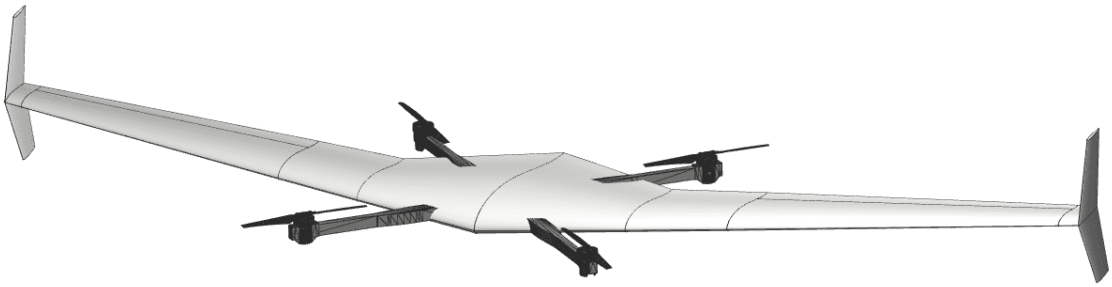

Figure B.4: Aerodynamic wing model integrated with the multirotor's frame - dimetric view.

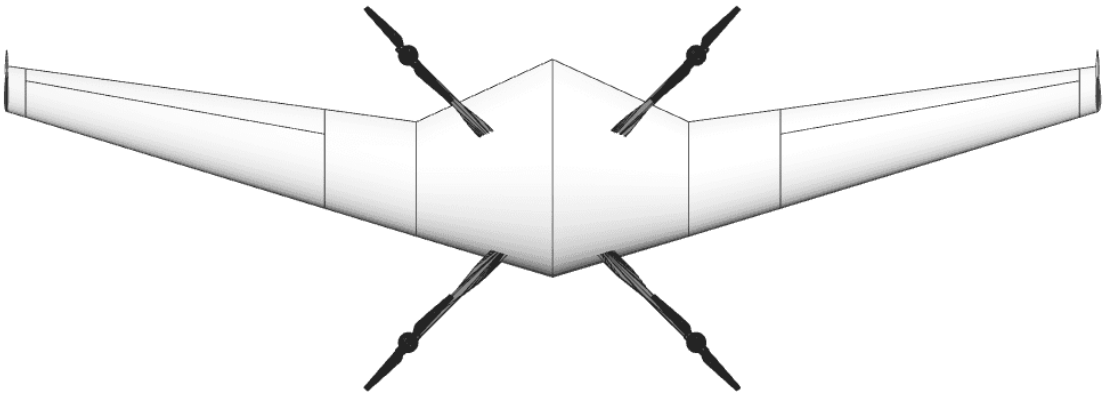

Figure B.5: Aerodynamic wing model integrated with the multirotor's frame - top view.